Fabrication and evaluation of deep surface grating DFB stripe lasers using quantum well material

by

Hiroaki Abe

April 1994

A thesis submitted to the Faculty of Engineering of the University of Glasgow
for the degree of Master of Science

© Hiroaki Abe, 1994

ProQuest Number: 13832112

All rights reserved

INFORMATION TO ALL USERS
The quality of this reproduction is dependent upon the quality of the copy submitted.

In the unlikely event that the author did not send a complete manuscript
and there are missing pages, these will be noted. Also, if material had to be removed,
a note will indicate the deletion.

ProQuest 13832112

Published by ProQuest LLC (2019). Copyright of the Dissertation is held by the Author.

All rights reserved.
This work is protected against unauthorized copying under Title 17, United States Code
Microform Edition © ProQuest LLC.

ProQuest LLC.
789 East Eisenhower Parkway
P.O. Box 1346
Ann Arbor, MI 48106 – 1346

Thesis
10302
Copy 1

Acknowledgements

I would like to express my thanks to my supervisor Professor Richard De La Rue for accepting me as a research student, for his extremely valuable help, encouragement and many useful discussions.

I would also like to express my thanks to my second supervisor Dr. Stephen Ayling for his supervision on all aspects of the experimental and theoretical work and his very helpful comments.

I would like to thank Mr. Masataka Kataoka, President of ALPS Electric Co., Ltd., for the decision to allow me to study abroad.

I would also like to thank Dr. Tsutomu Nakamura, Managing director of ALPS Electric Co., Ltd., for his academic advice and encouragement.

I would also like to thank Mr. Ichiro Morishita, Chief of the OE group of ALPS Electric Co., Ltd., for his kind support.

The help and assistance of members of the Mechanical and Electronic Workshops of Glasgow University is gratefully appreciated. Special thanks also go to Mr. Robert Harkins, Mrs. Lois Hobbs, Mr. Tommy Cairns, Mr Jimmy Young and Mr. Dave Clifton.

I would further like to extend my gratitude to all my colleagues who made my stay at Glasgow University enjoyable.

ALPS Electric Co., Ltd. are to be thanked for their financial support over the two years of my work at Glasgow.

Table of contents

Abstract

Content of the thesis

Chapter 1 : Introduction

1.1 DFB lasers 1
1.2 A brief history of research into DFB lasers 2
1.2.1 DFB laser with a step-like non-uniform stripe width structure 2
1.2.2 DFB laser with a gradual phase shift region 3
1.2.3 DFB air-grating stripe lasers 3
1.3 Aims of this work 4
References 5

Chapter 2 : Theory of DFB lasers

2.1 Wavelength dependence of Bragg reflections 7
2.2 The coupled-mode solutions 8
2.3 Lasing with distributed feedback 10
2.4 Coupling coefficient κ 12
2.5 Non-uniform stripe DFB lasers 14
References 15

Chapter 3 : Epitaxial wafer structure and analysis

3.1 Epitaxial wafer structure 16
3.2 Epitaxial wafer analysis using broad area oxide stripe lasers 16
3.2.1 Theory of epitaxial wafer analysis 17
3.2.2 Experimental results 19
References 25

Chapter 4 : Device structure and fabrication

4.1 Device structure 26
4.2 Fabrication 26
4.2.1 Sample preparation 27
4.2.2 Etching of GaAs contact layer in the grating regions 27
4.2.3 Manufacture of gratings alongside the ridge 28
(1) The two beam interference method 28
(2) NiCr shadowed evaporation 31
(3) Dry-etching resist, ARC, SiO_2 and GaAs layers 32
4.2.4 Making contacts 36
4.2.5 Deposition of anti-reflection (AR) coatings 37
4.2.6 Mounting and wire-bonding 37
References 38

Chapter 5 : Measurements

5.1 measurement method 39
(1) Injection current - Voltage characteristic (I-V curves) and Light output power - Injection current characteristics (L-I curves) 39
(2) Far field pattern 40
(3) Laser spectra 40
5.2 Experimental results and interpretation 43
5.2.1 Results for lasers in pulsed operation 43
(1) Narrow area oxide stripe lasers without AR coatings 43
(2) Narrow area oxide stripe lasers with AR coatings 47
(3) Surface grating DFB uniform stripe lasers without AR coatings 49
(4) Surface grating DFB uniform stripe lasers with AR coatings 53
(5) Surface grating DFB non-uniform stripe lasers without AR coatings 63
(6) Surface grating DFB non-uniform stripe lasers with AR coatings 66
5.2.2 Results for lasers in CW operation 70
(1) Surface grating DFB uniform stripe lasers with AR coatings 70
(2) Surface grating DFB non-uniform stripe lasers with AR coatings 80
References 84

Chapter 6 : Conclusions and future work

6.1 Conclusions 86
6.2 Future work 87
References 88

Abstract

This thesis describes experiments performed to fabricate and evaluate deep surface grating distributed feedback (DFB) lasers using double quantum well material. The distributed feedback structure was created by deep, dry etched, gratings alongside the ridge in the top confining layer of the laser. The material system used consisted of two 0.01 μm GaAs quantum wells and 0.01 μm $Al_{0.2}Ga_{0.8}As$ barriers. The typical emission wavelength of the lasers was about 860 nm.
Conditions were optimised to produce a third order 1:1 mark-space ratio grating using holographic exposure, shadow evaporation and reactive ion etching.
The typical threshold current of the 2.5 μm stripe DFB lasers was 20 % lower compared with the laser fabricated without etching of the GaAs contact layer in pulsed operation and was 37 mA in CW operation. The typical external differential quantum efficiency per facet was 15 % in CW operation. The temperature range for single transvere DFB mode operation was found to be from 10 to 75 °C .
Stopband widths were estimated using the scanning Fabry-Perot interferometer. From the stopband width, the coupling coefficient of 2.5 μm width stripe DFB lasers was estimated to be 14 ± 2.2 cm^{-1}, in agreement with the value calculated using the effective index method.
Variable stripe width DFB lasers, equivalent to corrugation pitch modulated (CPM) structures were also fabricated. Such lasers were effective in achieving single longitudinal mode operation.

Contents of the thesis

Chapter One is an introduction to the thesis topic. It outlines the advantages of DFB lasers and deep surface grating DFB stripe lasers. A brief history of research into DFB lasers is also given.

Chapter Two provides the theoretical background to the work. The coupled mode solutions, calculation of coupling coefficient are described and method of calculation for DFB non-uniform stripe lasers is also introduced briefly.

Chapter Three describes the epitaxial wafer structure and its device characterisation using broad area oxide stripe lasers.

Chapter Four describes the fabrication process for deep surface grating DFB stripe lasers using holographic exposure, shadow evaporation and reactive ion etching.

Chapter Five describes the measurement method and the measured results for surface grating DFB uniform stripe lasers and surface grating DFB non-uniform stripe lasers in pulsed and CW operation. Interpretation of the measured results is also described.

Chapter Six summarises the contents and results from this thesis, giving conclusions on the practical application of surface grating DFB stripe lasers and suggests directions for future work.

Chapter 1 : Introduction

1.1. DFB lasers

Distributed feedback (DFB) lasers have useful characteristics, such as smaller emission linewidth and stable dynamic single-mode operation, in comparison to Fabry-Perot lasers. For instance, in long-cavity AlGaAs/GaAs multi-quantum well DFB lasers emitting at 0.86 μm, a minimum linewidth of 1.5 MHz has been reported.[1-1] In three-section corrugation-pitch-modulated multi-quantum well DFB (CPM-MQW-DFB) lasers emitting at 1.55 μm a spectral linewidth of less than 98 kHz has been achieved.[1-2] As regards stable dynamic single-mode operation characteristics, side-mode suppression ratios of more than 30 dB have been achieved under 2Gbps NRZ (non-return-to-zero) modulation. Because of these characteristics, InGaAs/InP DFB lasers have been extensively developed and applied for long haul high-bit-rate optical fibre transmission systems. The modulation bandwidth is ultimately limited by the linewidth of the laser source, AlGaAs/GaAs DFB lasers have been researched as the optical source for holographic laser devices, especially in consumer electronics, such as holographic laser beam printers.[1-3]
DFB lasers are also useful as optical sources in integrated optics based on miniature optical waveguide components, such as optical amplifiers, modulators and passive waveguides using disordering[1-4, 1-5] of quantum well structures. This is because they do not need cleaved facets, since the feedback is generated by the grating structure.
Most DFB lasers have been fabricated by forming a feedback grating parallel to the growth plane, either below or above the active region, during a growth interruption. But this approach is complicated by the need for epitaxial regrowth. On the other hand, methods for incorporating distributed feedback in a ridge waveguide laser by means of lateral gratings and a single growth step have been demonstrated by Miller et al.[1-6,1-7] The necessary Bragg condition for distributed feedback was satisfied by etching gratings alongside the ridge in the top confining layer of the laser, on either side of the contact stripe. The advantages of this approach are simple fabrication and the possibility of full characterisation of the wafer before processing into DFB lasers.

In the optoelectronics research group at Glasgow University, surface grating DFB stripe lasers using quantum well material have been researched with a view to improving longitudinal mode stability.

1.2. A brief history of research into DFB lasers

In this section a brief history of research into DFB lasers by others is presented.
The first description of DFB laser research was given by Nakamura et al, 1973.[1-8] The lasers were operated by optical pumping. The quarter-wavelength shifted DFB laser was later proposed, in order to overcome the multi-longitudinal mode operation, by Haus et al, 1976.[1-9] The important feature of the quarter-wavelength shifted DFB laser was its single longitudinal mode operation with the lowest threshold gain.
Many types of DFB laser have been researched in order to attain stability of the longitudinal mode and other improvements in performance. Among them, structures considered to be closely related to this work are as follows:

(1) DFB lasers with a step-like non-uniform stripe width structure,[1-10, 1-11]

(2) DFB lasers with a gradual phase shift region, [1-12, 1-13, 1-14]

(3) DFB ridge-waveguide lasers.[1-6,1-7]

1.2.1. DFB laser with a step-like non-uniform stripe width structure[1-10, 1-11]

DFB lasers with a step-like non-uniform stripe width structure were proposed by H.Soda et al, 1984[1-10] and K.Tada et al, 1984[1-11] in order to stabilise single longitudinal mode oscillation. The laser had a phase adjustment region which was located at the centre of the laser. The phase adjustment region consisted of a wider stripe the width of which was 3 μm. The length of the phase adjustment region was 60 μm and the length of the laser chip was 400 μm. The narrower stripe width was 2 μm. Current was injected into the whole length. The difference in propagation constant $\Delta\beta$ was calculated as 250 cm^{-1} by using the effective index approximation. With the length of the phase adjustment region chosen to be L=60 μm, the amount of the phase shift $\Delta\beta L$ was calculated to be $0.48\,\pi$.
The phase adjusted DFB laser lased near the Bragg wavelength with a threshold current of 28 mA and stable single longitudinal mode oscillation was achieved up to a light output of 10 mW at room temperature.

1.2.2. DFB laser with a gradual phase shift region[1-12, 1-13, 1-14]

The DFB laser with a gradual phase shift region was proposed by M.Okai, 1989 in order to reduce the spatial hole burning effect. A CPM (Corrugation-pitch modulated) structure was introduced into 1200 μm long MQW-DFB lasers, in order to obtain narrow spectral linewidth. The CPM structure had a phase-arranging region around the centre of the laser cavity to attain an effective $\lambda/4$-shift. In the 360 μm long phase arranging region, the corrugation pitch was 0.8 nm longer than that of other regions. The CPM grating was fabricated by the photomask self-interference method. The CPM structure was effective in suppressing spatial hole burning effects since the light intensity profile along the CPM-DFB laser was much flatter than that along a conventional $\lambda/4$-shifted DFB laser. The threshold current of the 1200 μm long CPM-MQW-DFB laser was 20 mA and the slope efficiency was 0.2 W/A per facet. The minimum spectral linewidth achieved was 170 kHz at 25 mW output power.

1.2.3. DFB air-grating stripe lasers[1-6, 1-7]

The DFB air-grating stripe laser was proposed by L.M.Miller et al,[1-6]1991. The operation of this DFB air-grating stripe laser combined the lateral optical confinement of the ridge waveguide with DFB gratings etched along the side of the laser stripe. The gratings extended to the laser facets on either side of the laser stripe width. The gratings were etched through the AlGaAs top confining layer and close to the strained layer of the active region. In this way, the gratings formed a lateral effective index step which assisted in lateral optical confinement, as in a conventional ridge laser structure. The gratings also provided optical feedback when the period of the grating satisfied the Bragg condition within the gain spectrum. The third order gratings were formed along the ridge by direct electron beam writing and reactive ion etching in a single post-growth processing step.
An InGaAs/GaAs/AlGaAs strained-layer DFB air-grating stripe QW heterostructure laser with third-order gratings which operated at room temperature under pulsed conditions was demonstrated. The threshold current was I_{th}=85 mA and single longitudinal emission at λ=1.0324 μm was presented up to $2.2\times I_{th}$, where other DFB modes reached threshold. Results for CW operation were not reported.

1.3. Aims of this work

Deep surface grating DFB stripe lasers have several advantages , as discussed in the previous section. But this type of laser has not been fully characterised, especially in CW operation.

The purpose of the experimental work described in this thesis is as follows:

(1) characterisation of surface grating DFB stripe lasers with conventional gratings, such as output power - drive current characteristics, temperature dependence of the spectrum and emission field patterns, including CW operation,

(2) estimates of the stopband and coupling coefficient values,

(3) characterisation of surface grating DFB non-uniform stripe lasers and experimental confirmation of the effectiveness of the non-uniform structure in achieving single longitudinal mode operation.

References

1-1. K.Kojima, K.Hara, K.Kameya and K.Kyuma, "Narrow-linewidth AlGaAs/GaAlAs multiple quantum well distributed feedback lasers", Electronics Letters, Vol. 25, p. 240-241, 1989.

1-2. M.Okai and T.Tsuchiya, "Tuneable DFB lasers with ultra-narrow spectral linewidth", Electronics Letters, Vol. 29, p. 349-351, 1993.

1-3. Sharp co., ltd., Optical Semiconductor Device catalogue, 1992.

1-4. J.H.Marsh, S.I.Hansen, A.C.Bryce and R.M.De La Rue, "Applications of neutral impurity disordering in fabricating low-loss optical waveguides and integrated waveguide devices", Optical and Quantum Electronics, Vol. 23, p. s941-s957, 1991.

1-5. I.Gontijo, T.Krauss, R.M.De La Rue, J.S.Roberts and J.H.Marsh, "Very low loss extended cavity GaAs/AlGaAs lasers made by impurity-free vacancy diffusion", Electronics Letters, Vol. 30, p. 145-146, 1994.

1-6. L.M.Miller, J.T.Verdeyen, J.J.Coleman, R.P.Bryan, J.J.Alwan, K.J.Beernink, J.S.Hughes, and T.M.Cockerill, "A distributed feedback ridge waveguide quantum well heterostructure laser", IEEE Photonics Technology Letters, Vol. 3, p. 6-8, 1991.

1-7. L.M.Miller, K.J.Beernink, J.T.Verdeyen, J.J.Coleman, J.S.Hughes, G.M.Smith, J.Honing and T.M.Cockerill, "Characterization of an InGaAs-GaAs-AlGaAs strained-layer distributed-feedback ridge-waveguide quantum-well heterostructure laser", IEEE Photonics Technology Letters, Vol. 4, p. 296-299, 1992.

1-8. M.Nakamura, A.Yariv, H.W.Yen, S.Somekh and H.L.Garvin, "Optically pumped GaAs surface laser with corrugation feedback", Applied Physics Letters, Vol. 22, p. 515, 1973.

1-9. H.A.Haus, "Antisymmetric taper of distributed feedback lasers", IEEE Journal of Quantum Electronics, Vol. QE-12, p. 532, 1976.

1-10. H.Soda, K.Wakao, H.Sudo, T.Tanahashi and H.Imai, "GaInAsP/InP phase-adjusted distributed feedback lasers with a step-like nonuniform stripe width structure.", Electronics Letters, Vol. 20, p. 1016-1018, 1984.

1-11. K.Tada, Y.Nakane and A.Ushirokawa, "Proposal of a distributed feedback laser with nonuniform stripe width for complete single-mode oscillation.", Electronics Letters, Vol. 20, p. 82-84, 1984.

1-12. M.Okai, S.Tsuji, and N.Chinone, "Stability of the longitudinal mode in $\lambda/4$-shifted InGaAsP/InP DFB lasers", IEEE Journal of Quantum Electronics, Vol. QE-25, p. 1314-1319, 1989.

1-13. M.Okai, S.Tsuji, N.Chinome and T.Harada, "Novel method to fabricate corrugation for $\lambda/4$-shifted distributed feedback laser using a grating photomask", Applied Physics Letters, Vol. 55, p. 415-417, 1989.

1-14. M.Okai, T.Tsuchiya, K.Uomi, N.Chinone and T.Harada, "Corrugation-pitch modulated MQW-DFB lasers with narrow spectral linewidth", IEEE Journal of Quantum Electronics, Vol. 27, p. 1767-1772, 1991.

Chapter 2 : Theory of DFB lasers

In this chapter, the theory of DFB lasers and DFB non-uniform stripe lasers is described.

An analysis of laser action in a periodic structure was presented first by Kogelnik and Shank in 1972.[2-1] The basic concept had been used in analysing Bragg diffraction of X-rays and light diffraction by acoustics. After the analysis, Wang[2-2] and Streifer et al.[2-3] presented a more generalised theory for semiconductor lasers with built-in gratings, that is, DFB lasers and DBR lasers.

2.1. Wavelength dependence of Bragg reflections

The principle of DFB lasers is based on Bragg's law, which states that the electromagnetic waves reflected from different planes in a crystal will be in phase if the following condition is satisfied

$$2d\sin\theta = m\lambda \qquad [2.1]$$

where θ is glancing angle, d is the separation between successive planes, λ is the wavelength of radiation and m is an integer. To adapt Eqn. [2.1] to the case of 180° reflection of light by a grating in a DFB laser, it is only necessary to let d equal the grating period Λ, let λ equal λ_0 / n_{eff}, where n_{eff} is the effective index in the waveguide for the mode under consideration, and let θ equal 90°. Under these assumptions Eqn. [2.1] becomes

$$2\Lambda = m\frac{\lambda_0}{n_{eff}} \qquad [2.2]$$

The vacuum wavelength of light that will be reflected through 180° by such a grating is therefore

$$\lambda_0 = \frac{2\Lambda n_{eff}}{m} \qquad [2.3]$$

Although the grating is capable of reflecting many different longitudinal modes, corresponding to the various values of m, usually only one mode will lie within the gain bandwidth of the laser.

2.2. The coupled-mode solutions

The fraction of the optical power that is reflected by a grating such as that shown in Fig.2.1 depends on many factors, including the thickness of the waveguiding layer, the depth of the grating teeth and the length of the grating region. The determination of the fraction of reflected optical power is mathematically quite complex. It is possibly the best approach is to use coupled-mode theory, as was done by Kogelnik and Shank[2-1] and by Yariv.[2-4] In coupled-mode analysis, it is assumed that the grating is only weakly coupled to the optical mode. Using this approach, Yariv has shown that the coupling can be characterised by a coupling coefficient κ.

In Fig.2.1, for the first order gratings, the reflection is essentially limited to coupling between only the forward and backward waves travelling in the $\pm$z direction. Then the incident field $B(z)e^{i\beta z}$ and the reflected field $A(z)e^{i\beta z}$ are functions of the distance z, given by the expressions[2-4]

$$A(z)e^{i\beta z} = B(0)\frac{i\kappa e^{i\beta_0 z}}{-\Delta\beta\sinh(SL)+iS\cosh(SL)}\sinh[S(z-L)] \quad [2.4]$$

and

$$B(z)e^{i\beta z} = B(0)\frac{e^{-i\beta_0 z}}{-\Delta\beta\sinh(SL)+iS\cosh(SL)}\cdot \{\Delta\beta\sinh[S(z-L)]+iS\cosh[S(z-L)]\} \quad [2.5]$$

where

$$S=\sqrt{\kappa^2-(\Delta\beta)^2} \quad [2.6],$$

$$\Delta\beta=\beta-\beta_0 \quad [2.7],$$

$$\beta_0=\frac{m\pi}{\Lambda} \quad [2.8],$$

κ is the coupling coefficient, β is the propagation constant, Λ is the grating period, L is the length of the grating and m is an integer. For sufficiently large arguments of the hyperbolic functions in Eqns. [2.4] and [2.5], the incident optical power decreases exponentially with z, as power is reflected into the backward travelling wave. The effective reflection coefficient R_{eff} and corresponding transmissions T_{eff} near the Bragg wavelength are given by

$$R_{eff}=\left|\frac{A(0)}{B(0)}\right|^2 \quad [2.9],$$

and

$$T_{eff}=\left|\frac{B(L)}{B(0)}\right|^2 \quad [2.10]$$

The calculated reflection characteristics of a grating length L as a function of the detuning $\Delta\beta L=[(\omega-\omega_0)L/c]n_{eff}$ are shown in Fig.2.2. From the characteristics, the reflectivity becomes a maximum at the Bragg frequency, $\omega=\omega_0$.

In these index-coupling grating waveguides, there exists a stopband[2-4] $(\Delta\omega)_{gap}$ given by

$$(\Delta\omega)_{gap} = \frac{2\kappa c}{n_{eff}} \tag{2.11}$$

where c is the vacuum velocity of light.

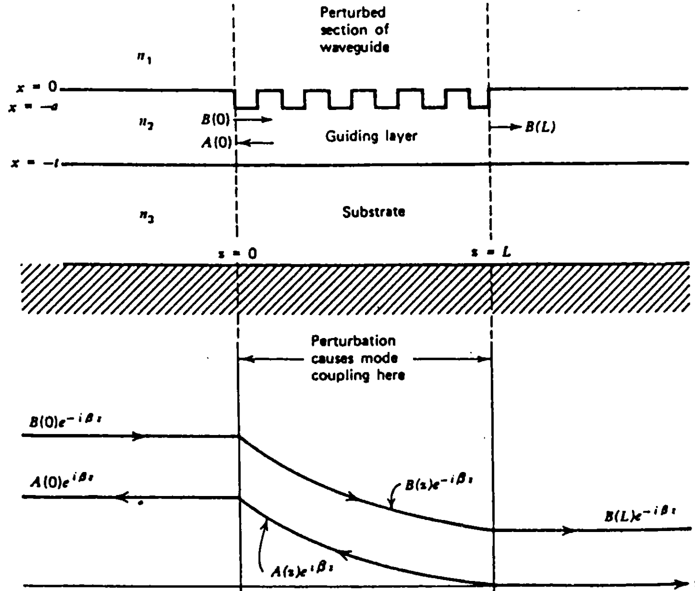

Fig.2.1. An optical waveguide with a rectangular grating for distributed feedback.[2-5]
Upper: A corrugated section of a dielectric waveguide.
Lower: The incident and reflected fields.

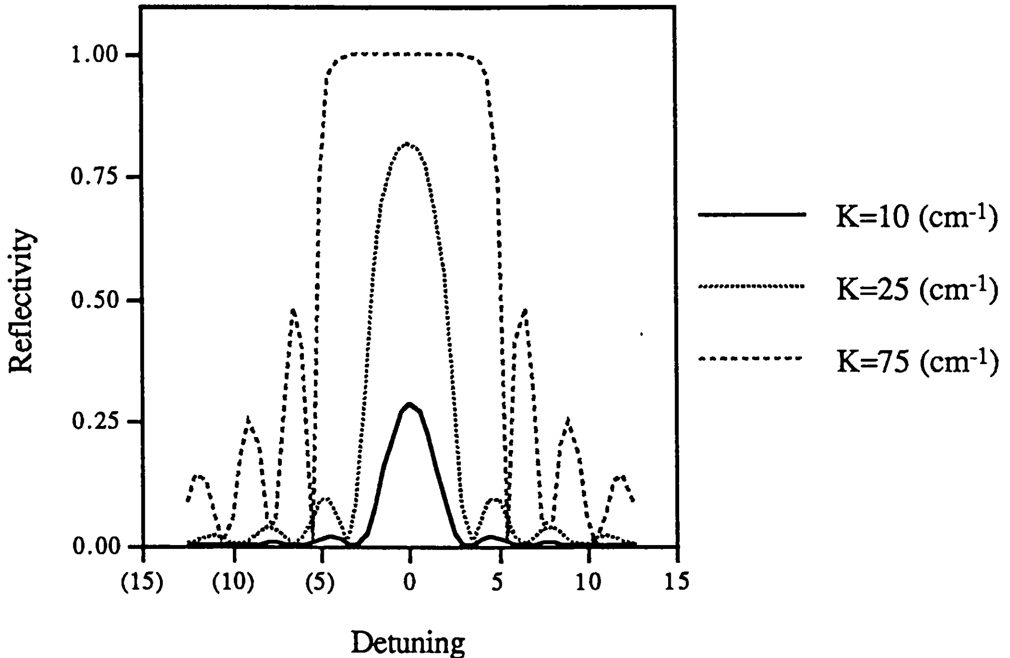

Fig.2.2. Calculated reflection characteristics of a grating length L (L=600 μm) as a function of the detuning $\Delta\beta L = [(\omega-\omega_0)L/c]n_{eff}$.

2.3. Lasing with distributed feedback

If the medium in which the wave is travelling has optical gain, such as in the inverted population region of a laser diode, the distributed feedback can result in lasing. In a medium with an exponential gain constant γ, the amplitudes of the incident and reflected waves are given by the expressions[2-6]

$$E_i(z) = E_0 \frac{e^{-i\beta_0 z}\{(\gamma - i\Delta\beta)\sinh[S(L-z)] - S\cosh[S(L-z)]\}}{(\gamma - i\Delta\beta)\sinh(SL) - S\cosh(SL)} \qquad [2.12],$$

and

$$E_r(z) = E_0 \frac{\kappa e^{i\beta_0 z}\sinh[S(L-z)]}{(\gamma - i\Delta\beta)\sinh(SL) - S\cosh(SL)} \qquad [2.13],$$

where

$$S^2 = \left|\kappa^2\right| + (\gamma - i\Delta\beta)^2 \qquad [2.14]$$

The parameter E_0 is the amplitude of a single mode (the one for which the net gain is greatest) incident on the grating of length L at z=0, while $\Delta\beta$ is given by

$$\Delta\beta = \beta - \beta_0 \qquad [2.15]$$

where β_0 is the propagation constant at the Bragg wavelength.

The oscillation condition for the DFB laser corresponds to the case for which both the transmittance $E_i(L)/E_i(0)$ and the reflectance $E_r(0)/E_i(0)$ become infinite. From Eqns. [2.12] and [2.13], it can be shown that this condition is satisfied when

$$(\gamma - i\Delta\beta)\sinh(SL) = S\cosh(SL) \qquad [2.16]$$

In general, Eqn. [2.16] can be solved to determine the threshold values of $\Delta\beta$ and γ, only by numerical solution.

The calculated reflection gain, $\left|E_r(0)/E_i(0)\right|^2$, for the condition of κ=10 cm^{-1} and L=600 μm is shown in Fig.2.3 and the calculated relationship between the gain constant γ and the detuning $\Delta\beta$ from the Bragg frequency is shown in Fig.2.4.

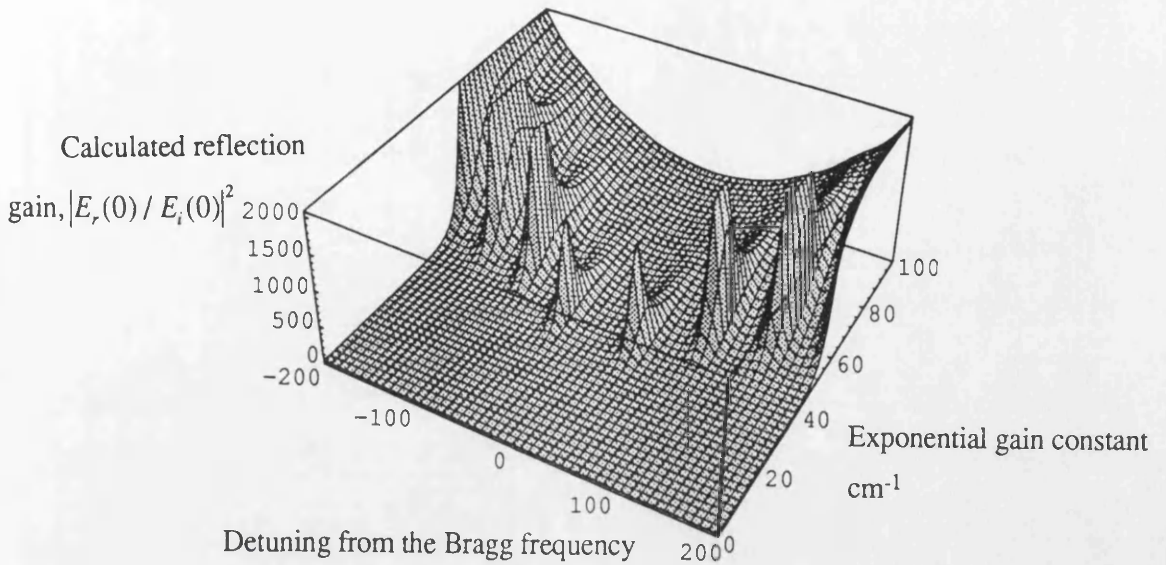

Fig.2.3. Calculated reflection gain, $|E_r(0)/E_i(0)|^2$, for the conditions κ=10 cm^{-1} and L=600 μm.

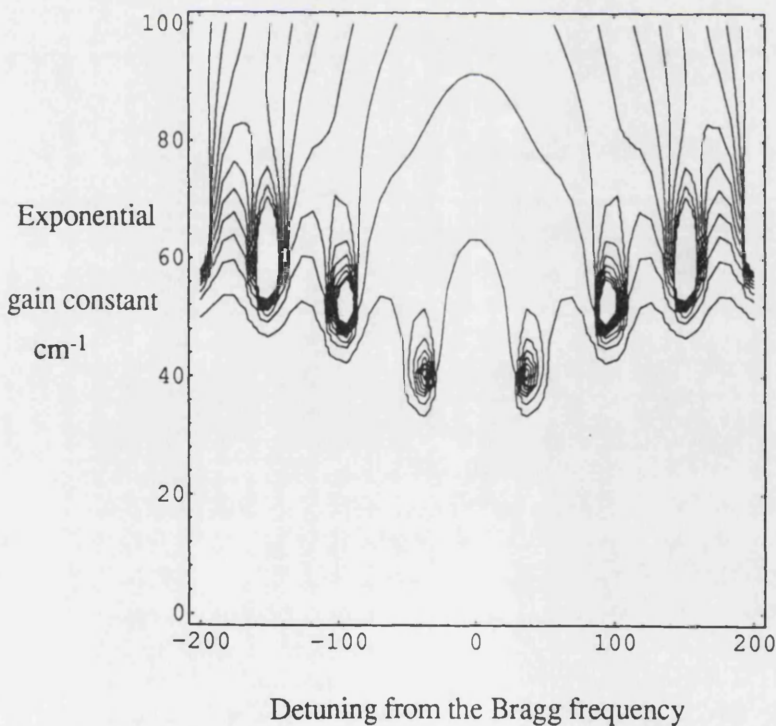

Fig.2.4. Calculated relationship between the gain constant γ and the detuning from the Bragg frequency $\Delta\beta$ (κ=10 cm^{-1} and L=600 μm).

2.4. Coupling coefficient κ

Using the coupled-mode theory, Yariv[2-4] has derived the coupling coefficient κ for a buried grating waveguide. For the surface grating waveguide, generally, the coupling coefficient is smaller than the coupling coefficient of the buried grating waveguides, because of the weaker mode coupling. An approximate calculation of the coupling coefficient of the surface grating waveguide, as shown in Fig.2.5, can be made from the change in effective index Δn_{eff} between the etched and unetched portions of the waveguide. The appropriate coupling coefficient κ is given by

$$\kappa = \frac{2\Delta n_{eff}}{m\lambda}\sin(\pi m\frac{w}{\Lambda}) \qquad [2.17]$$

where m is the order of the grating, λ is the lasing wavelength, W is the width of the grating teeth and Λ is the grating period. The dependence on the order of the grating m is represented by the multiplicative factor $\frac{\sin(\pi m w/\Lambda)}{m}$.[2-7] In the case of odd numbered order grating waveguides, the coupling coefficients is a maximum for 1:1 mark space ratio gratings.

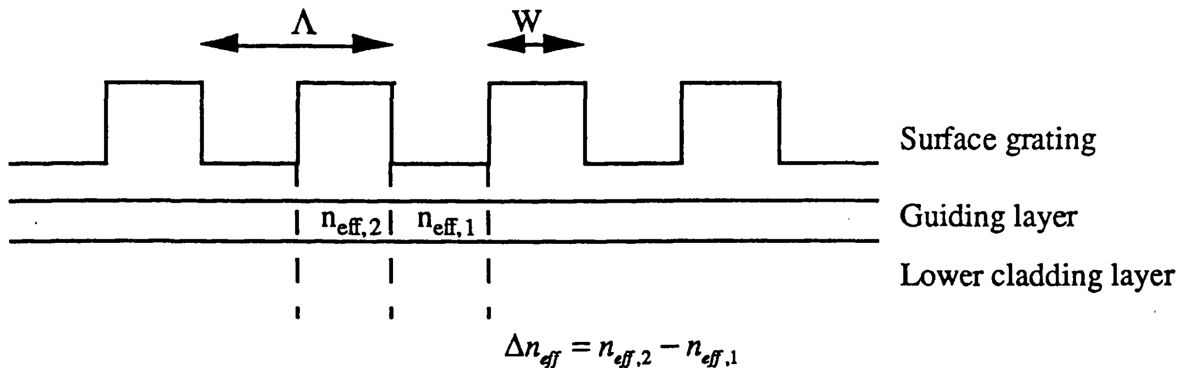

Fig.2.5. Schematic of the surface grating waveguide.

The change in the effective index Δn_{eff} can be estimated using the effective index method.[2-8, 2-9] Fig.2.6 shows models for calculation of the change of the effective index Δn_{eff}. Here W is the stripe width of the surface grating waveguide and T is the etched depth. The thickness of the upper cladding layer is assumed to be 0.7μm. The refractive index of each layer can be calculated using equations given by S.Adachi.[2-10] The calculated relationship between the coupling coefficient κ and the stripe width of the surface grating waveguide with the 3rd order gratings is shown in Fig.2.7. The calculated relationship between the coupling coefficient κ and the depth of the gratings is also shown in Fig.2.8.

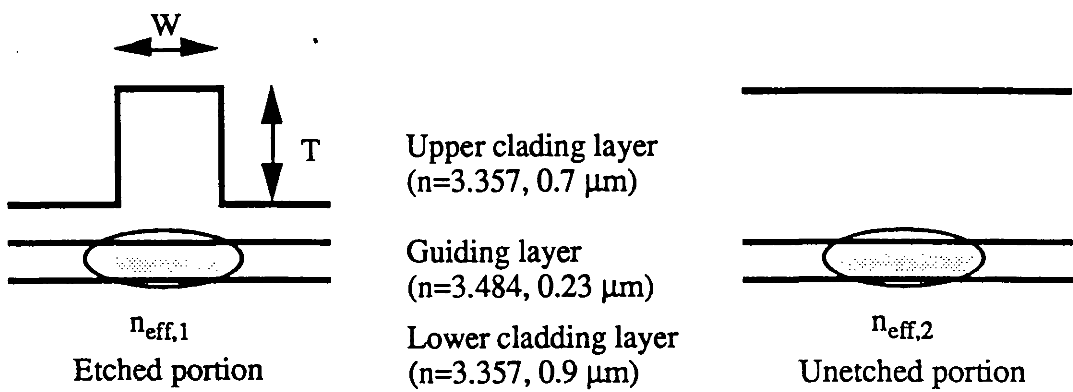

Fig.2.6. Calculation models of the etched and unetched portions surface grating waveguides.

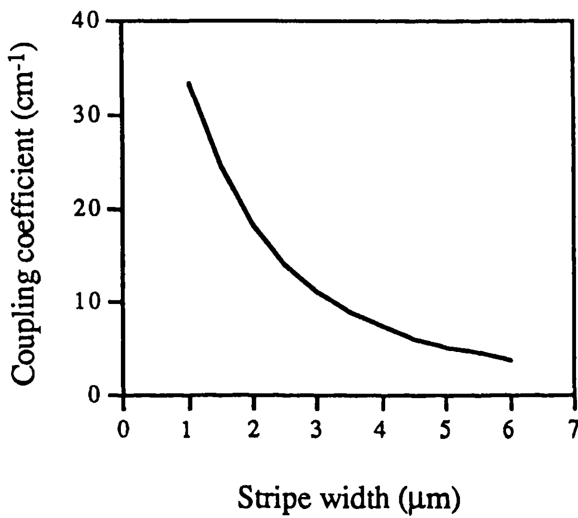

Fig.2.7. Calculated relationship between the coupling coefficient κ and the stripe width of the 3rd order surface grating waveguide. T=0.5 μm is assumed.

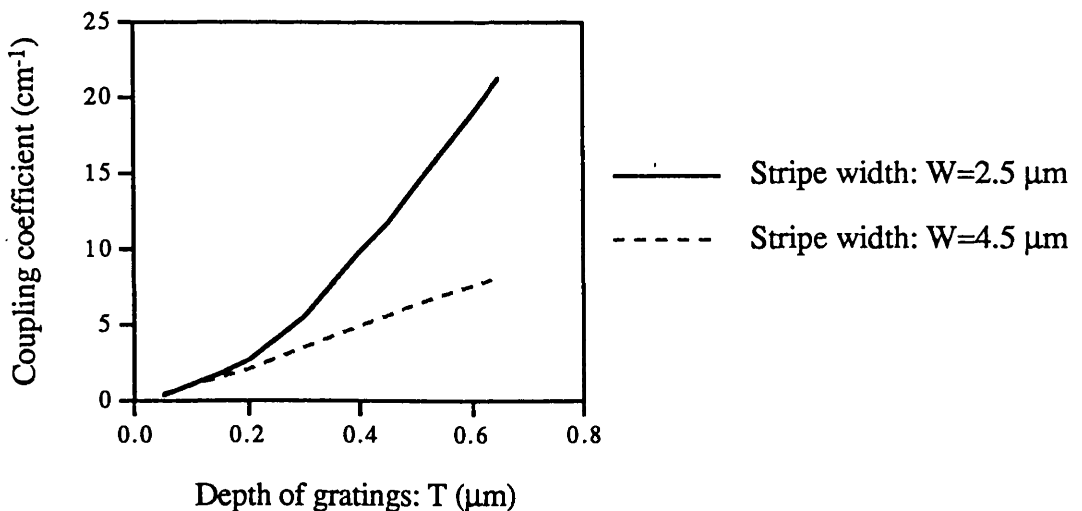

Fig.2.8. Calculated relationship between the coupling coefficient κ and the depth of the 3rd order gratings.

2.5. Non-uniform stripe lasers

Fig.2.9 shows a schematic diagram of a surface grating DFB non-uniform stripe lasers. Calculation of the threshold gain and the oscillation frequency for the DFB non-uniform stripe lasers, is based on the following coupled-mode equations:[2-4, 2-11]

$$-dA / dz + (\alpha - j\delta)E_A = j\kappa E_B \quad [2.18]$$

$$dB / dz + (\alpha - j\delta)E_B = j\kappa E_A \quad [2.19]$$

where

$$\delta = \beta - \pi / \Lambda \quad [2.20]$$

$$\beta = 2\pi n_{eff} / \lambda \quad [2.21]$$

In these Eqns., E_A and E_B are the amplitudes of the forward and backward wave, respectively and z is the position co-ordinate along the laser axis. α and κ are the loss and the coupling coefficient, respectively. δ means the deviation of the propagation constant β from the grating vector π / Λ. n_{eff} is the effective index and λ is the oscillation wavelength in free space. When the frequency parameter δ is constant , Eqns. [2.18] and [2.19] can be solved analytically. But a variation in δ is caused by a change in n_{eff} at the non-uniform region. Accordingly, Eqns. [2.18] and [2.19] are usually solved numerically.

The F-matrix method[2-12, 2-13] is one of the reported numerical calculation methods. In this approach the waveguides are divided into short segments along the propagation path, and in each segment the gratings are assumed to be periodic, that is, parameters such as coupling coefficient, grating phase, deviations from the Bragg frequency and gain in the waveguide are independent of position z. The characteristics of almost periodic grating stripe waveguides can then be obtained by multiplying each F-matrix of a short segment with the proper grating phase conditions at the interface between two adjacent segments.

The threshold gain and the oscillation frequency for the DFB non-uniform stripe lasers could be calculated using this F-matrix method, but this has not been carried out.

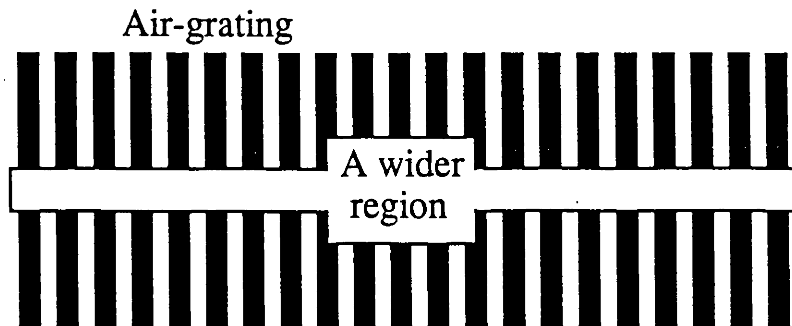

Fig.2.9. Schematic diagram of a surface grating DFB non-uniform stripe waveguide.

References

2-1. H.Kogelnik and C.V.Shank, "Coupled-wave theory of distributed feedback lasers", Journal of Applied Physics, Vol. 43, p. 2327-2335, 1972.

2-2. S.Wang, "Principles of distributed feedback and distributed Bragg-reflector lasers", IEEE Journal of Quantum Electronics, Vol. QE-10, p. 413-427, 1974.

2-3. W.Streifer, R.D.Burnham and D.R.Scifres, "Effect of external reflectors on longitudinal modes of distributed feedback lasers", IEEE Journal of Quantum Electronics, Vol. QE-11, p. 154-161, 1975.

2-4. A.Yariv, "Coupled-mode theory for guided-wave optics", IEEE Journal of Quantum Electronics, Vol. QE-9, p. 919, 1973.

2-5. A.Yariv and M.Nakamura, "Periodic Structures for Integrated Optics", IEEE Journal of Quantum Electronics, Vol. QE-13, p. 233-253, 1977.

2-6. R.G.Hunsperger, "Integrated optics: theory and technology", Springer-Verlag, p. 220-226, 1991.

2-7. W.Streifer, D.R.Scifres and R.D.Burnham, "Coupling coefficients for distributed feedback single- and double-heterostructure diode lasers", IEEE Journal of Quantum Electronics, Vol. QE-11, p. 867-873, 1975.

2-8. V.Ramaswamy, "Stripe-loaded film waveguide", Bell System Technical Journal, Vol. 53, p. 697-704, 1974.

2-9. P.K.Tien, "Light waves in thin films and integrated optics", Applied Optics, Vol. 10, p. 2395-2413, 1971.

2-10. S.Adachi, "GaAs, AlAs, and $Al_xGa_{1-x}As$: material parameters for use in research and device applications", Journal of Applied Physics, Vol. 58, p. R1-R29, 1985.

2-11. K.Tada, Y.Nakane and A.Ushirokawa, "Proposal of a distributed feedback laser with nonuniform stripe width for complete single-mode oscillation.", Electronics Letters, Vol. 20, p. 82-84, 1984.

2-12. M.Yamada and K.Sakuda, "Analysis of almost-periodic distributed feedback slab waveguides via a fundamental matrix approach", Applied Optics, Vol. 26, p. 3474-3478, 1987.

2-13. M.Okai, S.Tsuji and N.Chinone, "Stability of the longitudinal mode in $\lambda/4$-shifted InGaAsP/InP DFB lasers", IEEE Journal of Quantum Electronics, Vol. 25, p. 1314-1319, 1989.

Chapter 3 : Epitaxial wafer structure and analysis

In this chapter, the epitaxial wafer structure and analysis using broad area oxide stripe lasers are described.

3.1. Epitaxial wafer structure

The epitaxial wafer structure consists of two 0.01 μm GaAs quantum wells and 0.01μm $Al_{0.2}Ga_{0.8}As$ barriers and is shown in Fig.3.1.
The material was grown by MOCVD (Metal Organic Chemical Vapour Deposition) in University of Sheffield and identified as sample QT270.

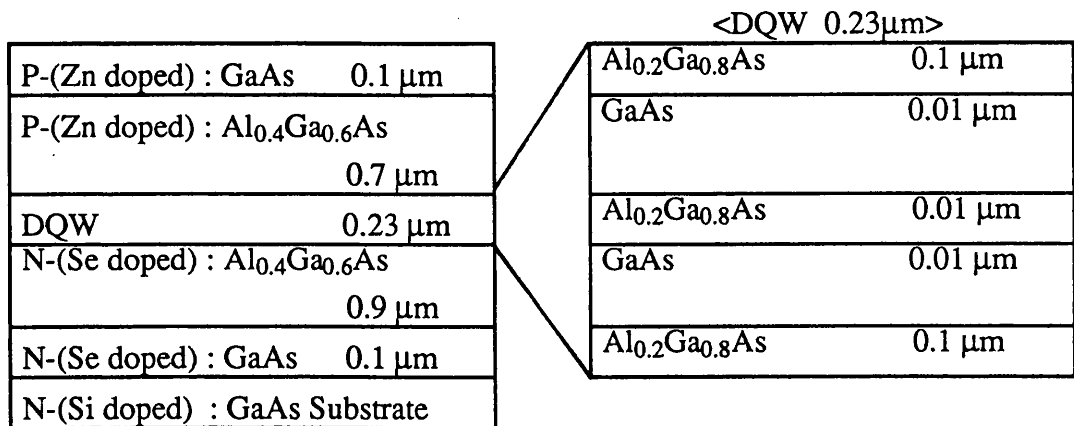

Fig.3.1. Schematic diagram of the epitaxial wafer structure (QT270).

3.2. Epitaxial wafer analysis using broad area oxide stripe lasers

It is important to have measured or estimated the emitting wavelength, internal loss α and internal quantum efficiency η_i of the epitaxial wafer before the fabrication of deep surface grating DFB stripe lasers. To analyse the epitaxial wafer parameters, broad area oxide stripe lasers were used because the effect of current spreading from the lasing region should be relatively small in such lasers. The approach in analysing the material was to fabricate 75 μm width oxide stripe lasers, cleave them into lengths from 400 μm to 1200 μm and measure the threshold currents for the devices that had the lowest threshold, followed by estimates of the external quantum efficiency η_e. The structure of the broad area oxide stripe lasers is shown in Fig.3.2.

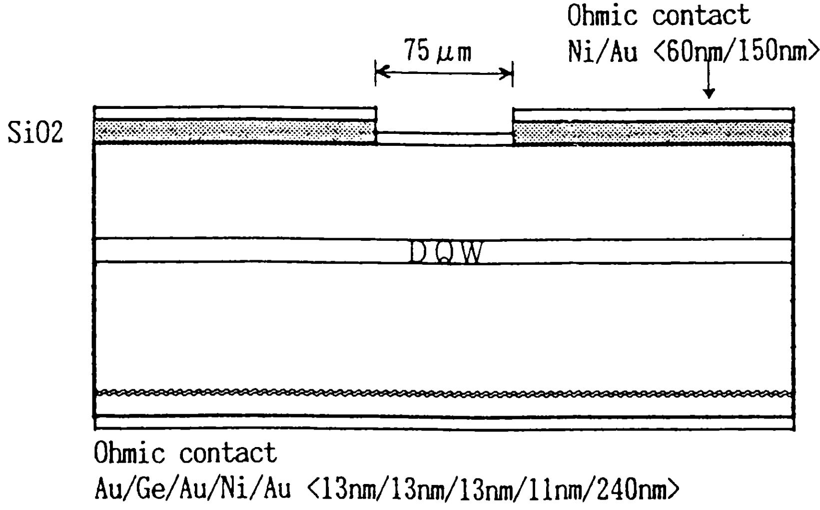

Fig.3.2. Schematic diagram of the broad area oxide stripe lasers.

3.2.1. Theory of epitaxial wafer analysis

The theory relevant to epitaxial wafer analysis is given in references 3-1 to 3-7.
In oxide stripe lasers, the following condition applies at threshold

$$g_{th} = \alpha + \frac{1}{L}\ln(\frac{1}{R}) \qquad [3.1]$$

The threshold gain g_{th} equals the sum of the losses, which are the internal loss α and the mirror loss $\frac{1}{L}\ln\frac{1}{R}$, where L is the cavity length and R is the average reflectivity of the facets. Above threshold, the gain is assumed to be clamped and the extra electrical power appears as light emission. The efficiency of conversion of electron power to photon power is given by

$$\eta_e = \eta_i(1-\frac{\alpha}{g_{th}}) \qquad [3.2]$$

where η_i is the internal quantum efficiency and η_e is the external quantum efficiency as measured by the slope of the light-current curve above threshold.
It has been found that the gain for a quantum well laser, taking account of the effect of light guided outside of the quantum wells, up to threshold can be related to the current density in the laser by the following relationship

$$g(J) = n\Gamma g_0 \ln(\frac{\eta_i J}{nJ_t}) \qquad [3.3]$$

where n is the number of quantum wells, Γ is the optical confinement per well, g_0 is the quantum well gain parameter for one well and J_t is the transparency current

which is needed in a well to overcome the resonant absorption. The optical confinement per well, Γ, is the fraction of the power within the well divided by the whole power carried by the laser mode, which is defined by

$$\Gamma = \frac{\int_{well} E(x)^2 dx}{\int_{waveguide} E(x)^2 dx} \qquad [3.4]$$

In broad area oxide stripe lasers, the approximate value of the optical confinement per well Γ can be calculated using a 2-dimensional waveguide model.
Fig.3.3 shows an illustration of Eqn. [3.3] and shows the relationship between the gain produced by quantum wells and the current density for material with different numbers of wells.

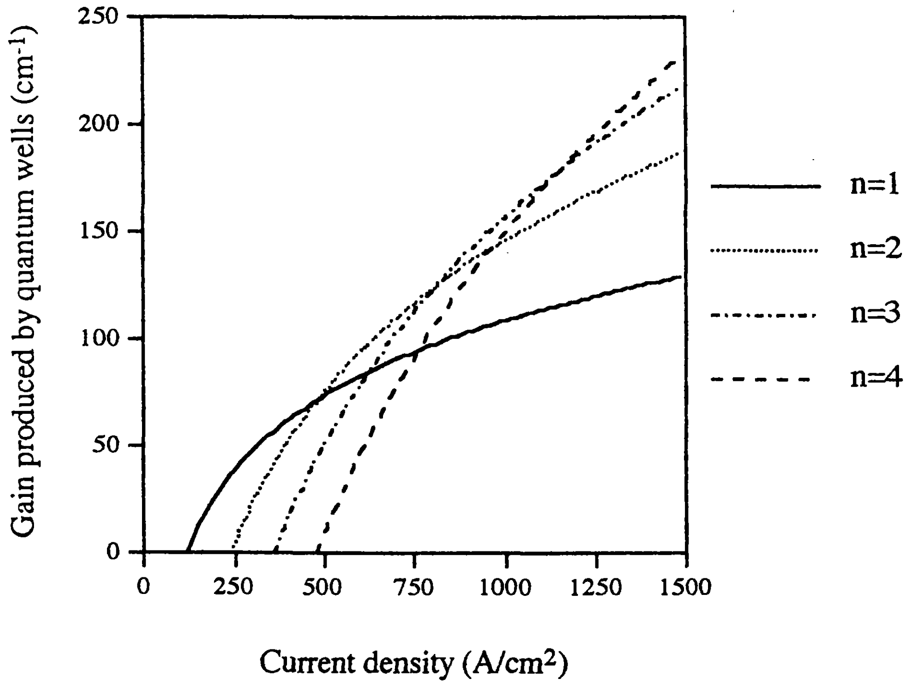

Fig.3.3. The calculated relationship between the gain, taking account of the effect of light guided outside of the quantum wells, and the current density for material with different numbers of wells using Eqn. [3.3]. Internal quantum efficiency η_i=1, transparency current J_t =120 A/cm^2, gain coefficient for one well g_0=1700 cm^{-1} and optical confinement per well Γ=3 % are assumed.

Combining [3.1] and [3.2] gives

$$\frac{1}{\eta_e} = \frac{1}{\eta_i} - L(\frac{\alpha}{\eta_i \ln R}) \qquad [3.5]$$

From a plot of the measured external quantum efficiency η_e against the cavity length L, the internal quantum efficiency η_i and the internal optical loss α can be estimated. Combining [3.3] and [3.5] gives

$$\ln(J_{th}) = \{\frac{\alpha}{n\Gamma g_0} + \ln(\frac{nJ_t}{\eta_i})\} - \frac{1}{L}(\frac{\ln R}{n\Gamma g_0}) \qquad [3.6]$$

A plot of the natural log of the threshold current density against inverse of the cavity length gives the gain factor $n\Gamma g_0$ from the slope and the intercept gives the transparency current J_t using the internal loss α calculated.
From these calculations, quantum well epitaxial wafers can be analysed.

3.2.2. Experimental results

To prevent excessive heating, the lasers were operated in pulsed current mode. The current pulse width was 400 nsec and the repetition rate was 1 kHz (duty cycle 1:2500). Fig.3.4 shows the measured L-I curves of the 400 μm, 600 μm, 800 μm, 1000 μm and 1200 μm cavity length broad area oxide stripe lasers, at 20 °C. The lasers had the lowest threshold currents among the five lasers within each category. Table 3.1 shows the external differential quantum efficiency for a single output facet, the threshold current and the threshold current density obtained from the L-I curves.

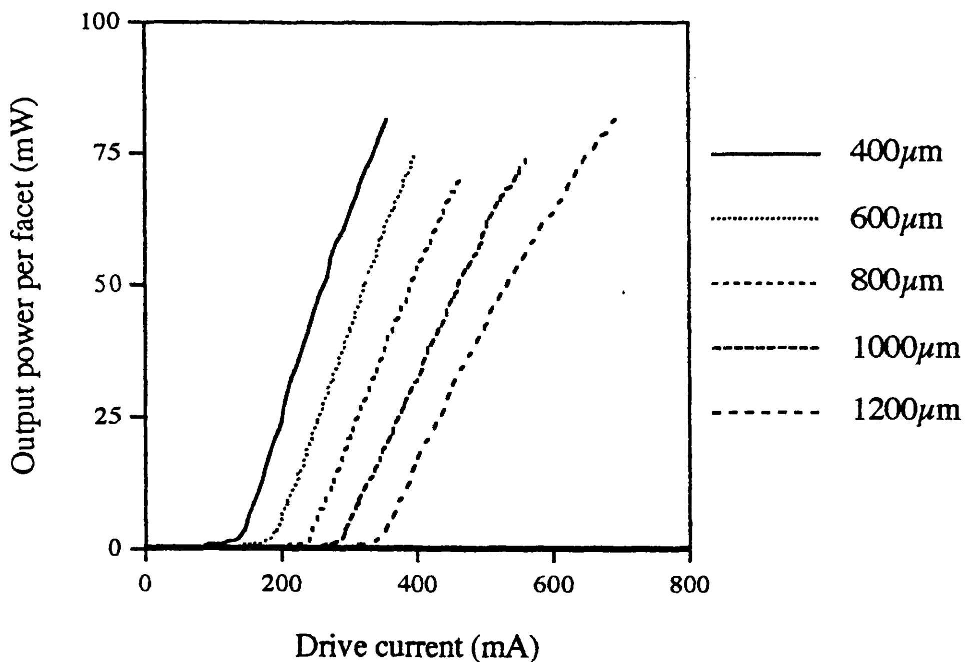

Fig.3.4. Measured output power per facet - drive current characteristics in broad area oxide stripe lasers.

Table 3.1. Measurement results for broad area oxide stripe lasers in pulsed operation, at 20 °C.

Cavity length (μm)	External differential quantum efficiency per facet (%)	Threshold current (mA)	Threshold current density (A/cm^2)
400	28	137	457
600	25	182	404
800	22	233	388
1000	19	281	375
1200	17	333	370

Fig.3.5 shows the spectra of the 400 μm and 600 μm cavity length broad area oxide stripe lasers at 20 °C. They lased multi-moded and the wavelengths were about 862nm.

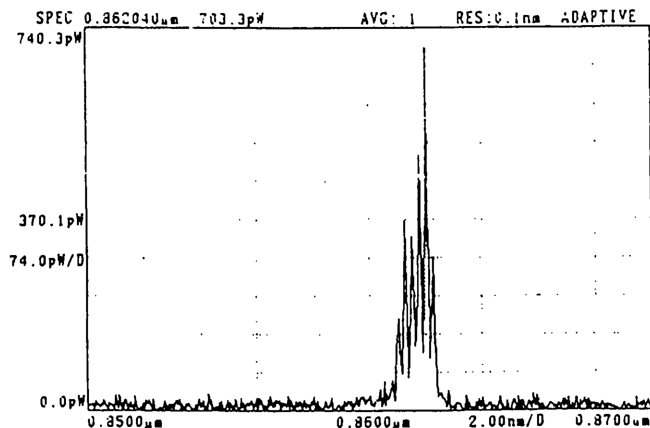

(A) 400μm cavity length broad area oxide stripe lasers, I=250 mA (ND 0.044).

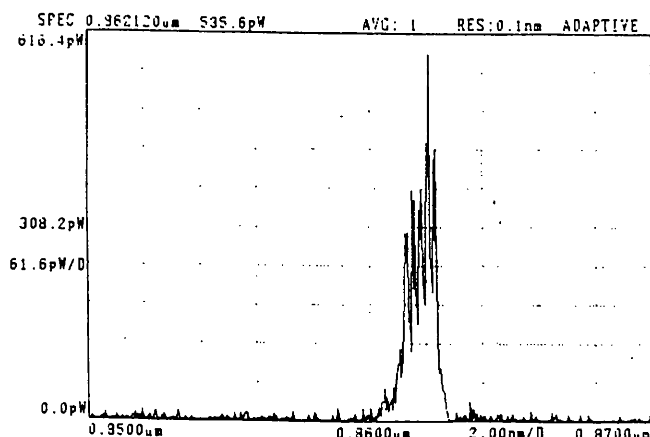

(B) 600μm cavity length broad area oxide stripe lasers, I=300 mA (ND 0.044).

Fig.3.5. Measured spectra of the 400 μm (A) and 600 μm (B) cavity length broad area oxide stripe lasers at 20 °C.

Fig.3.6 shows the relationship between the inverse of the external quantum efficiency and the cavity length obtained from the L-I curves along Eqn. [3.5]. The fit gave the internal quantum efficiency of 85% and the internal optical loss of 14.5 cm^{-1}. From Eqn. [3.4], optical confinement factors were calculated to be 22.2 % in the upper cladding layer, 55.5 % in the guiding layer, 22.3 % in the lower cladding layer and 2.73 % in one well (Γ=2.73 %) for the QT270 material structure using a 2-dimensional waveguide model.

Fig.3.7 shows the relationship between the natural log of the threshold current density and the inverse of the cavity length obtained from the L-I curves along Eqn. [3.6]. The fit gave $n\Gamma g_0$=92.6 cm^{-1} and $\ln(\frac{nJ_t}{\eta_i})$=5.64. From those data, the transparency current J_t and the quantum well gain parameter for one well g_0 were calculated to be J_t=120 A/cm^2 and g_0=1700 cm^{-1}. The epitaxial wafer parameters obtained from the analysis are shown in Table 3.2.

Table 3.2. The epitaxial wafer parameters obtained from the analysis.

Wavelength (nm)	η_i (%)	α (cm^{-1})	g_0(cm^{-1})	$J_{th,600\mu m}$ (A/cm^2)	J_t (A/cm^2)
862	85	14.5	1700	182	120

The internal quantum efficiency value and the optical internal loss value are good and therefore the material can be recognised to be good.

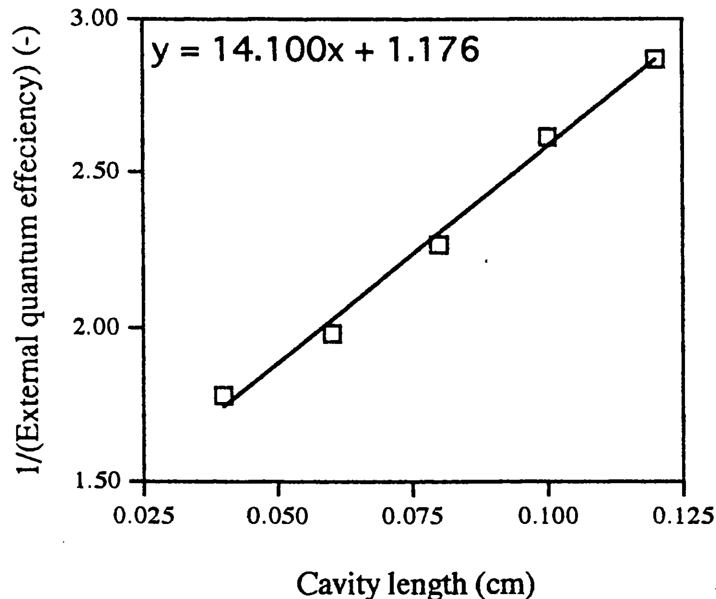

Fig.3.6. Relationship between the inverse of the external quantum efficiency and the cavity length obtained from the L-I curves according to Eqn. [3.5].

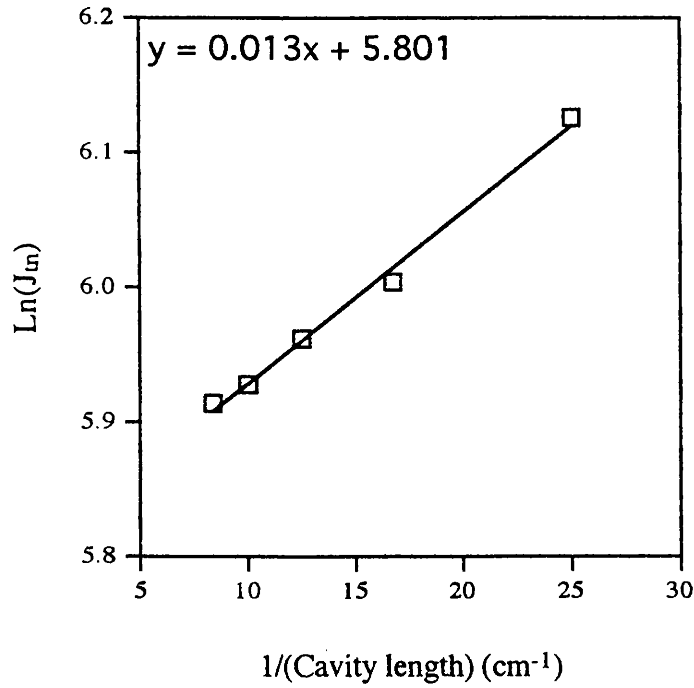

Fig.3.7. Relationship between the natural log of the threshold current density and the inverse of the cavity length obtained from the L-I curves according to Eqn. [3.6].

The temperature dependence of the spectra and the threshold current were measured as well. Fig.3.8 shows the temperature dependence of the spectra of the 400 μm and 600 μm cavity length broad area oxide stripe lasers. Because of the multi-moded emission, the plotted wavelength values were adopted from the centre of the multi-moded emission. The estimated temperature dependence of the spectra was about 0.28 nm/°C. Fig.3.9 shows the L-I curves for the 600 μm cavity length broad area oxide stripe lasers from 10 °C to 40 °C. It has been found the threshold current increases exponentially with temperature as

$$I_{th} = I_0 \exp(\frac{T}{T_0}) \qquad [3.7]$$

where T is the temperature (°C) and T_0 is the characteristic temperature.[3-8, 3-9] In GaAs/AlGaAs lasers, it has been found that the increase of the threshold current with temperature is due to the effects of gain spectrum broadening and overflow of carriers from a hetero-barrier.[3-10] Fig.3.10 shows the relationship between the natural log of the threshold current and temperature of the 400 μm and 600 μm cavity length broad area oxide stripe lasers obtained from the L-I curves using the equation [3.7]. From the slope values, the estimated characteristic temperature was about 150 K.

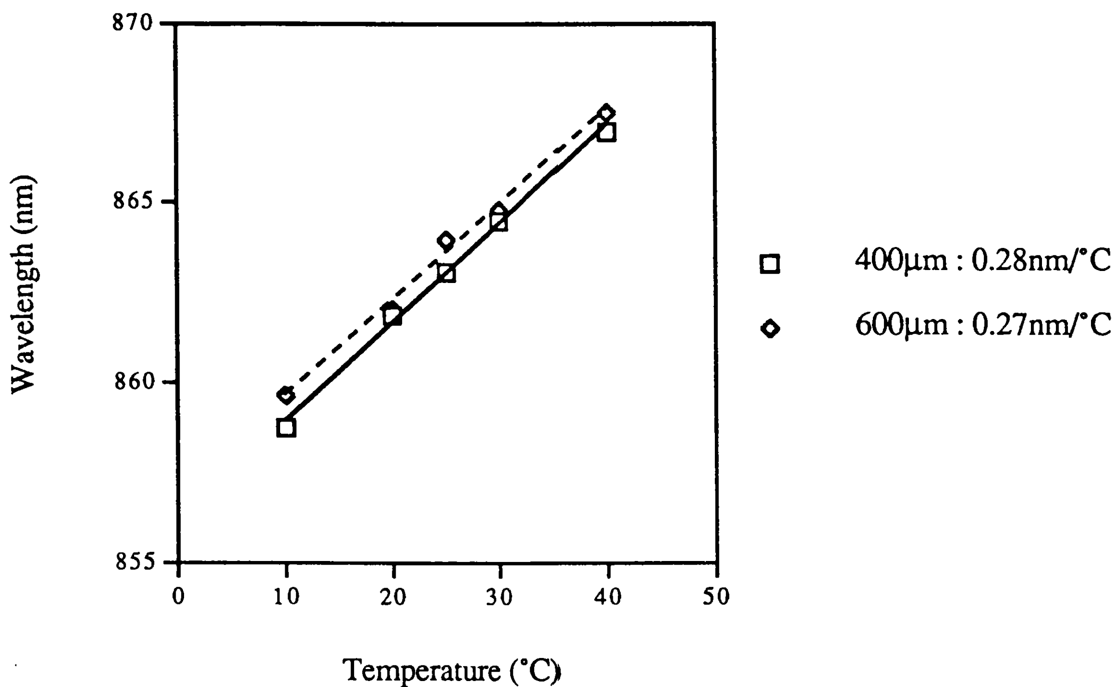

Fig.3.8. The temperature dependence of the spectra of the 400 μm and 600 μm cavity length broad area oxide stripe lasers.

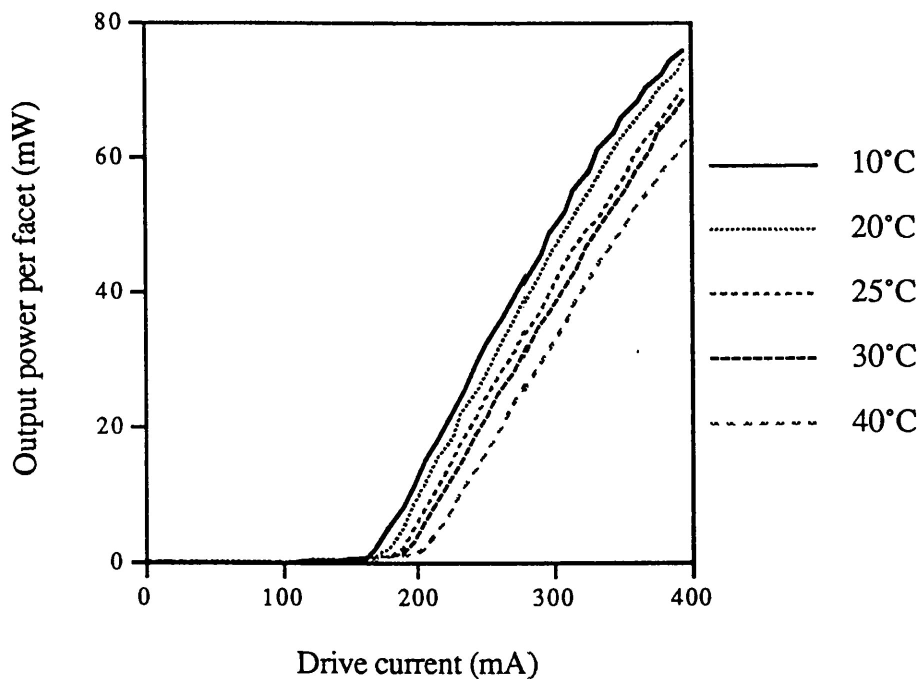

Fig.3.9. The L-I curves for the 600μm cavity length broad area oxide stripe lasers from 10 °C to 40 °C.

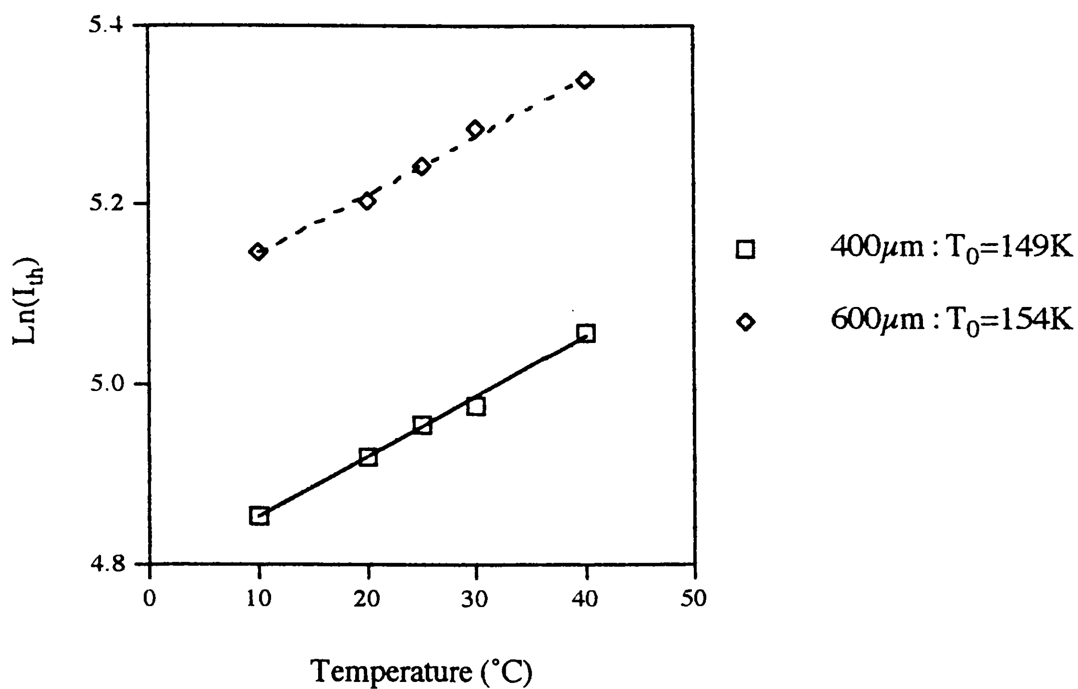

Fig.3.10. The relationship between the natural log of the threshold current and temperature of the 400 μm and 600 μm cavity length broad area oxide stripe lasers obtained from the L-I curves using the equation [3.7].

References

3-1. G.H.B.Thompson, "Physics of semiconductor laser devices", John Wiley and Sons., p. 97-105, 1980.

3-2. S.M.Sze, "Semiconductor devices physics and technology", John Wiley and Sons., p. 267-274, 1985.

3-3. A.Yariv, "Quantum electronics", John Wiley and Sons., p. 271-276, 1987.

3-4. P.Mc Ilory, A.Kurobe and Y.Uematsu, "Analysis and application of theoretical gain curves to the design of multi-quantum-well lasers", IEEE Journal of Quantum Electronics, Vol. QE-21, p. 1958-1963, 1985.

3-5. A.Kurobe, H.Furuyama, S.Naritsuka, N.Sugiyama, Y.Kokubun and N.Nakamura, "Effects of quantum well number, cavity length and facet reflectivity on the reduction of threshold current of GaAs/AlGaAs multiquantum well lasers", IEEE Journal of Quantum Electronics, Vol. 24, p. 635-639, 1988.

3-6. Y.Arakawa and A.Yariv, "Theory of gain, modulation response and spectral linewidth in AlGaAs quantum well lasers", IEEE Journal of Quantum Electronics, Vol. QE-21, p. 1666-1674, 1985.

3-7. J.Whiteaway, "Logarithmic gain/current-density characteristic of InGaAs/InGaAlAs/InP multi-quantum-well separate-confinement-heterostructure lasers", Electronics Letters, Vol. 27, p. 340-342, 1991.

3-8. S.M.Sze, "Semiconductor devices physics and technology", John Wiley and Sons., p. 274-278, 1985.

3-9. W.Tsang, "Low-current-threshold stripe-buried-heterostructure laser with self-aligned current injection stripes", Applied Physics Letters, Vol. 34, p. 644,1979.

3-10. T.Ohtoshi, "A two-dimensional device simulator of semiconductor lasers", Solid State Electronics, Vol. 30, p. 627-638, 1987.

Chapter 4 : Device structure and fabrication

In this section, the deep surface grating DFB stripe laser structure and the fabrication process for the lasers are presented.

4.1 Device structure

Fig.4.1 shows a schematic diagram of the deep surface grating DFB stripe lasers. To reduce current spreading, the GaAs contact layer was etched away in the grating regions. The cavity length was typically 600 μm. The grating was etched within 0.2μm (T=0.5 μm in Fig.4.1) of the active region and the width of the laser stripe was 2.5 or 4.5 μm. The grating period was about 0.38 μm, corresponding to 3rd order gratings. Surface grating DFB non-uniform stripe lasers were also fabricated with a wider region 4.5 μm wide and narrower regions 2.5 μm wide.

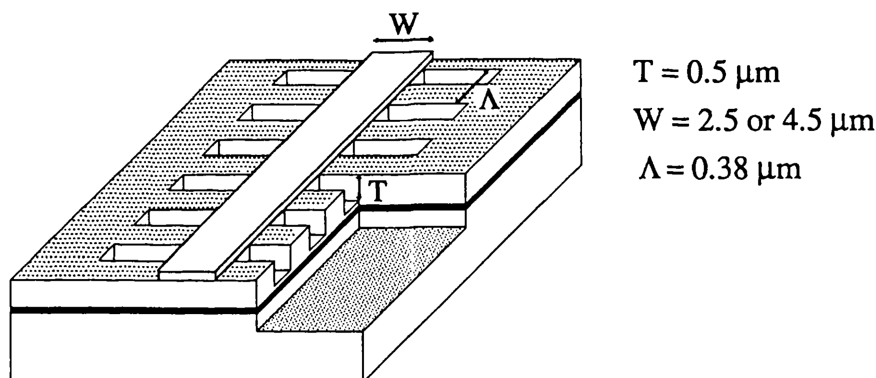

Fig.4.1. Schematic diagram of the deep surface grating DFB stripe lasers.

4.2 Fabrication

The fabrication requires several steps, which are briefly described as follows:

1. sample preparation:
   the wafer is cleaved into a rectangle of suitable size and cleaned using various solvents.
2. etching of the GaAs contact layer in the grating regions to reduce current spreading:
   after lithography using a mask aligner, the GaAs contact layer is etched away in the grating regions using wet etching in a solution of H_2O_2 and NH_4OH.
3. making gratings alongside the ridge:
   third-order gratings (Λ = 380 nm) are fabricated using the two beam interference method, shadow evaporation of NiCr and reactive ion etching.

4. making contact window and contacts:
   a contact window is opened by wet etching of the SiO_2 layer, which is deposited by Plasma Enhanced Chemical Vapour Deposition (PECVD). After suitable surface preparation, the final step is deposition and annealing of the contact metallisation.
5. cleaving and deposition of anti-reflection coatings:
   after cleaving the wafer section into suitable sizes for lasers, anti-reflection coatings consisting of a single Al_2O_3 layer are deposited by sputtering on both facets.
6. mounting and wire-bonding:
   the laser chip is mounted on a laser header and wire-bonded.

In this fabrication process, three masks fabricated by electron-beam lithography were used for etching the GaAs contact layer, definition of the grating regions and opening the contact window.

4.2.1 Sample preparation

Samples are cleaved into 8×12 mm^2 pieces, this size is the approximate size of the grating that can be produced in the holographic set up. The wafer section is prepared for lithography by cleaning for 5 minutes in subsequent ultrasonic baths of trichloroethylene, methanol and acetone, with a final rinse in reverse osmosis water.

4.2.2 Etching of GaAs contact layer in the grating regions

To reduce current spreading, the GaAs contact layer, which was 0.1 μm thick, was etched away in the grating regions. After lithography using a mask aligner, wet etching was carried out in a 20 : 1 solution of H_2O_2 and NH_4OH for 7 seconds. In this solution, the etching rate is quite different for GaAs and AlGaAs layers and the etching rate of AlGaAs layers is about 5 % of the etching rate of GaAs layers (1μm/min).[4-1, 4-2] So this solution was adopted.

4.2.3 Manufacture of gratings alongside the ridge

The device grating period was about 380 nm, corresponding to 3rd order gratings. When developing the fabrication techniques for deep surface gratings, 2nd order gratings in which the period was about 250 nm were also fabricated. Accordingly the fabrication of deep surface gratings is presented with 2nd order gratings as a particular example. The deep surface gratings were fabricated in 4 steps as follows:

(1) making sinusoidal resist patterns using the two beam interference method.
(2) making a shadow mask using NiCr shadowed evaporation.
(3) dry-etching of photoresist, anti reflective coatings (ARC), SiO_2 and GaAs layers.
(4) removing resist and ARC layers with N-methyl-2-pyrrolidone (NMP) and removing the SiO_2 layer with a solution of HF and RO water.

(1) The two beam interference method

Fig.4.2 shows a schematic diagram of the two beam interference method.[4-3, 4-4, 4-5] The period of the grating is defined by the incident angle θ_E of the argon laser. Spatial filters were inserted in order to improve spatial coherence. The power of the argon laser after the spatial filters was about 40 mW each. Samples were prepared as follows:

[1] deposition of SiO_2 film on top of the sample.
[2] spinning of ARC and baking.
[3] spinning of photoresist and baking.

ARC was used to prevent the formation of standing waves. Table 4.1 shows the conditions of spinning and baking.

Table 4.1. Conditions of coating ARC and resist.

	Ingredients	Maker	Spinning	Baking
ARC		Brewer Science Inc.	5000rpm for 60 seconds	130°C for 30 minutes
Resist	S1400-31(33%) Thinner (67%)	Shipley Inc.	4000rpm for 30 seconds	90°C for 30 minutes

In the case of fabrication of gratings alongside the ridge, patterning of the ridge and grating regions is executed by photolithography before exposure using the two beam interference method. After exposure by the two beam interference method, samples were developed in a 1 : 2 solution of the developer and RO water for 15 seconds. Fig.4.3 shows SEM photographs of resist patterns after each exposure time. Fig.4.4 shows a SEM photograph of resist patterns after exposure without ARC. Sinusoidal resist patterns are suitable because of the use of a shadowed evaporation angle.

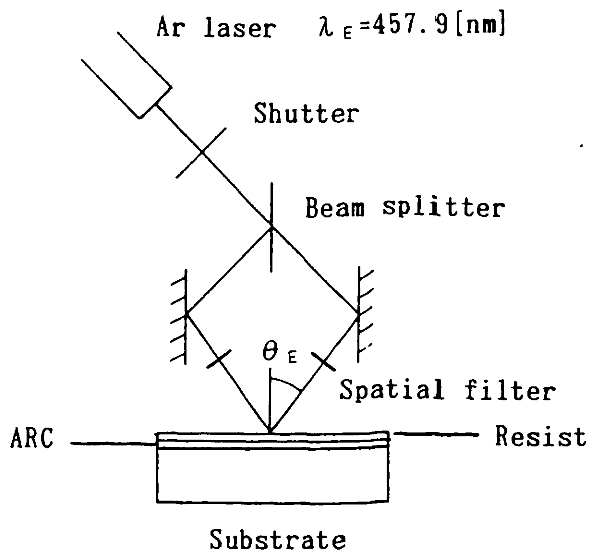

Fig.4.2. Schematic diagram of the two beam interference method.

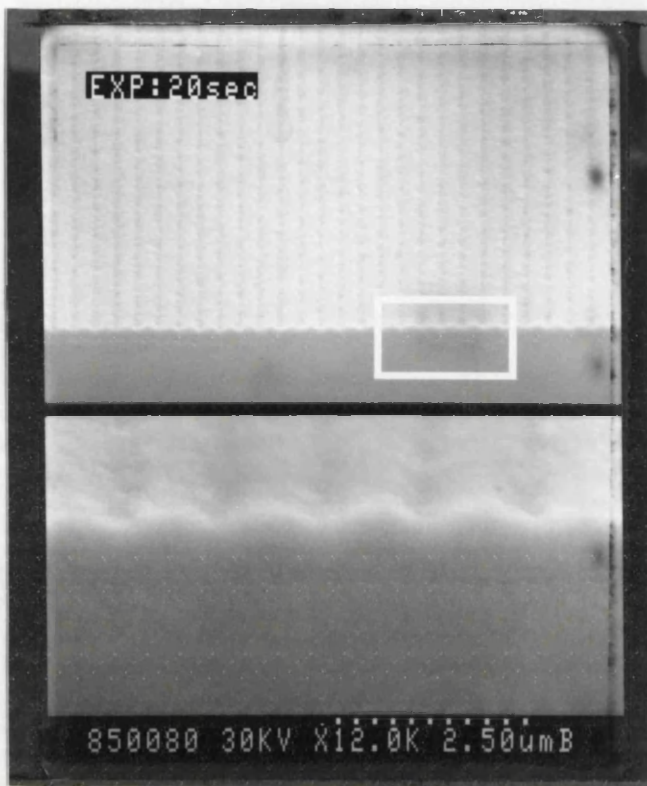

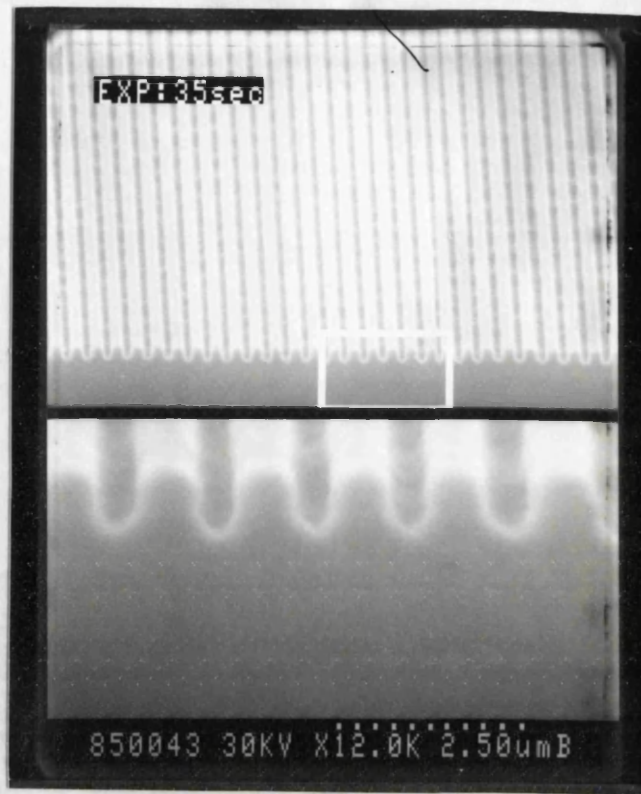

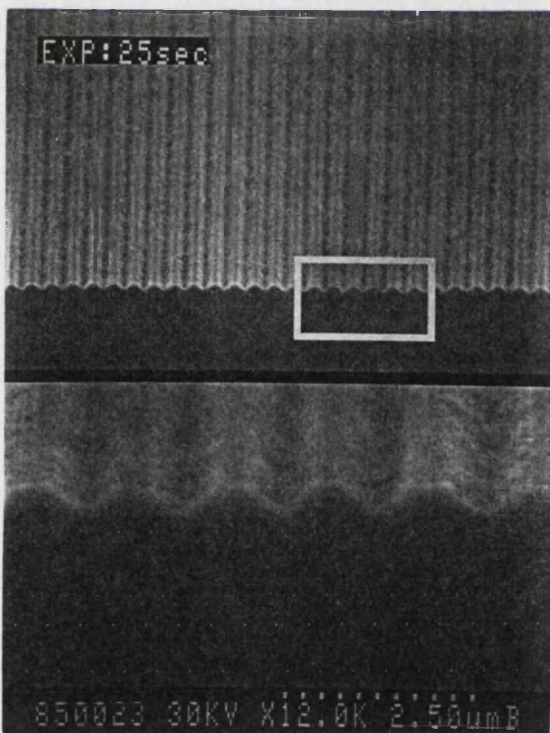

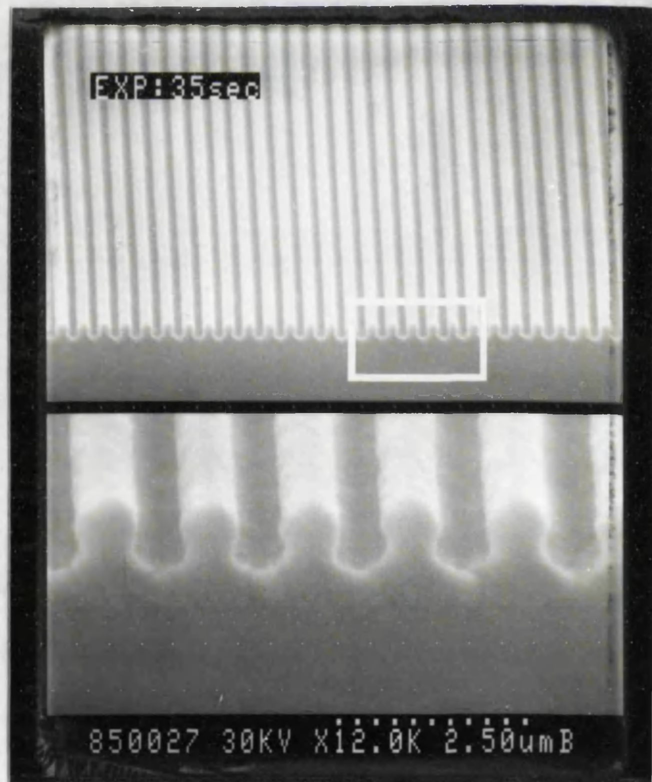

Fig.4.3. Change of grating profiles with increasing exposure time obtained by SEM observation. (Λ=285 nm).

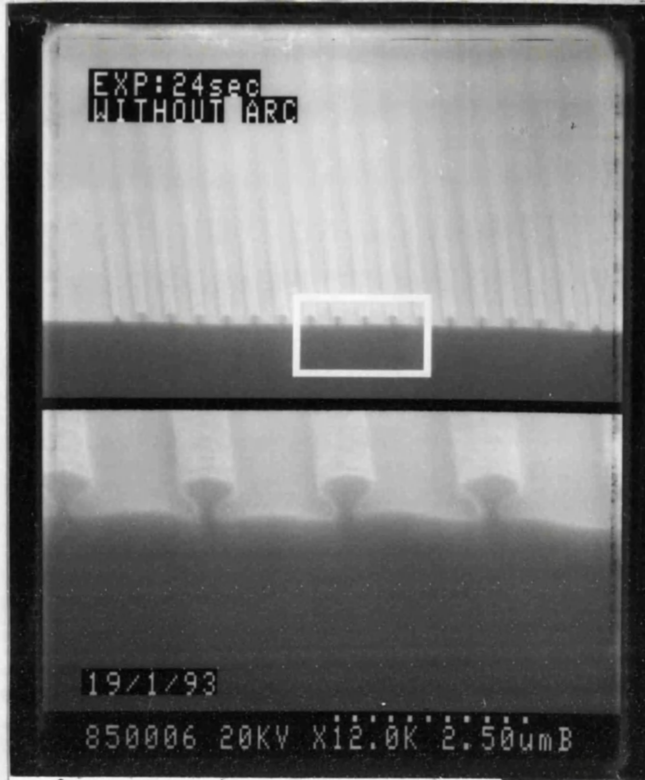

Fig.4.4. Resist patterns after exposure without ARC.

(2) NiCr shadowed evaporation

Fig.4.5 shows a schematic diagram of shadowed evaporation. When a resist pattern, after exposure using the two beam interference method, forms a sinusoidal pattern, a shadowing angle is calculated by Eqns. [4.1] and [4.2].

$$\theta = \frac{180}{\pi}\tan^{-1}\left(\frac{2\pi H}{\Lambda_G}\sin m \cdot \cos m\right) \quad [4.1]$$

$$m = \frac{\pi}{2} + \frac{1}{2}\tan^{-1}\left(\frac{\cos 2\pi K - 1}{\sin 2\pi K + 2\pi - 2\pi K}\right) \quad [4.2]$$

where H is the depth of the sinusoidal pattern, Λ_G is the period of the sinusoidal pattern and K is the mark-space ratio (K=A/Λ_G). The value of H was measured by SEM observation and it was about 0.2 μm. In the case of K=0.5 and Λ_G=0.38 μm, θ is calculated to be 42 °, but a smaller angle was used in practice because of difference centre positions between a sample and a metal boat.

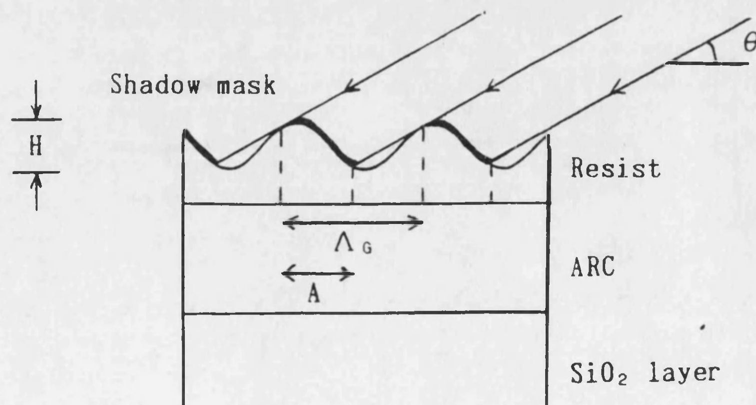

Fig.4.5. Schematic diagram of shadowed evaporation.

(3) Dry-etching resist, ARC, SiO_2 and GaAs layers

Resist and ARC layers were dry-etched with O_2 gas in a planar Reactive Ion Etching (RIE) plant. The SiO_2 layer was dry-etched with C_2F_6 gas and the GaAs layer was dry-etched with $SiCl_4$ gas.[4-6, 4-7, 4-8] Table 4.2 shows conditions for the RIE of resist, ARC, SiO_2 and GaAs layers.

Table 4.2. Conditions of reactive ion etching of resist, SiO_2 and GaAs layers.

	Gas	Gas flow (SCCM)	Pressure (mtorr)	RF power (W)	Etching rate (μm/min)	Etching time (min)
Resist	O_2	13	10	75	0.15	5
SiO_2	C_2F_6	20	14	100	0.04	8
GaAs	$SiCl_4$	6	8	100	0.06	10

Fig.4.6 shows SEM photographs of the 2nd order gratings after dry-etching of resist, ARC and SiO_2 layers. In order to keep the mark-space ratio close to unity, the shadowing angle should be controlled.
The RIE of GaAs/AlGaAs layers is anisotropic. $SiCl_4$ forms volatile reaction products with both GaAs and AlGaAs:

$SiCl_4$ + GaAs + AlGaAs $GaCl_w\uparrow + AsCl_x\uparrow + AlCl_y\uparrow + SiCl_z\uparrow$

This etch rate depends on 3 parameters: pressure, gas flow and RF power. The pressure and the gas flow are interrelated because the pump rate of the vacuum system is constant. The grating profile was changed by the gas flow. Fig.4.7 shows SEM photographs of the grating profiles for the condition of 6 SCCM and 9 SCCM $SiCl_4$ gas flow. In this fabrication process, 6 SCCM $SiCl_4$ gas flow was adopted. To dry-etch to the target value of depth accurately, test samples were used.

Fig.4.8 shows a SEM photograph of the fabrication result of the deep surface gratings. The dimensions are 0.5 μm etch depth, 0.38 μm grating period and 55 : 45 mark-space ratio. Fig.4.9 shows a SEM photograph of the deep surface grating uniform stripe waveguide and Fig.4.10 shows a SEM photograph of the deep surface grating non-uniform stripe waveguide. It was found that the width of the GaAs contact layer was a little bit narrower than the width of the surface grating stripe waveguide. As regards the surface grating non-uniform waveguide, the width of the narrow region was 2.5 $\pm$ 0.2 μm and the width of the wide region was 4.5 $\pm$ 0.2 μm.

Evaporate angle = 20[deg]

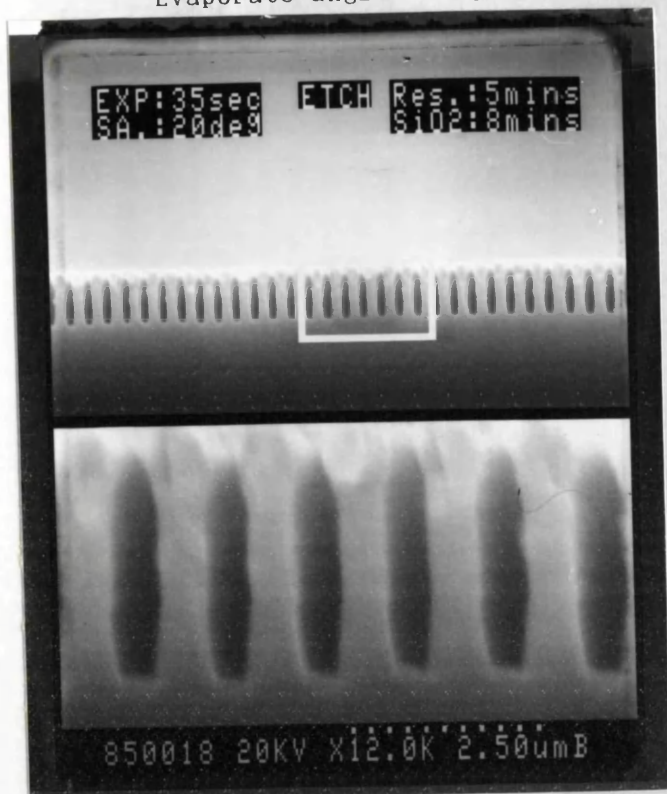

Evaporate angle = 30[deg]

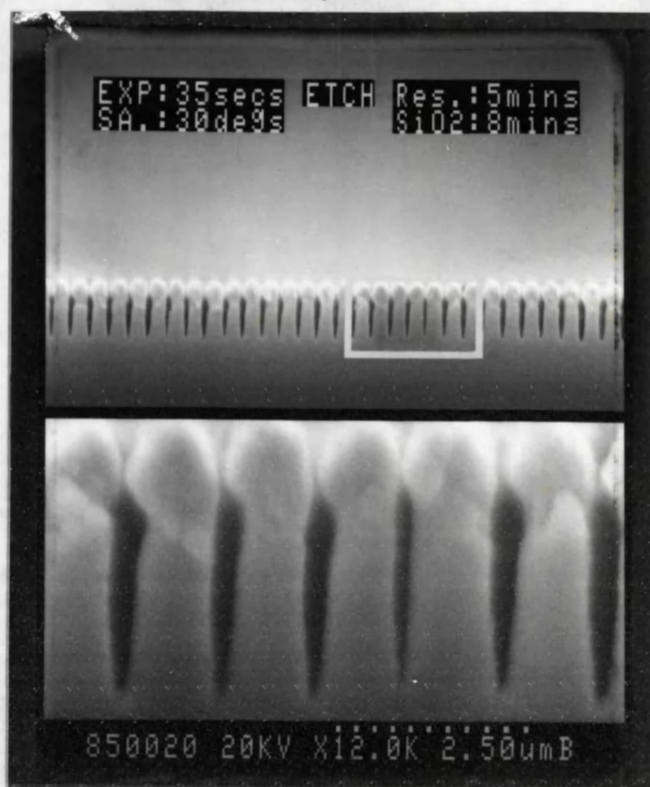

Evaporate angle = 25[deg]

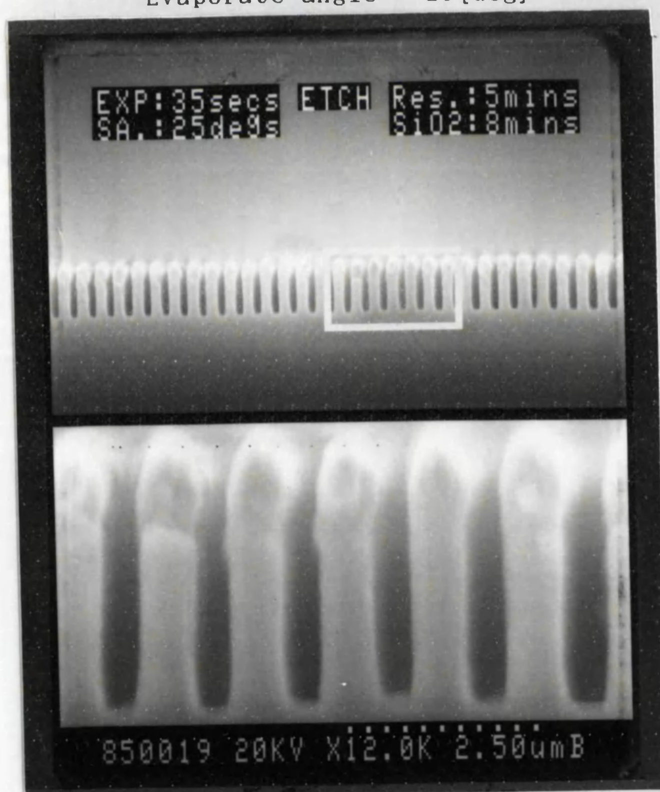

Shadowing angle (°)	Mark-space ratio
20	1 : 1
25	1.6 : 1
30	3.8 : 1

Fig.4.6. Change of mark-space ratio with increasing shadowing angle obtained by SEM observation (Λ_G = 250 nm).

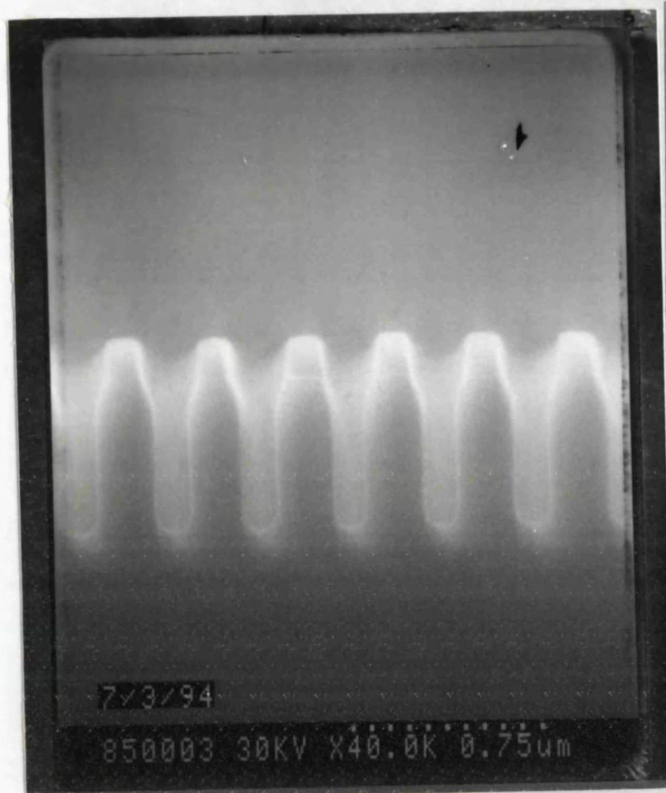

(A) 6 SCCM

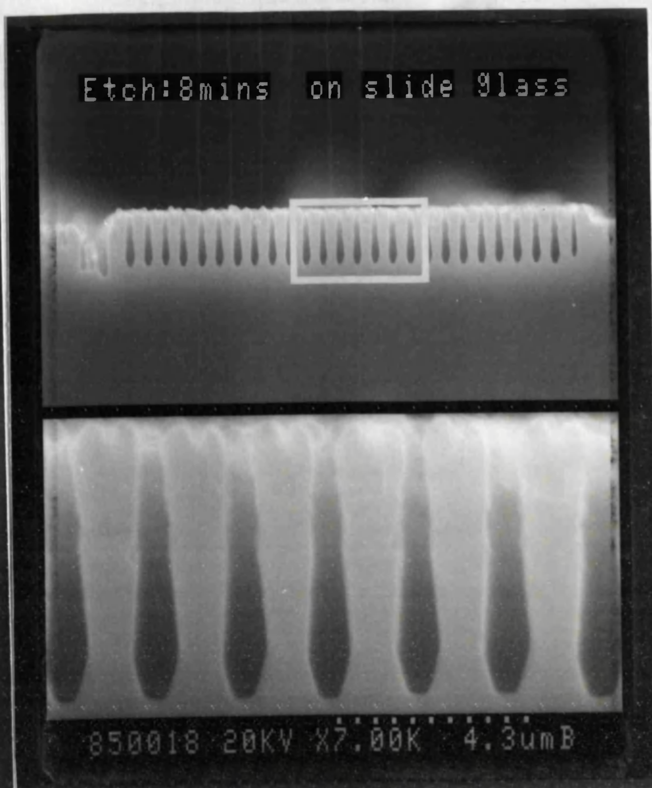

(B) 9 SCCM

Fig.4.7. SEM photographs of the grating profiles for the condition of 6 SCCM (A) and 9 SCCM (B) $SiCl_4$ gas flow.

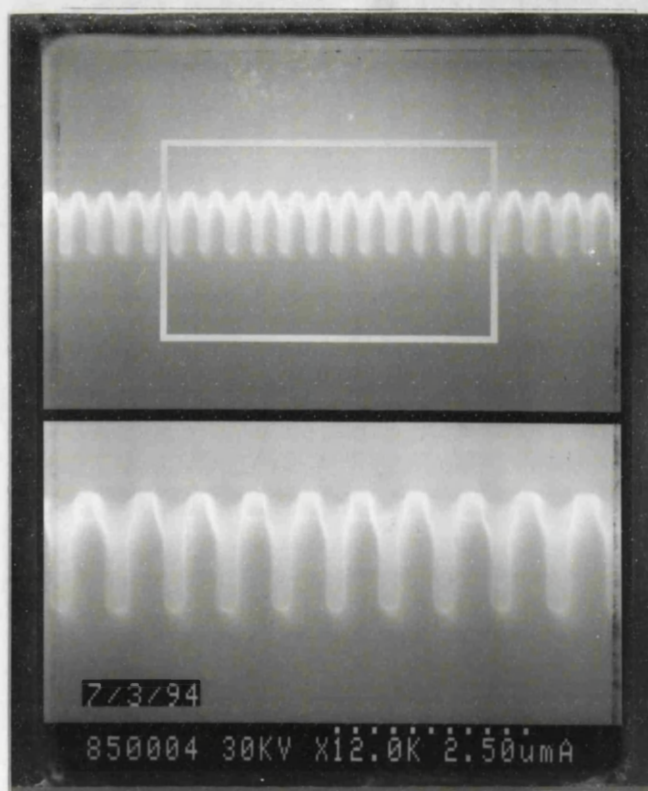

Fig.4.8. SEM photograph of the grating profiles

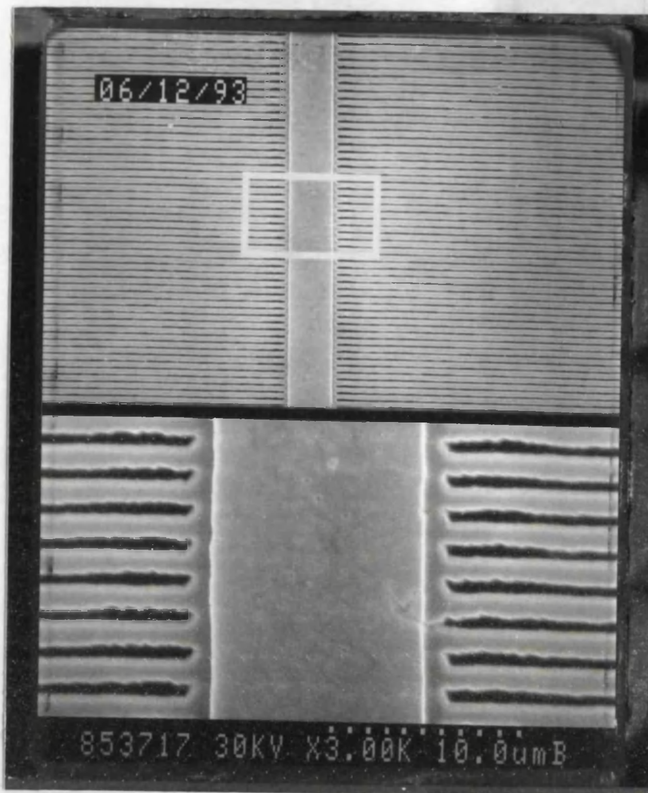

Fig.4.9. SEM photograph of the surface grating uniform stripe waveguide.

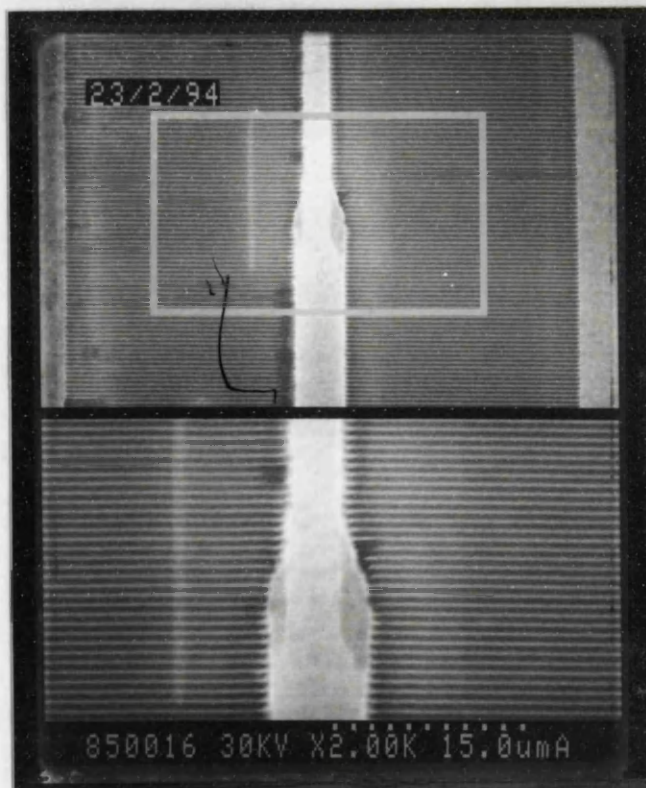

Fig.4.10. SEM photograph of the surface grating non-uniform stripe waveguide.

4.2.4 Making contacts

Three factors are important in the metallization of the wafer. First, the metal should adhere adequately, secondly it should provide a low resistance electrical contact, and thirdly it should not introduce excessive strain into the laser chip. Strain has a deleterious effect on laser life.[4-9]

During the processing steps, an oxide layer which acts as an insulator grows on top of the semiconductor . To remove this layer and prepare the semiconductor surface for the contact, various processes can be employed. For instance, bombardment with low energy Ar^+ ions has been carried out prior to the metal deposition.[4-10] In this fabrication process, wet etching was employed in a 1 : 2 solution of NH_4OH and RO water for 60 seconds.

The resistivity depends approximately exponentially on the height of the potential barrier between the metal and the appropriate band of the semiconductor, and also depends on the doping level, decreasing fairly rapidly as the doping level is increased.[4-11] When the barrier height is low, good contact can be obtained relatively easily by increasing the doping level and using a simple evaporated metallic layer. This applies to p-type contacts in GaAs where a p-doping level of greater than 3×10^{18} cm^{-3} may be used in conjunction with a well adhering metal.[4-12] The standard p-type contacts are as follows:

[1] Ti/Au (Schottky contact)
[2] Au/Zn/Au with annealing (ohmic contact)[4-13]
[3] Ti/Pt/Au with annealing (ohmic contact)[4-10, 4-14]
[4] Ni or Cr/Au (ohmic contact)[4-15]

In this present work, Ni(60 nm)/Au(150 nm) contacts were used.
When the barrier is lager, as in n-type GaAs, some form of alloying is necessary and Au/Ge/Ni/Au contacts with annealing have been used.[4-15] In the present work, an ohmic contact consisting of Au(13 nm)/Ge(13 nm)/Au(13 nm)/Ni(11 nm)/Au(240nm) was used, with annealing at 400 °C for 1 minute.

4.2.5 Deposition of anti-reflection (AR) coatings

To prevent Fabry-Perot mode oscillation, AR coatings consisting of a layer of Al_2O_3 or silicon nitride[4-16] were deposited on both facets. The film thickness satisfying the minimum reflectivity d is given by

$$d = \frac{(2m-1)\lambda}{4n} \qquad [4.3]$$

where m is an integral number, λ is the lasing wavelength and n is the refractive index of the film. In this fabrication process, a single monolayer of sputtered Al_2O_3 was used. The refractive index of sputtered Al_2O_3 was about 1.85 and the target value of the thickness was 116 nm.

4.2.6 Mounting and wire-bonding

Mounting of the laser chip is also a process that needs care to avoid the introduction of stress. In general indium solder can be relied upon to yield, before excessive stresses arise. So indium solder was used for the mounting of the laser chips on gold-plated steel heat-sinks. Normally the laser chips were mounted p-side down. Wire-bonding to the n-type contacts was performed using 25 μm diameter gold wire and an ultrasonic wire bonder.

A SEM photograph of the deep surface grating DFB stripe lasers is shown in Fig.4.11 and the wire-bonded laser chip is also shown in Fig.4.12.

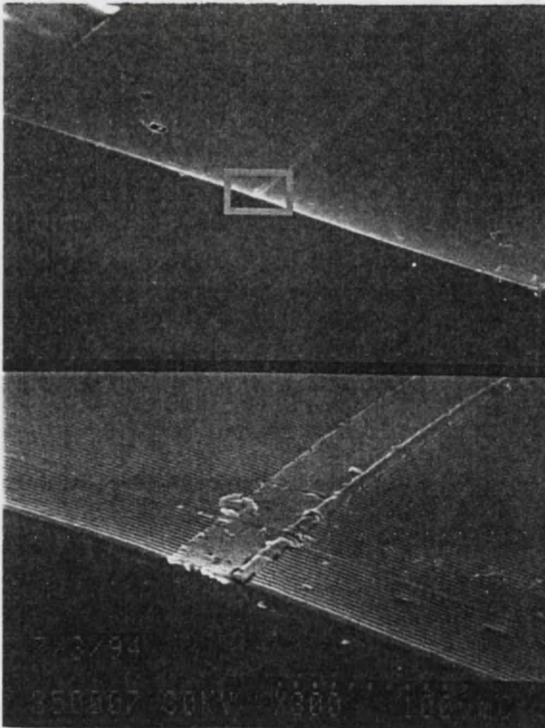

Fig.4.11. SEM photograph of the deep surface grating DFB stripe lasers.

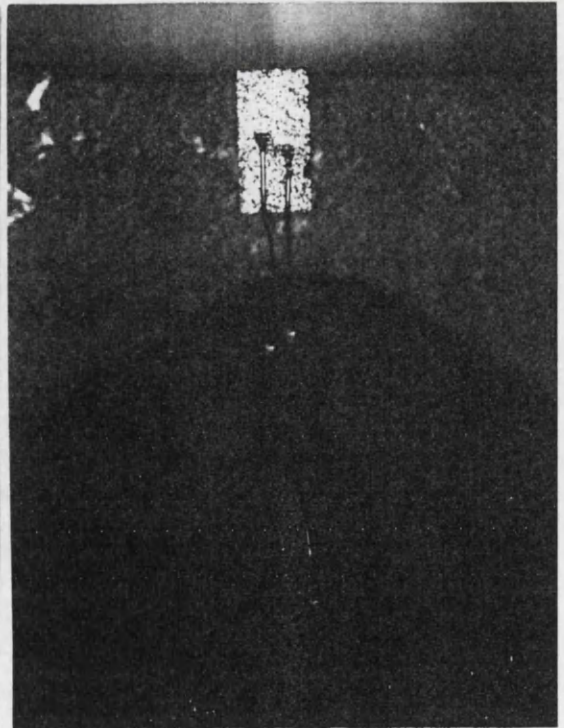

Fig.4.12. Photograph of the wire-bonded laser chip. (× 30)

References

4-1. S.M.Sze, "Semiconductor devices physics and technology", John Wiley and Sons., p. 428-457, 1985.

4-2. C.C.Chang, P.H.Citrin and B.Schwartz, "Chemical preparation of GaAs surfaces and their characterization by auger electron and x-ray photoemission spectroscopies", Journal of Vacuum Science and Technology, Vol.14, p. 943-952, 1977.

4-3. A.Yariv and M.Nakamura, "Periodic Structures for Integrated Optics", IEEE Journal of Quantum Electronics, Vol. QE-13, p. 233-253, 1977.

4-4. A.Yariv, "Holographic interference lithography for integrated optics", IEEE Trans. Electron Device, Vol. ED-25, p. 1193, 1974.

4-5. K.Kodate, T.Kamiya, H.Takenaka and H.Yanai, "Analysis of two dimensional etching effect on the profiles of fine holographic grating made of positive photoresist AZ2400", Japanese Journal of Applied Physics, Vol. 17, p. 123-128, 1978.

4-6. G.F.Doughty, "Dry etching of polymers, silica, glass and lithium niobate", Integrated Optical Technologies, p. 49-52, 1988.

4-7. S.Semura, Japanese Journal of Applied Physics, Vol.24, p. 463, 1985.

4-8. S.Thoms, "Ultra small device fabrication using dry etching of GaAs", Microelectronics Engineering, Vol. 5, p. 249-256, 1986.

4-9. G.H.B.Thompson, "Physics of semiconductor laser devices", John Wiley and Sons., p. 25-29, 1980.

4-10. G.Stareev, "Formation of extremely low resistance Ti/Pt/Au ohmic contacts to p-GaAs", Applied Physics Letters, p. 2801-2803, 1993.

4-11. C.Y.Chang, "Specific contact resistance of metal - semiconductor barriers", Solid State Electronics, Vol. 14, p. 541, 1971.

4-12. G.H.B.Thompson, "Physics of semiconductor laser devices", John Wiley and Sons., p. 23-24, 1980.

4-13. K.L.Klohn, Journal of Electrochem. Soc., Vol. 116, p. 507, 1969.

4-14. N.Braslan, Journal of Vacuum Science Technology, Vol. 19, p. 803, 1981.

4-15. T.Krauss, P.J.R.Laybourn and J.Roberts, "CW operation of semiconductor ring lasers", Electronics Letters, Vol. 26, P. 2094-2096, 1990.

4-16. M.Serenyi and H.U.Habermeier, "Directly controlled deposition of antireflection coatings for semiconductor lasers", Applied Optics, p. 845-849, 1987.

Chapter 5 : Measurements

In this section, the measurement methods, results and interpretation are described.

5.1 Measurement method

Among the important device characteristics measured were the following:

(1)Injection current - Voltage characteristics (I-V curves) and Light output power - Injection Current characteristics (L-I curves),

(2)Far field pattern,

(3)Laser spectra.

These parameters were measured in both pulsed and CW operation. In CW operation, the junction temperature generally rises significantly due to heating effects, so laser characteristics such as threshold current, external differential quantum efficiency and spectra change compared with pulsed characteristics. In pulsed operation, with duty cycle less than about 1 : 1000, the junction temperature does not change significantly. Pulsed measurements are therefore more accurate to evaluate laser characteristics, but laser characteristics in CW operation are at least as important because practical operation may be at or near CW conditions. Both measurements were therefore carried out.

The measurements carried out are summarised briefly below.

(1) Injection current - Voltage characteristic (I-V curve) and Light output power - Injection Current characteristic (L-I curve).

The resistances of the lasers were evaluated from I-V curves and the threshold current and slope efficiency were evaluated from L-I curves. These parameters are important laser characteristics. The measurement method used for L-I curves differed between pulsed operation and CW operation. Fig.5.1 shows the measurement system for L-I curves, in pulsed operation. The laser chip was injected with a pulsed current (duty cycle 1 : 2500), to prevent excessive heating of the chip. It was mounted on a brass clip. Optical power was measured by averaging the photocurrent for gate pulses of length 100 ns in electrical circuits to avoid the influences of delay time and relaxation [5-1] of laser emission. On the other hand, in CW operation, optical power was measured using an optical power meter.

(2) Far field pattern. .

Observation of the Far-field pattern was used to estimate the distribution of electromagnetic field in the laser waveguide and was measured in pulsed operation.

(3) Laser spectra.

Fig.5.2 shows the measurement system for laser spectra. The beam emitted by the laser chip was focused on the end of the multi-mode fibre input to the ADVANTEST Q8381 spectrum analyser, with objective lenses. The resolution of this spectrum analyser is about 0.2 nm.

In the case where the coupling coefficient κ is about 10 cm^{-1}, the stopband is about 0.25 nm wide. It is therefore difficult to observe the existence of the stopband using the spectrum analyser, and it is impossible to measure the linewidth of the spectrum of a DFB laser. A scanning Fabry-Perot interferometer method [5-2] can be used for observation of the existence of a stopband and measurement of the linewidth. Fig.5.3 shows the measuring system for the scanning Fabry-Perot interferometer method. It consists of two parallel, highly reflecting surfaces separated by an air gap which can be mechanically varied by moving one of the mirrors. The free spectral range of the interferometer $\Delta\lambda_{FP}$ is defined as follows[5-2]:

$$\Delta\lambda_{FP} = \frac{\lambda^2}{2nl} \qquad [5.1]$$

where n is the refractive index of air and l is the spacing of the Fabry-Perot interferometer cavity. For the measurement of the stopband, $\Delta\lambda_{FP}$ must be larger than $\Delta\lambda_{stopband}$, i.e.

$$\Delta\lambda_{FP} > \Delta\lambda_{stopband} \qquad [5.2]$$

This leads to the following condition for the spacing l of the Fabry-Perot interferometer cavity .

$$l < \frac{\lambda^2}{2n\Delta\lambda_{stopband}} \qquad [5.3]$$

With n = 1(air), λ = 860 nm and $\Delta\lambda_{stopband}$ = 0.25 nm, l is calculated to be < 1.48 mm. For the measurement of linewidth, the resolution of the apparatus is determined by the finesse F of the Fabry-Perot interferometer and the finesse depends on the reflectivity of the mirrors, as follows:

$$F = \frac{\pi\sqrt{R}}{1-R} \qquad [5.4]$$

where R is the intensity reflection coefficient, assumed the same at both ends of FP cavity. The resolution of the interferometer $\Delta\lambda_{Re}$ is defined by

$$\Delta\lambda_{Re} = \frac{\Delta\lambda_{FP}}{F} \quad [5.5]$$

In the Technical Optics Ltd. FPI - 25 scanning Fabry-Perot interferometer, the finesse is calculated to be 155 with R = 0.98 at λ = 860 nm and therefore the calculated minimum resolution is 2.4×10^{-5} nm (10MHz) at l = 10 cm. However, it is difficult to obtain this resolution in practice, because it requires very accurate alignment and collimation.

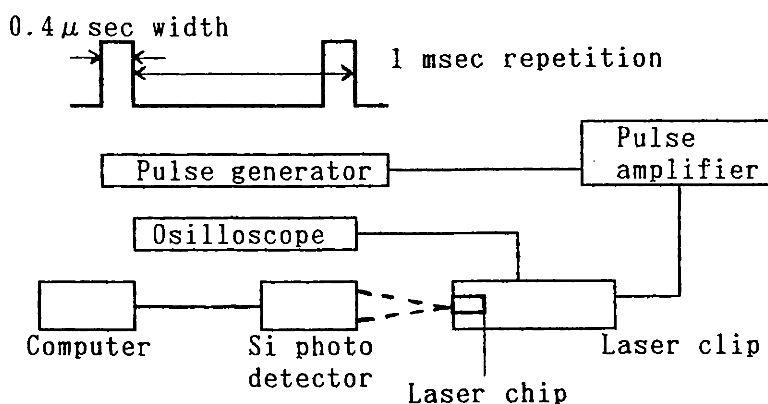

Fig.5.1. Schematic diagram of the measurement system for L-I curves in pulsed operation.

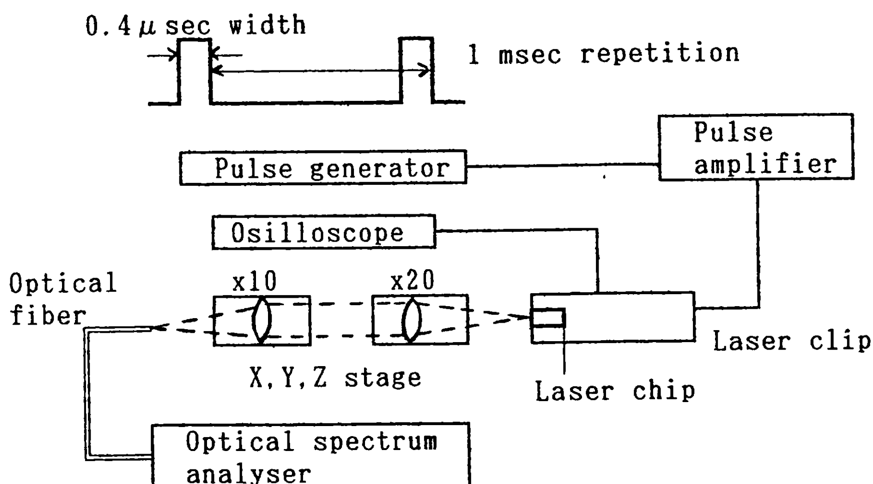

Fig.5.2. Schematic diagram of the measurement system for laser spectra.

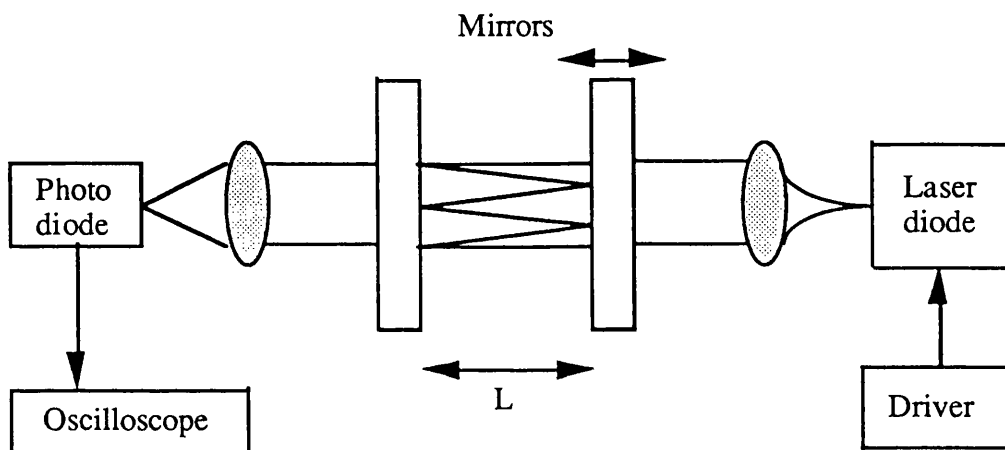

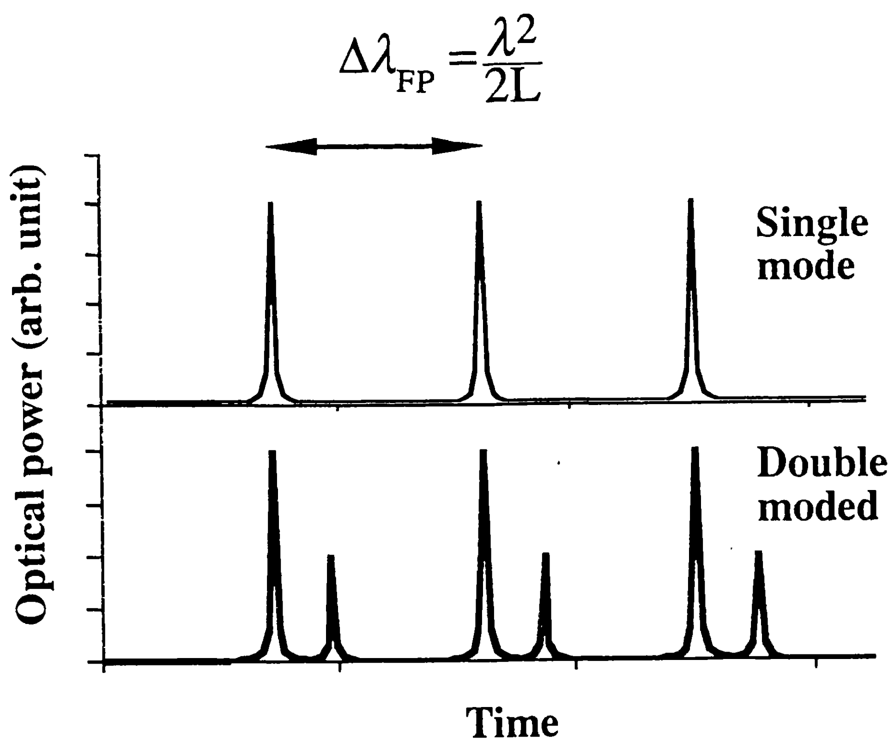

Fig.5.3. Schematic diagram of the measurement system for the scanning Fabry-Perot interferometer method.

5.2 Experimental results and interpretation

Narrow area oxide stripe lasers, surface grating DFB uniform stripe lasers and surface grating DFB non-uniform stripe lasers, fabricated from the same wafer, were evaluated. Measurements on narrow area oxide stripe lasers allowed estimation of internal loss and confirmation of the expected effects of using AR coatings. Results for devices under both pulsed operation and CW operation are described below.

5.2.1 Results for lasers in pulsed operation

The devices evaluated are categorised as follows:
(1) narrow area oxide stripe FP lasers without AR coatings (Stripe width 2.5μm),
(2) narrow area oxide stripe FP lasers with AR coatings (Stripe width 2.5μm),
(3) surface grating DFB uniform stripe lasers without AR coatings,
(4) surface grating DFB uniform stripe lasers with AR coatings,
(5) surface grating DFB non uniform stripe lasers without AR coatings,
(6) surface grating DFB non uniform stripe lasers with AR coatings.

(1) Narrow area oxide stripe lasers without AR coatings

To estimate the internal loss of the narrow area oxide stripe lasers and evaluate the threshold current, L-I curves were measured. Table 5.1 shows the threshold current and the external differential quantum efficiency for a single output facet in a laser which had the lowest threshold current among five lasers.

Table 5.1. Measurement results of narrow area oxide stripe lasers in pulsed operation, at 20 °C.

Lasers	Wavelength (nm)	Threshold Current (mA)	External differential quantum efficiency per facet (%)
Etched GaAs contact layer	861.0	30	8.3
Non etched GaAs contact layer	861.0	50	4.9

The measurement errors for threshold current and slope efficiency were estimated from six - fold repetition of measurements on the same device. The standard deviation of the threshold current was about 0.7 mA and the standard deviation of the external differential quantum efficiency was about 0.7 %. Nominal threshold current densities

were calculated to be 2000 A/cm^2 and 3300 A/cm^2 respectively. The differences in the threshold current and slope efficiency values were thought likely to be due to differences in the amount of current spreading outside the active region.

In broad area lasers, the current flow is one dimensional and the current density in the active region is the external current divided by the cross-sectional area. In structures such as a narrow area oxide stripe lasers, the current flow through the p-type layers is by a majority carrier drift current which spreads laterally as illustrated in Fig.5.4. Because of spreading, the current flows through an area in the active region that is significantly lager than the stripe contact area. Within the active layer, there is a lateral diffusive current of minority carriers due to recombination which also broadens the current distribution. These two effects greatly influence the threshold current behaviour and the emission properties of stripe geometry lasers.

A model for current spreading in stripe-geometry lasers has been presented in references 5-3 and 5-4. The simplified model assumes uniform current distribution in a region of width S, which is equal to the contact stripe width, and decreasing non-uniform current density outside the uniform current region. In Fig.5.4, the total current I_t is shown to be the sum of the uniform current under the stripe I_e and the spreading current I_o flowing in the $\pm y$ directions:

$$I_t = I_e + 2I_o \qquad [5.6]$$

In Ref. 5-4, it is shown that the current density across the junction at $y > |S/2|$ is

$$J_y(y) = \frac{I_o}{l_o L[1 + (|y| - \frac{S}{2}) / l_o]^2} \qquad [5.7]$$

where

$$l_o = \frac{2L}{\beta \rho_s I_o} \qquad [5.8]$$

In Eqn. [5.8], ß is the exponential junction parameter q/nkT, L is the cavity length, and ρ_S is the composite sheet resistivity given by

$$\frac{1}{\rho_s} = \frac{1}{\frac{\rho_4}{d_4}} + \frac{1}{\frac{\rho_3}{d_3}} \qquad [5.9]$$

It is also shown that

$$J_e = \frac{\beta \rho_s I_o^2}{2L^2} = \frac{I_o}{l_o L} \qquad [5.10]$$

and

$$I_o = \frac{[1 + (S\beta\rho_s / 2L)I_t]^{1/2} - 1}{S\beta\rho_s / 2L} \qquad [5.11]$$

Fig.5.5 shows the calculated results for the relationship between the sum of the uniform current in the active region and the total current in narrow oxide stripe lasers, using values for the cavity length of L = 600 μm, stripe width S = 2.5μm, GaAs sheet resistivity $\rho_4 = 8\times 10^{-3}$ Ω·cm and $Al_{0.4}Ga_{0.6}As$ sheet resistivity $\rho_3 = 2\times 10^{-1}$ Ω·cm. At threshold current, the ratio of the current flowing through the active region to the total current is calculated to be 36.0 % and 20.4 % in the laser with an etched GaAs

contact layer and the laser with an unetched GaAs contact layer, respectively. At threshold, the current flowing through the active region is calculated to be 10.2 ~ 10.8 mA and the threshold current density considering current spreading can be estimated as 680 ~ 720 A/cm^2.

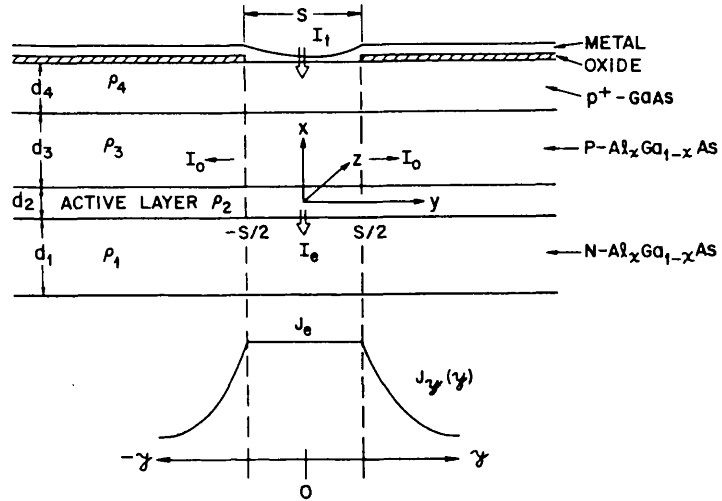

Fig.5.4. Schematic representation of current spreading in a contact stripe-geometry laser. The total current is I_t, the current through the active region under the stripe is I_e with a current density of J_e. The lateral spreading current is I_o, and the distribution of current density across the junction at y is $J_y(y)$ (Ref. 5-3).

The internal propagation loss α was calculated using the equations as follows:

$$\frac{1}{\eta_e} = \frac{1}{\eta_i} - L(\frac{\alpha}{\eta_i \ln R}) \quad [5.12]$$

$$\eta_e = 2 \times \frac{\Delta P}{\Delta I} \times \frac{1}{\gamma} \times \frac{q}{h\nu} \quad [5.13]$$

where η_i is the internal quantum efficiency, η_e is the external differential quantum efficiency considering current spreading, $\Delta P / \Delta I$ is the slope efficiency per facet and γ is the ratio of the current flowing through the active region to the total current. Using the values of the internal quantum efficiency, $\eta_i = 0.85$, from the evaluation of broad area oxide stripe lasers, the internal loss can be estimated at 16 ~ 17 cm^{-1}. This value is somewhat higher than the internal loss $\alpha_{broadoxide}$ of broad area oxide stripe lasers, $\alpha_{broadoxide} = 14.5$ cm^{-1}.

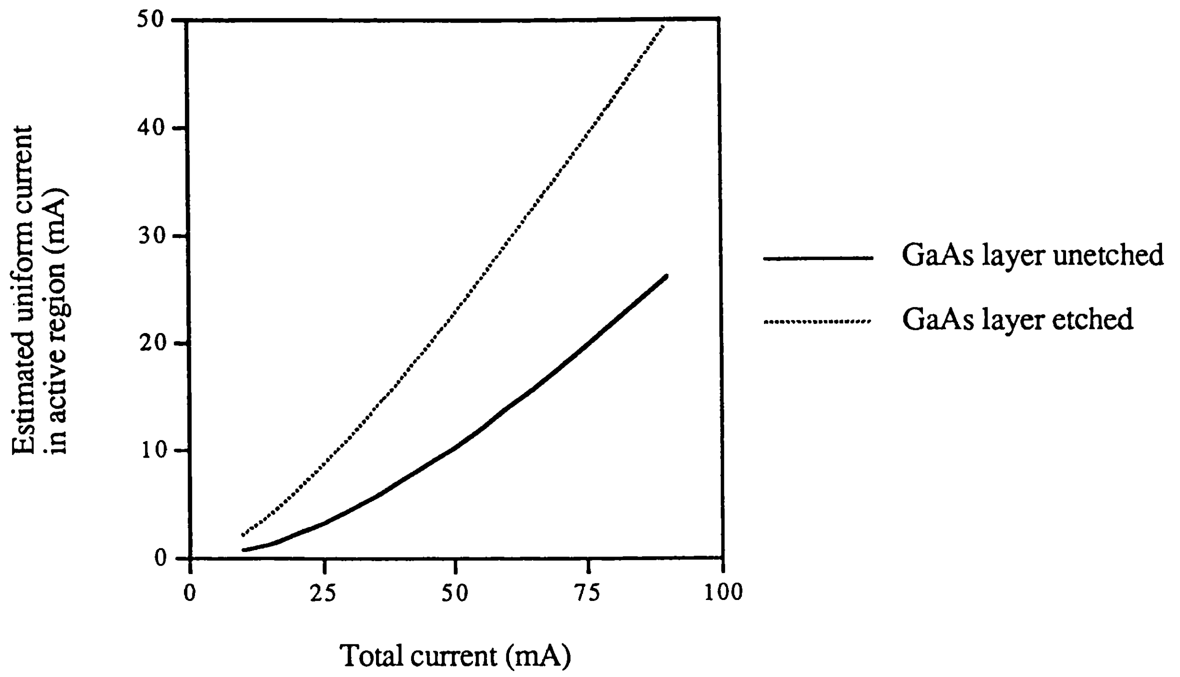

Fig.5.5. Calculated results for the relationship between the uniform current in the active region and the total current in narrow oxide stripe lasers.

(2) Narrow area oxide stripe lasers with AR coatings

To confirm the operation of AR coatings, spectra of narrow area oxide stripe lasers with AR coatings were measured. The emission spectra at 20 °C for the same device are shown in Fig.5.6 at I=350 mA and 450 mA. The threshold current increased from 50 mA without AR coatings to 350 mA with AR coatings, indicating that the AR coatings were close to optimum. The devices lased at a wavelength of 861.3 nm for I= 450 mA. Fig.5.7 shows the output spectra at 10, 20 and 40°C for I = 450 mA, confirming that the lasing wavelength shifted to longer wavelengths and that the gain curve peak value decreases in magnitude due to the rise in temperature.

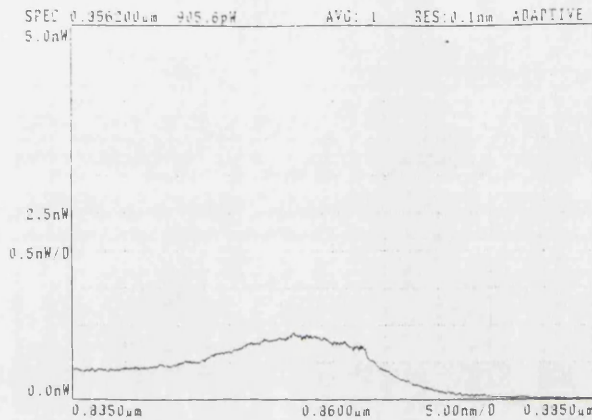

(A) I = 350 mA

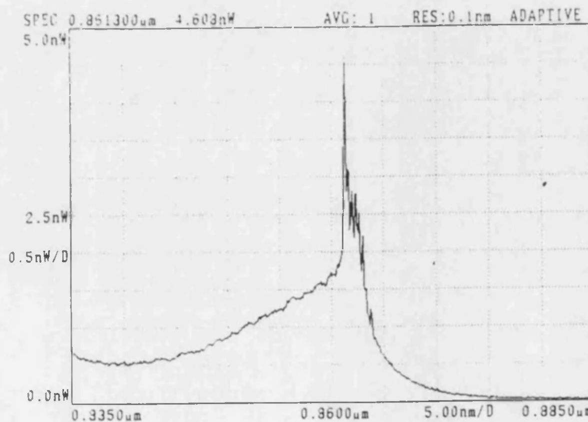

(B) I = 450 mA

Fig.5.6. Measured spectra for narrow oxide stripe lasers with AR coatings at 20 °C for I = 350 mA(A) and I = 450 mA(B) in pulsed operation.

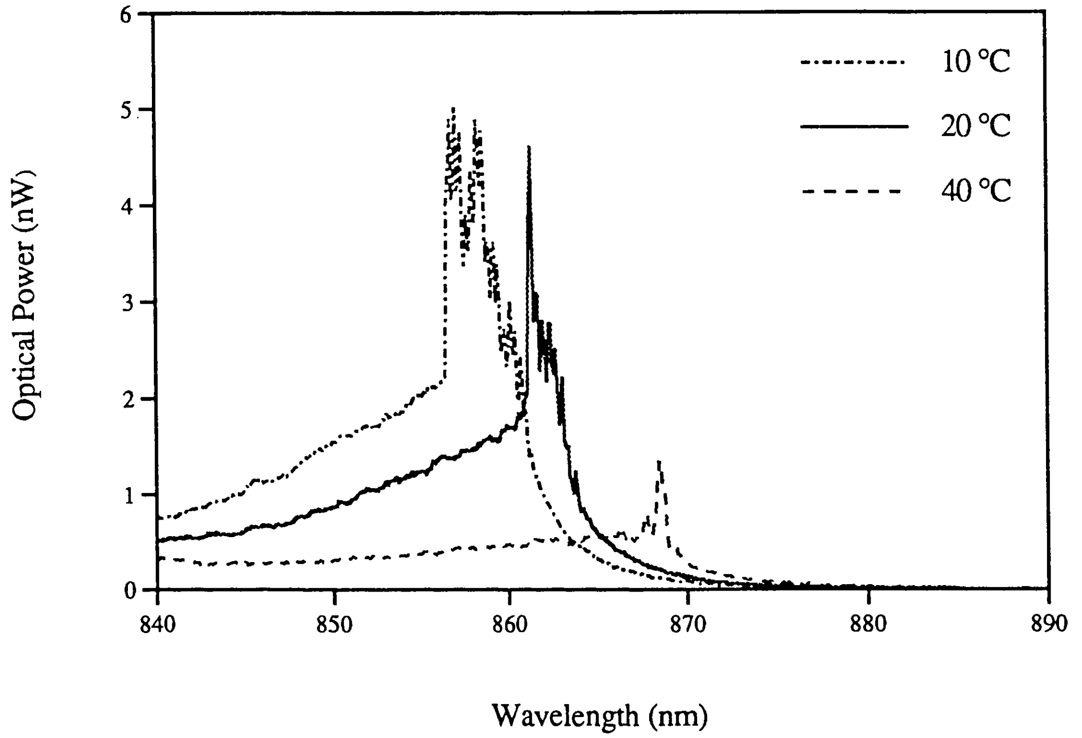

Fig.5.7. Measured spectra for narrow oxide stripe lasers with AR coatings at 10, 20 and 40 °C for I = 450 mA in pulsed operation.

(3) Surface grating DFB uniform stripe lasers without AR coatings

The L-I curves and spectra were also measured for surface grating DFB uniform stripe lasers without AR coatings, giving estimates for the internal losses of the lasers. Fig.5.8 shows the measured L-I curves of the lasers with an etched GaAs contact layer in the grating regions, and stripe width was 2.5 and 4.5 μm, without AR coatings, at 20 °C. These lasers had the lowest threshold currents among five lasers within each different category. Kinks exist at about 60 mA in the L-I curves.

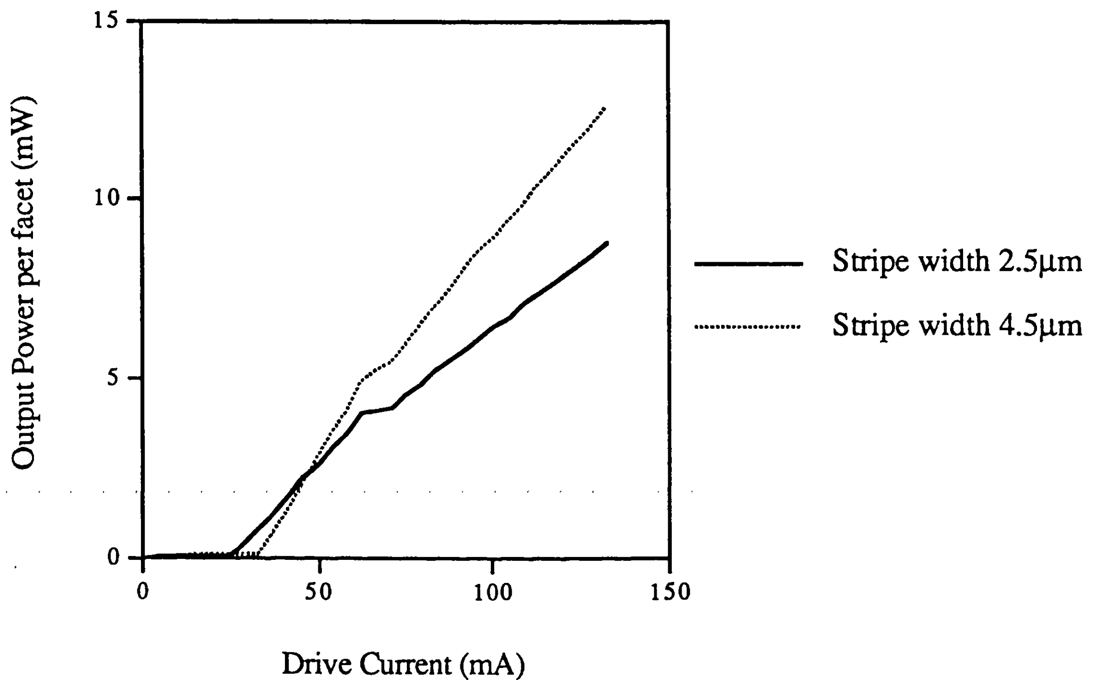

Fig.5.8. Measured output power per facet - drive current characteristics in surface grating DFB uniform stripe lasers without AR coatings, at 20 °C.

To investigate the reason for these kinks, spectra for drive currents around 60 mA were measured. Fig.5.9 shows changes in the spectra of the 4.5 μm stripe laser at 20 and 40 °C for 50, 60 and 70 mA current levels respectively.

At 20 °C

At 40 °C

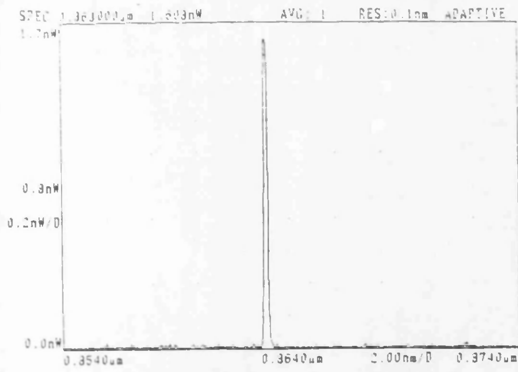

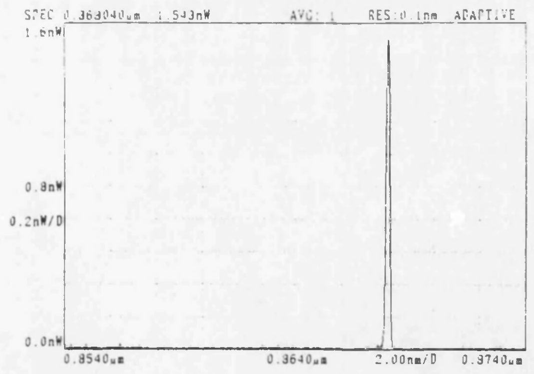

I = 50 mA

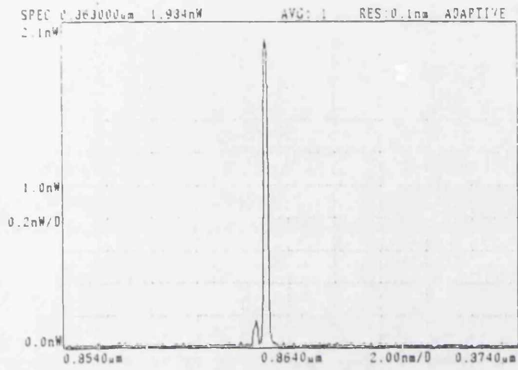

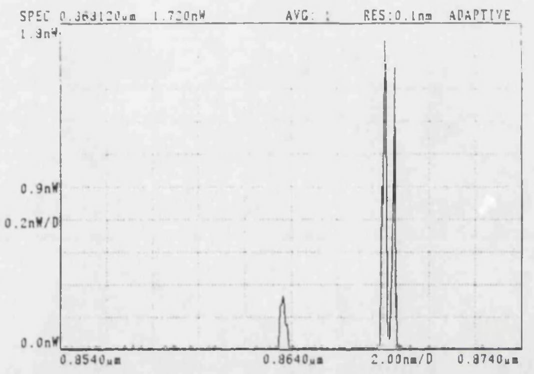

I = 60 mA

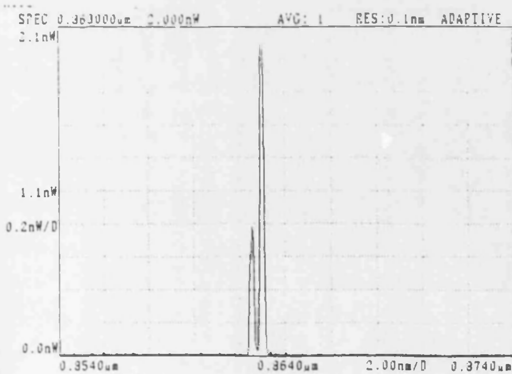

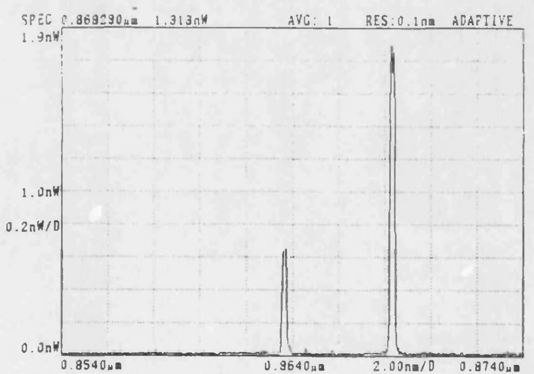

I = 70 mA

Fig.5.9. Measured spectra for 4.5 μm width stripe laser without AR coatings in pulsed operation at 20 and 40 °C for 50, 60 and 70 mA.

For I = 50 mA, below the kink current level, the temperature dependence of wavelength was about 0.25 nm/°C. From this temperature dependence of wavelength, it was clear that the laser was operating in a Fabry-Perot (FP) mode.[5-5] The measured wavelength of the FP mode was 863.0 nm at 20 °C.
For I = 60 mA, near the kink, additional small peaks were observed at 20 and 40 °C. The temperature dependence of wavelength for these peaks was about 0.06 nm/°C and they were therefore considered to be DFB modes. [5-5] The wavelength of the DFB mode was 862.6 nm at 20 °C.
For I = 70 mA, above the kink, the ratio of the DFB mode optical power to the FP mode optical power increased and this behaviour was also found in 2.5 μm stripe width lasers.
These results confirmed that the FP mode, only, lases below the kink, while FP modes and DFB modes lase above that kink.

The internal loss of the surface grating stripe waveguide can be estimated using the L-I curve data, below the kink. Table 5.2 shows the threshold current and the external differential quantum efficiency for FP mode taken from the L-I curve below the kink.

Table 5.2. Measurement results for FP modes in surface grating uniform stripe lasers without AR coatings in pulsed operation, at 20 °C.

Lasers	Threshold Current (mA)	External differential quantum efficiency per facet (%)
Stripe width 2.5 μm	26	7.6
Stripe width 4.5 μm	34	12

Nominal threshold current densities for FP modes were calculated to be 1700 A/cm^2 in the 2.5 μm width stripe laser and 1300 A/cm^2 in the 4.5 μm width stripe laser.
It is necessary to calculate the ratio of the current flowing through the active region to the total current for estimation of the internal loss. The surface grating stripe waveguide consists of ridge waveguide sections and slab waveguide sections alternately. The current flowing through the active region can be calculated as an average value between the current in the ridge waveguide structure and the current in the slab waveguide structure, on the assumption that the grating mark-space ratio is 1:1. Fig. 5.12 shows the calculated relationship between the sum of the uniform current in the active region and the total current for surface grating uniform stripe lasers, using the values: cavity length L = 600 μm, stripe widths S = 2.5 μm and

4.5μm, GaAs sheet resistivity $\rho_4 = 8 \times 10^{-3}\ \Omega\cdot$cm and $Al_{0.4}Ga_{0.6}As$ sheet resistivity $\rho_3 = 2 \times 10^{-1}\ \Omega\cdot$cm. The ratio of the current flowing through the active region to the total current was calculated to be 46.2 % and 57.9 % in the 2.5 μm stripe width laser and the 4.5 μm stripe width laser, respectively. In Eqns. [5.12] and [5.13], using the value of the internal quantum efficiency, $\eta_i = 0.85$, from the evaluation of broad area oxide stripe lasers, the internal loss can be estimated at 32 cm^{-1} in the 2.5 μm stripe width laser and 22 cm^{-1} in the 4.5 μm stripe laser. These values are clearly bigger than the values for narrow area oxide stripe lasers ($\alpha_{narrow\ oxide}$ = 16~17 cm^{-1}), most probably because the scattering losses were increased by the surface gratings.
Finally, at threshold current, the current flowing through the active region was calculated to be 12.0 mA in the 2.5 μm stripe width laser and 19.7 mA in the 4.5 μm stripe width laser, respectively. So the FP mode threshold current density considering current spreading can be estimated at 800 A/cm^2 in the 2.5 μm stripe width laser and 730 A/cm^2 in the 4.5 μm stripe width laser.

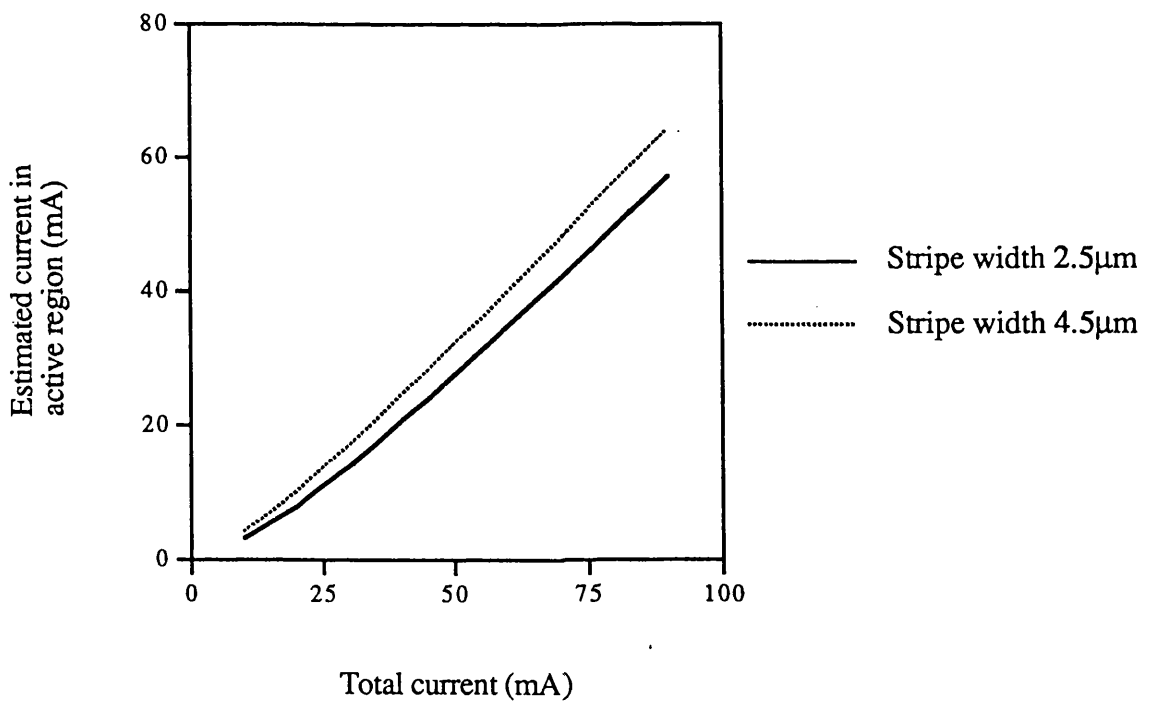

Fig.5.10. Calculated results for the relationship between current in active region and the total current in surface grating DFB stripe lasers.

(4) Surface grating DFB uniform stripe lasers with AR coatings

To confirm the effect of etching the GaAs contact layer in the grating region, I-V curves and L-I curves were measured for the lasers, as follows:

(a) stripe width 2.5 μm and GaAs contact layer unetched away,
(b) stripe width 2.5 μm and GaAs contact layer etched away,
(c) stripe width 4.5 μm and GaAs contact layer unetched away,
(d) stripe width 4.5 μm and GaAs contact layer etched away.

The measured I-V curves in pulsed operation are shown in Fig.5.11. The data presented for each type of laser is for the particular one which has the lowest threshold current among five lasers. Similar I-V characteristics result, despite the differences in the lasers. The turn on voltage was about 1.5 V and the differential resistance in the region from I = 30 mA to I = 100 mA was about 2 Ω.

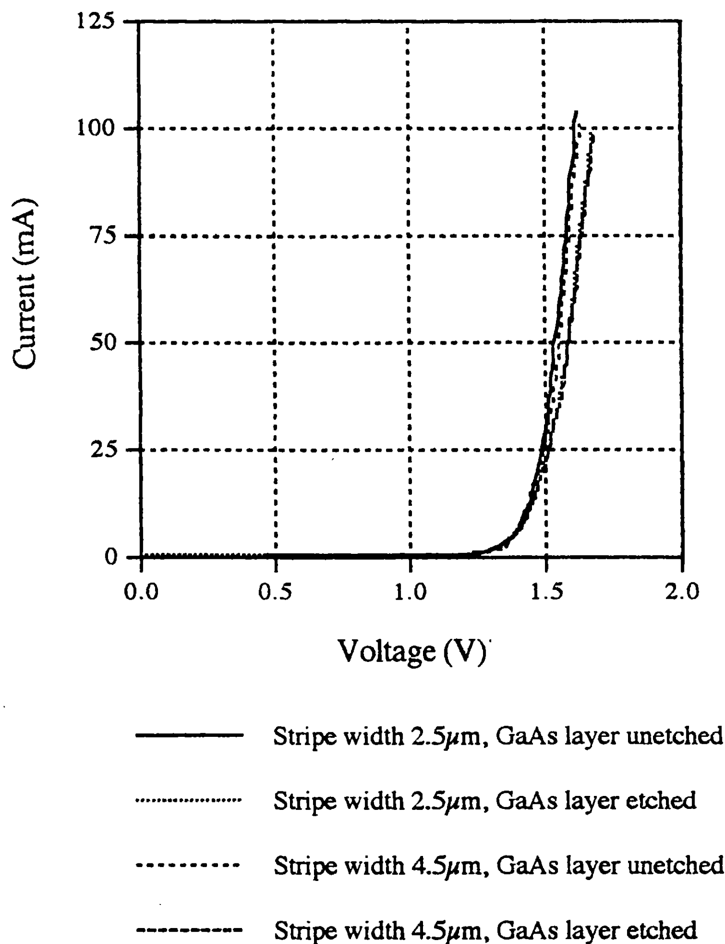

Fig.5.11. Measured current - voltage characteristics of surface grating DFB uniform stripe lasers with AR coatings.

Fig. 5.12 shows measured L-I curves for pulsed operation. Table 5.3 shows the external differential quantum efficiency, the threshold current and the threshold current density obtained from the L-I curves.

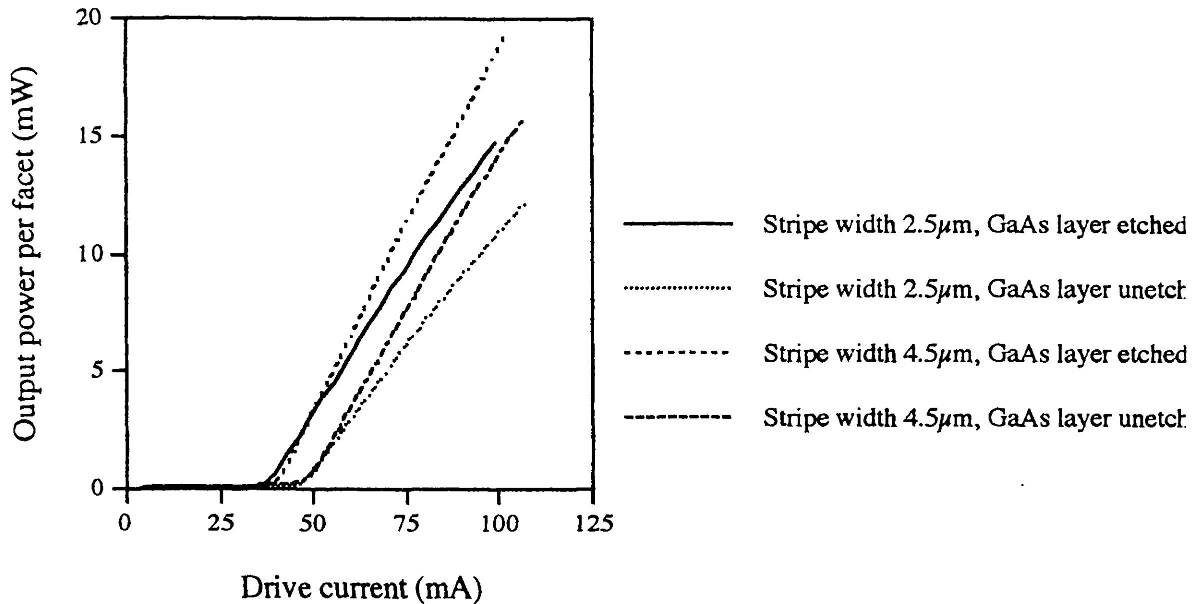

Fig.5.12. Measured output power per facet - drive current characteristics in surface grating DFB uniform stripe lasers with AR coatings.

Table 5.3. Measured data for surface grating DFB uniform stripe lasers with AR coatings in pulsed operation.

Lasers	External differential quantum efficiency per facet (%)	Threshold current (mA)	Nominal threshold current density (A/cm^2)
Stripe width 2.5μm GaAs contact layer etched.	15	36	2400
Stripe width 2.5μm GaAs contact layer non etched.	13	45	3000
Stripe width 4.5μm GaAs contact layer etched.	20	39	1440
Stripe width 4.5μm GaAs contact layer non etched.	17	47	1740

It was confirmed that the L-I curves of AR coated devices were kink-free up to 100 mA. Similar kink-free behaviour was shown by Miller et al[5-6] in InGaAs-GaAs-AlGaAs strained-layer DFB stripe lasers. The threshold current for 2.5 μm width stripe lasers with etched GaAs contact layers was about 20 % lower than for lasers with unetched GaAs contact layers and the threshold current for 4.5 μm width stripe lasers with etched GaAs contact layers was about 17 % lower than for lasers with unetched GaAs contact layers. These results agreed with calculated results using the model which is shown in section 5.2.1.(3). The ratio of the current flowing through the active region to the total current was calculated to be 49.6 % and 59.0 % respectively in the 2.5 μm width and the 4.5 μm width stripe lasers with etched GaAs contact layer. So the DFB laser threshold current densities, taking account of current spreading, can be estimated at 1190 A/cm^2 and 850 A/cm^2 in the 2.5 μm width and 4.5μm width stripe lasers, respectively.

Fig.5.13 shows measured spectra for lasers with etched GaAs contact layers at I=60 mA (1.5~1.7$\times I_{th}$) and I = 100 mA (2.6~2.8$\times I_{th}$), at 20 °C. There is no evidence of Fabry-Perot modes or higher order transverse modes. The emission wavelengths were 862.6 nm and 862.8 nm in the 2.5 μm width stripe laser and the 4.5 μm width stripe laser respectively. No measurable changes in the emission wavelengths were observed when the drive current was increased to 100 mA (2.6~2.8$\times I_{th}$) in pulsed operation.

To confirm that only a single transverse mode was lasing and to estimate the lasing area, far-field intensity patterns were measured. Fig.5.14 shows measurements of pulsed far-field intensity patterns for the 2.5 μm width stripe lasers with etched GaAs contact layer and Fig.5.15 shows measurements of pulsed far-field intensity patterns for the 2.5 μm width stripe lasers with etched GaAs contact layers, at 20 °C.

For the 2.5 μm width stripe lasers, the full angle at half power perpendicular to the active layer was about 46 degrees and the full angle at half power parallel to the active layer was about 18 degrees. For the 4.5 μm width stripe lasers, the full angle at half power perpendicular to the active layer was about 46 degrees and the full angle at half power parallel to the active layer was about 10 degrees. The approximate width of the lasing area parallel to the active layer was calculated by the equation as follows:

$$W = \frac{\lambda}{\Delta\theta_{//,3dB}} \quad [5.14]$$

where W is the approximate width of lasing area, λ is lasing wavelength and $\Delta\theta_{//,3dB}$ is the full angle(radian) at half power of the far-field pattern. Using Eqn. [5.14], the approximate width of the lasing area was calculated to be 2.7 μm and 4.9 μm for the 2.5 μm width stripe laser and the 4.5 μm width stripe laser respectively.

From measurements of the L-I curves, the emission spectra and the far-field patterns, it was confirmed that only the fundamental transverse DFB mode lases up to 100 mA ($2.6\sim2.8\times I_{th}$) in the 2.5 μm width and 4.5 μm width stripe lasers with AR coatings.

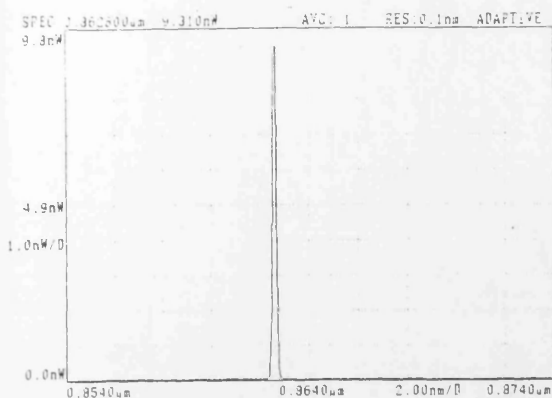

I = 60 mA (Neutral density filter 0.3)

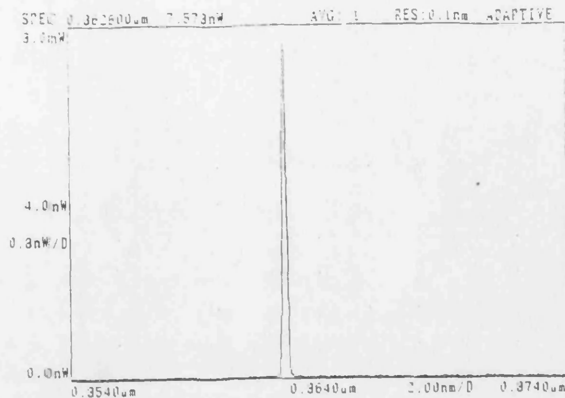

I = 100 mA (ND 0.044)

(A) 2.5 μm width stripe lasers with etched GaAs contact layer.

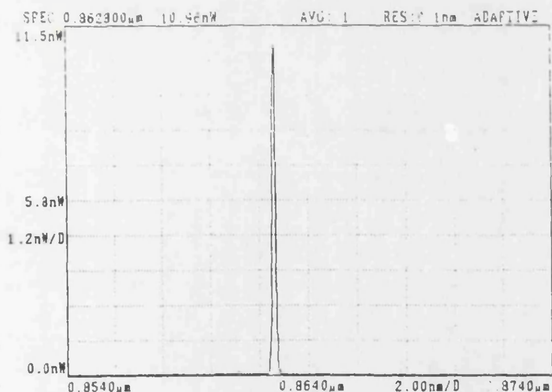

I = 60 mA (ND 0.3)

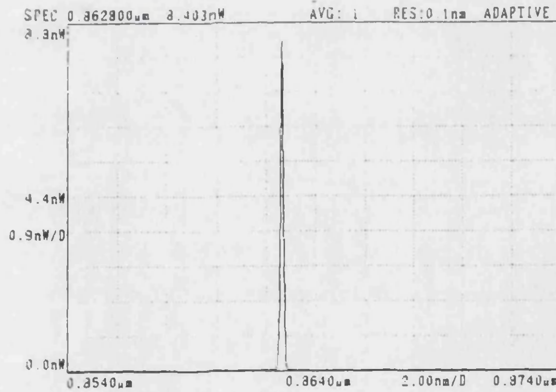

I = 100 mA (ND 0.044)

(B) 4.5 μm width stripe lasers with etched GaAs contact layer.

Fig.5.13. Measured spectra for the 2.5 μm width (A) and the 4.5 μm width (B) stripe lasers in pulsed operation, at 20 °C.

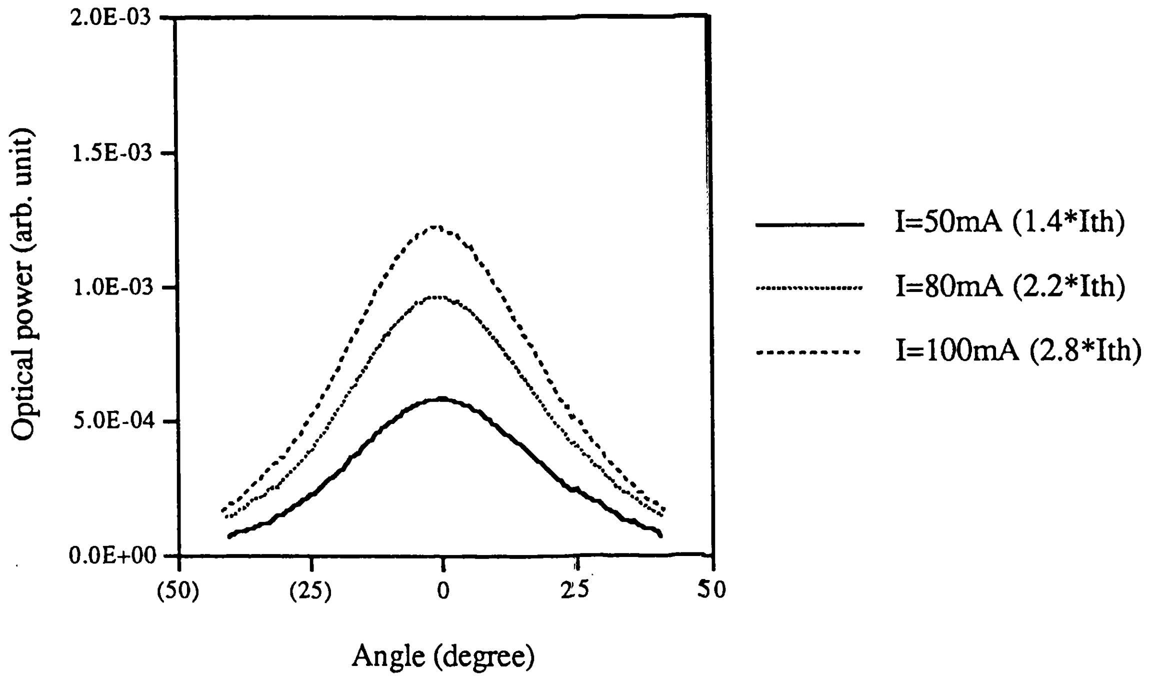

(A) Far-field intensity patterns for the 2.5μm width stripe laser in perpendicular to the active layer.

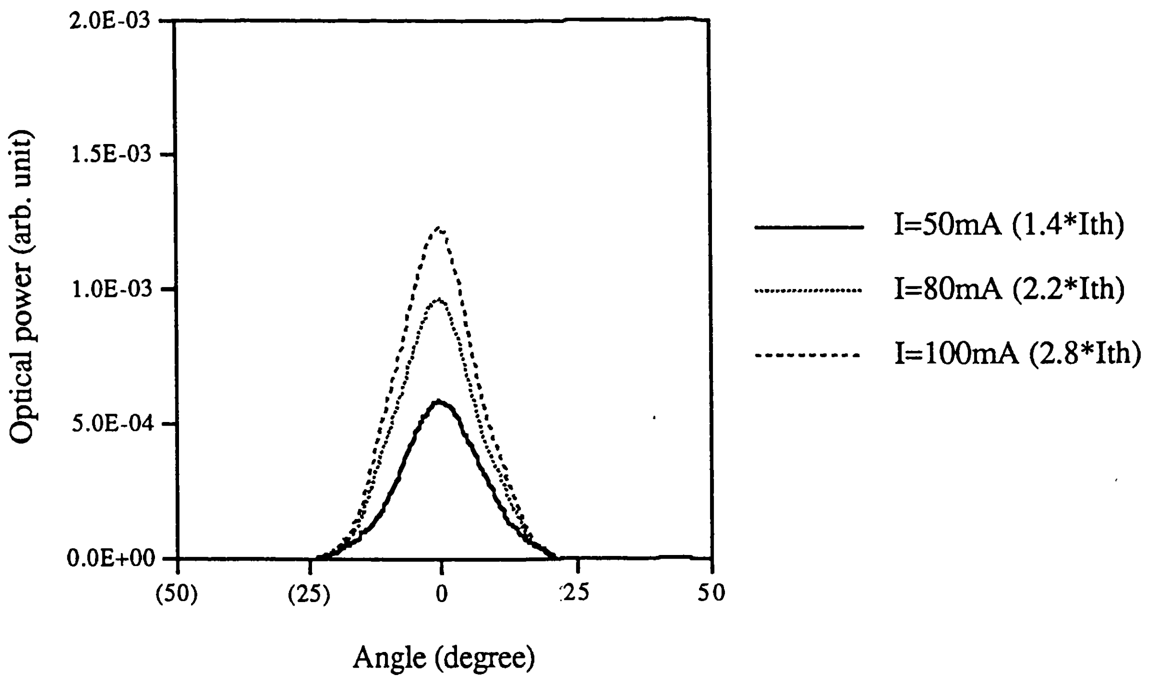

(B) Far-field intensity patterns for the 2.5 μm width stripe laser in parallel to the active layer.

Fig.5.14. Measured far-field intensity patterns for 2.5 μm width stripe laser in pulsed operation, at 20 °C.

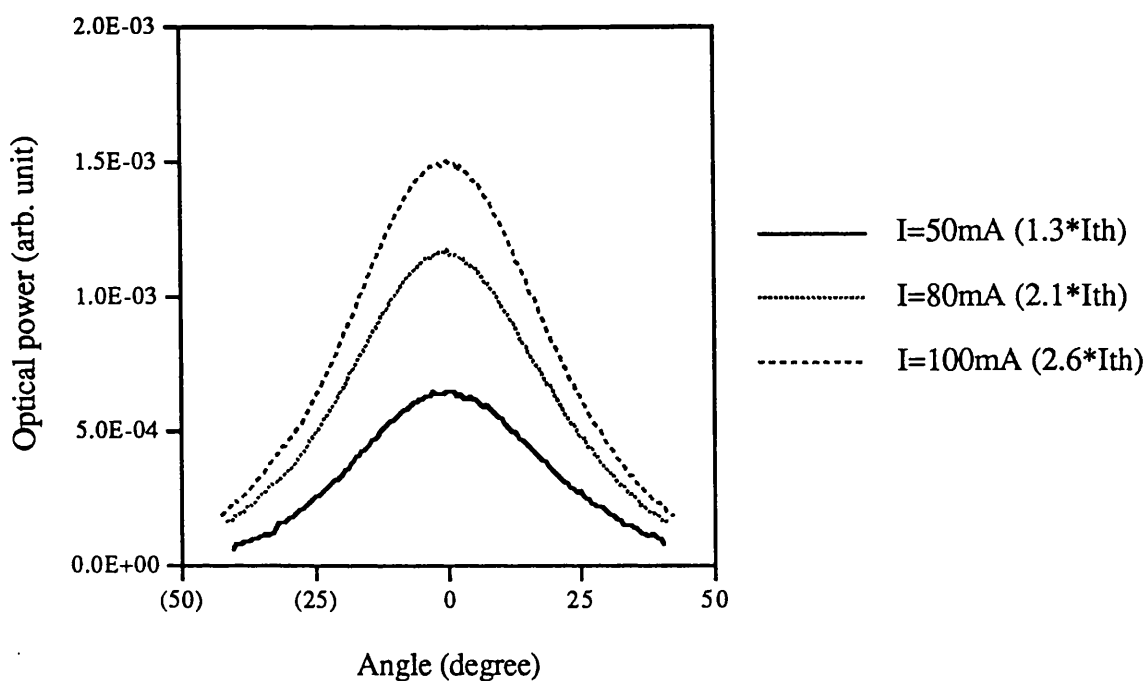

(A) Far-field intensity patterns for the 4.5m width stripe laser in perpendicular to the active layer.

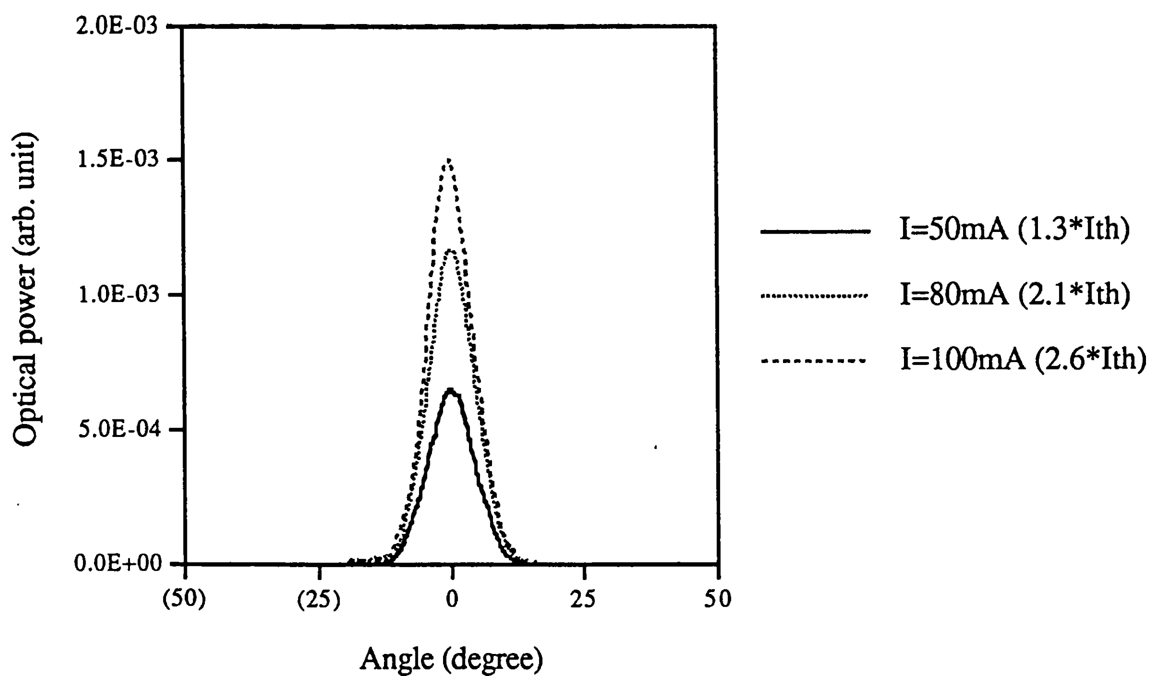

(B) Far-field intensity patterns for the 4.5μm width stripe laser in parallel to the active layer.

Fig.5.15. Measured far-field intensity patterns for 4.5 μm width stripe laser in pulsed operation, at 20 °C.

Because of the single transverse mode operation of the lasers, the coupling constant κ could be estimated using measured values of the slope efficiency, the internal loss, and estimates of the ratio of the current flowing through the active region to the total current.

The threshold gain g_{th} which is related to optical power and includes the gain necessary to counteract optical loss is given as follows[5-7, 5-8, 5-9] :

$$\eta_e = \eta_i(1-\frac{\alpha}{g_{th}}) \quad [5.15]$$

$$\eta_e = 2\times\frac{\Delta P}{\Delta I}\times\frac{1}{\gamma}\times\frac{q}{h\nu} \quad [5.16]$$

where η_e is the external differential quantum efficiency including current spreading effects, η_i is the internal quantum efficiency, γ is the ratio of the current flowing through the active region to the total current and α is the internal loss. The threshold gain is related to the net amplitude gain g_a in the present instance by

$$g_{th} = 2g_a + \alpha \quad [5.17]$$

So the threshold gain g_{th} and the amplitude gain g_a are calculated using values in Table 5.4.

Table 5.4. Data used in calculations of the threshold gain g_{th}.

Lasers	$\Delta P/\Delta I$ (W/A)	γ (%)	α (cm^{-1})	η_i (-)
Stripe width 2.5μm	0.22	49.6	32	0.85
Stripe width 4.5μm	0.29	59.0	22	0.85

$\Delta P/\Delta I$ values are from Table 5.3, γ values are calculated in section 5.2.1.(4) and η_i is calculated from measured results for broad area oxide stripe lasers. α values are calculated in section 5.2.1.(3) and are based on FP mode operation. They are adopted, in, the calculation here, because the wavelength of the DFB mode is close to the wavelength of the FP modes.

The threshold gains for the 2.5 μm width and 4.5 μm width stripe lasers were calculated to be $g_{th,2.5}$= 116 cm^{-1} and $g_{th,4.5}$= 111cm^{-1} respectively. The amplitude gain g_a values for the 2.5 μm width and 4.5 μm width stripe lasers were calculated to be $g_{a,2.5}$=42 cm^{-1} and $g_{a,4.5}$=45 cm^{-1} respectively.

To calculate the coupling constant, a relationship between the amplitude gain and the coupling constant is required and was calculated as a threshold condition for DFB lasers[5-10, 5-11]. The threshold condition is given by

$$(g_a - i\Delta\beta)\sinh(SL) = S\cosh(SL) \quad [5.18]$$

$$S = \sqrt{\kappa^2 + (g_a - i\Delta\beta)^2} \quad [5.19]$$

where κ is coupling constant, g_a is the amplitude gain required for threshold, $\Delta\beta$ is the frequency deviation from the Bragg condition for an index periodicity and L is cavity length. Using Eqns. [5.18] and [5.19], the relationship between the coupling constant and the amplitude gain may be calculated. Fig.5.16 shows the result of the calculation.

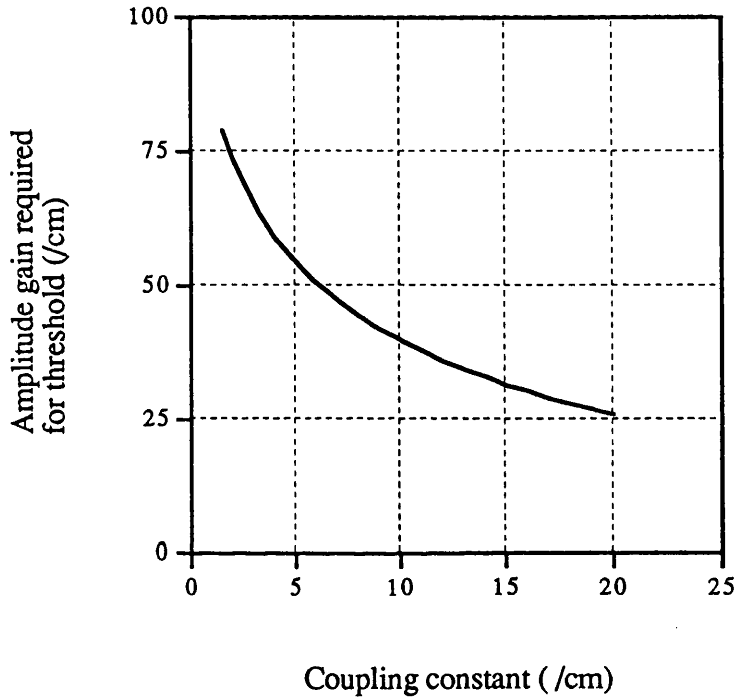

Fig.5.16. The calculated relationship between the coupling constant and the amplitude gain required for threshold in DFB lasers using Eqns. [5.18] and [5.19]. L=600 μm is assumed.

From the relationship between the coupling constant and the amplitude gain required for threshold in DFB lasers, the coupling constants κ for the 2.5 μm width and 4.5 μm width stripe lasers are estimated to be $\kappa_{2.5}$ = 9 cm^{-1} and $\kappa_{4.5}$ = 8 cm^{-1}. This estimation is not accurate because a simple model for calculation of current spreading and a simple threshold condition for DFB lasers are used. For accurate estimation of the coupling constant, it is necessary to measure the stopband width, which is descried in a later section.

Fig.5.17 shows the temperature dependence of the spectrum of the 2.5 μm width stripe DFB lasers and Fig.5.18 shows the spectra of the lasers for I = 60 mA at 2, 5, 10 and 60 °C in pulsed operation. The estimated temperature dependence of the DFB lasing mode was 0.063 nm/°C. It was found that the temperature range for single transverse DFB mode operation was from 10 to 60 °C and that the DFB mode did not lase at 2 °C. There was evidence of another mode below 5 °C, which was likely to be the Fabry-Perot mode from its temperature dependence. The reason for the onset of FP mode lasing below 5 °C is likely to be that the threshold gain for the FP mode becomes lower than the threshold gain for the DFB mode, because of the shift of the gain curve to shorter wavelengths, as shown in Fig.5.7.

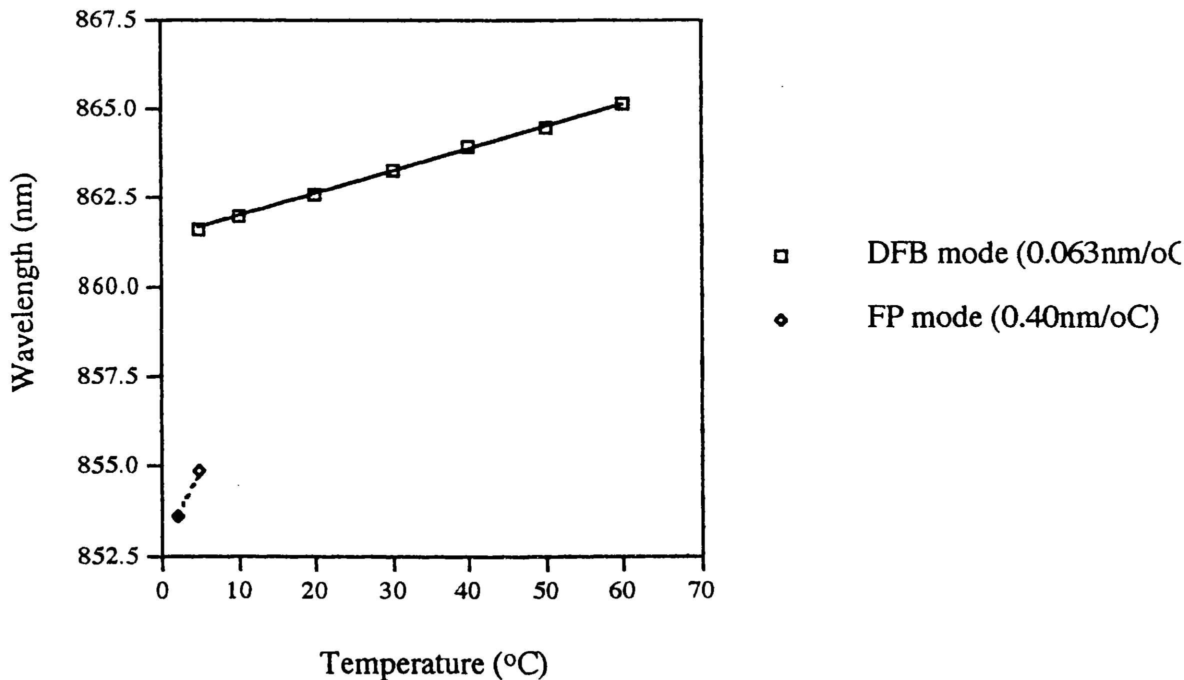

Fig.5.17. Temperature dependence of the spectrum of 2.5 μm width stripe DFB lasers.

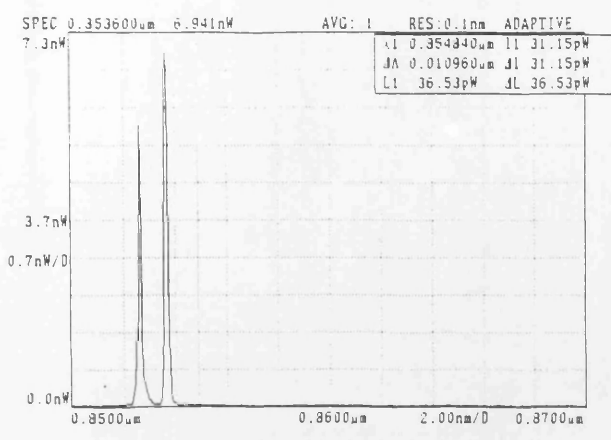

At 2 °C

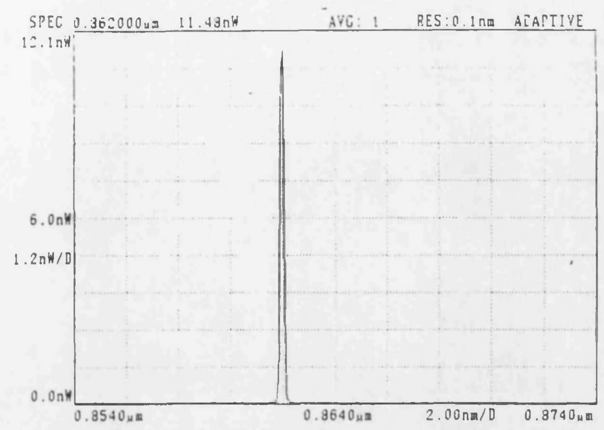

At 10 °C

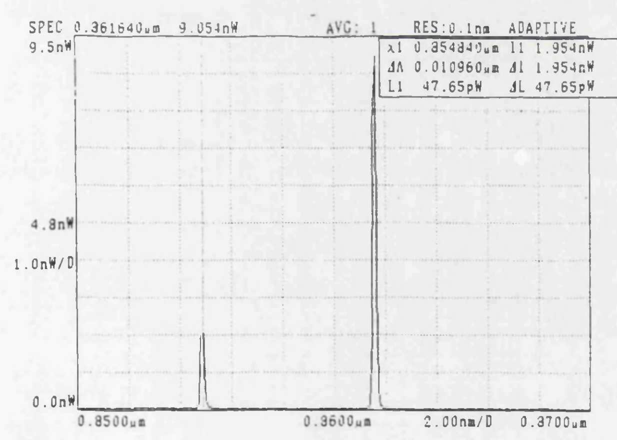

At 5 °C

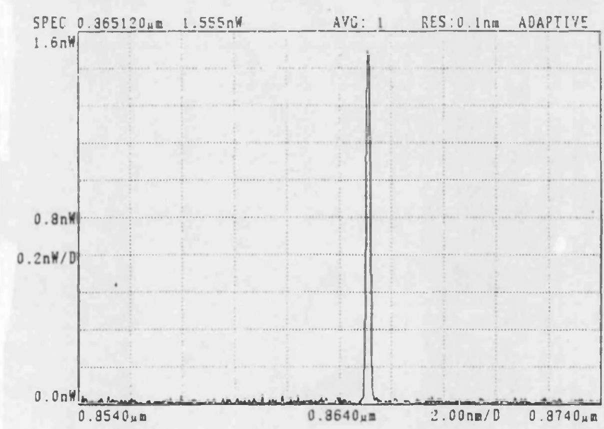

At 60 °C

Fig.5.18. Change of spectrum of the 2.5 µm width stripe DFB lasers for I = 60 mA, at 2, 5, 10 and 60 °C in pulsed operation.

(5) Surface grating DFB non-uniform stripe lasers without AR coatings

Surface grating DFB non-uniform stripe lasers had a wider region which was located at the centre of the lasers. The width of the wider region was 4.5 μm and the width of the narrower region was 2.5 μm. The lengths of the wider regions were 60 μm (10%), 180 μm (30 %), 300 μm (50 %) and 420 μm (70 %). The L-I curves and spectra were measured for surface grating DFB non uniform stripe lasers without AR coatings. Fig.5.19 shows the measured L-I curves of the lasers with etched GaAs contact layers in the grating regions, and where the length of the wider region was 60 μm (10 %) and 300 μm (50 %), without AR coatings, at 20 °C. These lasers had the lowest threshold currents among the five different categories. Kinks exist at about 70 mA in the L-I curves.

To investigate the reason for the kinks, spectra for drive currents around 70 mA were measured. Fig.5.20 shows changes in the spectra of the laser whose length of wider region is 300 μm at 20 and 40 °C for 60, 70, 80 mA the current levels respectively.

For I = 60 mA in the kink, temperature dependence of wavelength was about 0.20 nm/°C. From this temperature dependence of wavelength, it was clear that the laser was operating in a Fabry-Perot (FP) mode.[5-5] The measured wavelength of the FP mode was 862.8 nm at 20 °C.

For I =70 mA near the kink, additional small peaks were observed at 20 and 40 °C. The temperature dependence of wavelength for these peaks was about 0.07 nm/°C and they were therefore considered to be DFB modes. [5-5] The wavelength of the DFB mode was 862.0 nm at 20 °C.

For I = 80 mA above the kink, the ratio of the DFB mode optical power to the FP mode optical power increased and this behaviour was also found in another length of wider region lasers.

From these results, it is confirmed that the FP mode, only, lases below the kink and the FP mode and DFB mode lase above the kink.

The internal loss of the surface grating non-uniform stripe waveguide might possibly be estimated using the L-I curve data, below the kink. It is necessary to calculate the ratio of the current flowing through the active region to the total current for estimation of the internal loss, as is proposed for the surface grating uniform lasers. But the calculation is complicated because of the structure. Accordingly, the calculation was not attempted and the estimation of the internal loss was not carried out.

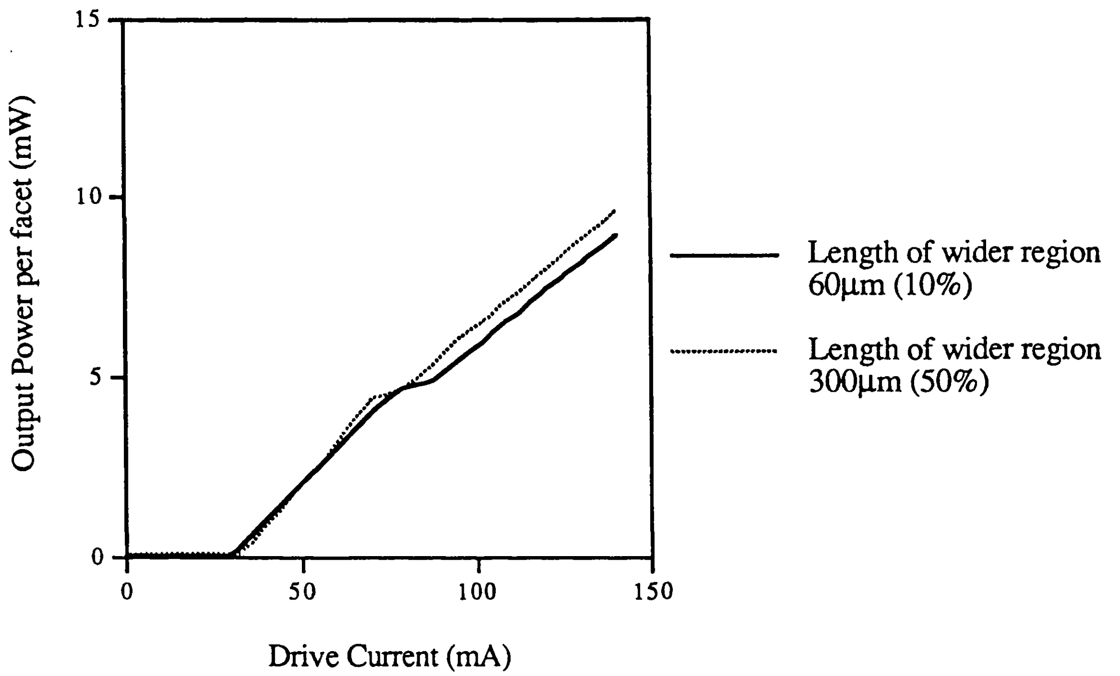

Fig.5.19. Measured output power per facet - drive current characteristics in surface grating DFB non-uniform stripe lasers without AR coatings, at 20 °C.

At 20 °C

At 40 °C

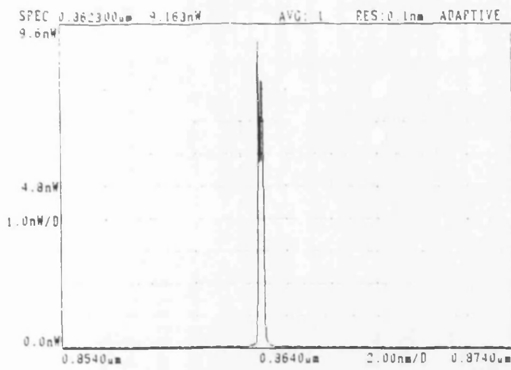

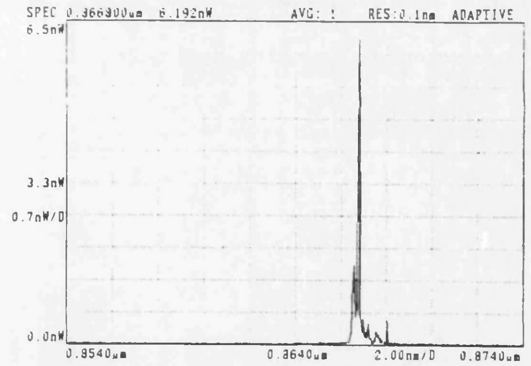

I = 60 mA

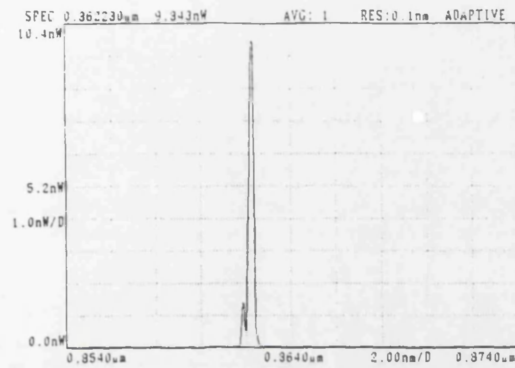

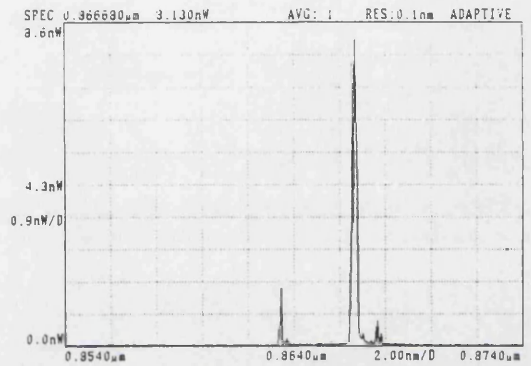

I = 70 mA

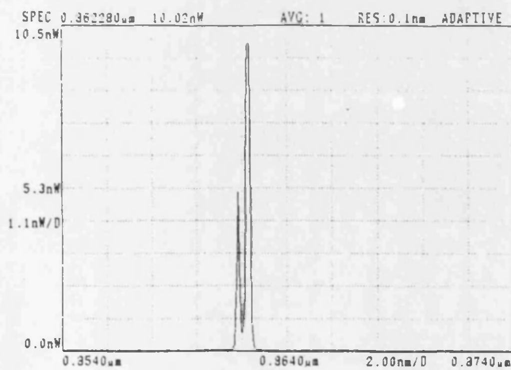

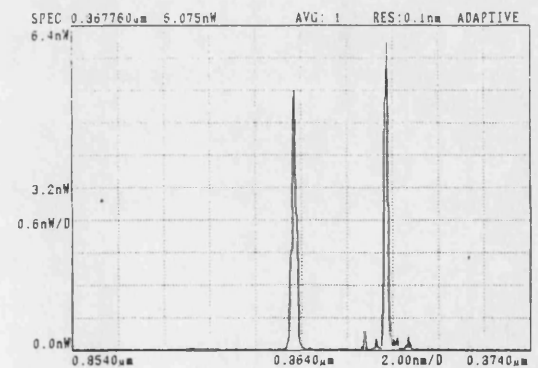

I = 80 mA

Fig.5.20. Measured spectra for the laser whose length of wider region is 300 μm without AR coatings in pulsed operation at 20 and 40 °C for 60, 70 and 80mA.

(6) Surface grating DFB non-uniform stripe lasers with AR coatings

From measured I-V curves for the surface grating DFB non-uniform stripe lasers in pulsed operation, the turn on voltage was about 1.5 V and the differential resistance in the region from I = 30 mA to I = 100 mA was about 2Ω. Fig.5.21 shows measured L-I curves for pulsed operation at 20 °C. Table 5.5 shows the external differential quantum efficiency, the threshold current and the threshold current density obtained from L-I curves.

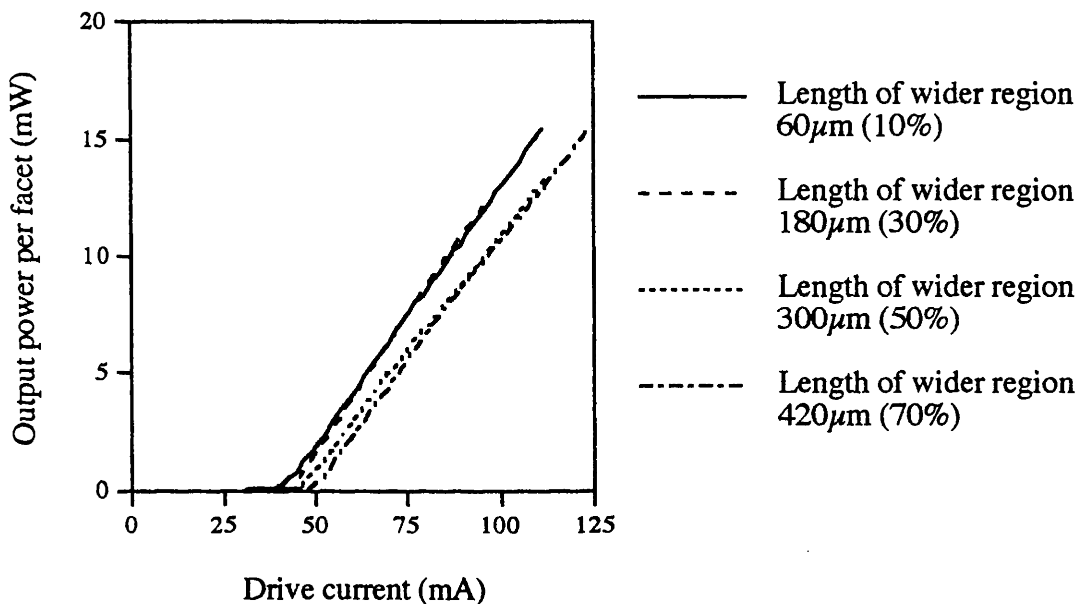

Fig.5.21. Measured output power per facet - drive current characteristics in surface grating DFB non-uniform stripe lasers with AR coatings in pulsed operation, at 20 °C.

Table 5.5. Measured data for surface grating DFB non uniform stripe lasers with AR coatings in pulsed operation, at 20 °C.

Lasers	External differential quantum efficiency per facet (%)	Threshold current (mA)	Nominal threshold current density (A/cm^2)
Length of wider region 60 μm	15	41	2530
Length of wider region 180 μm	16	42	2260
Length of wider region 300 μm	14	45	2140
Length of wider region 420 μm	14	48	2050

It was confirmed that the L-I curves of AR coated devices were kink-free up to 110 mA and the threshold current was higher than the threshold current of uniform stripe lasers, which may be due to an increase in the total optical internal loss caused by the boundaries between the wider and the narrower regions. Fig. 5.22 shows measured spectra for the 180 μm (30 %) non-uniform region lasers and the 300 μm (50 %) non-uniform region lasers. There is no evidence of Fabry-Perot modes or higher order transverse modes. The emission wavelengths were 862.6 nm. No measurable changes in the emission wavelengths were observed when the drive current was increased to 100 mA (2.2~2.4× I_{th}) in pulsed operation.

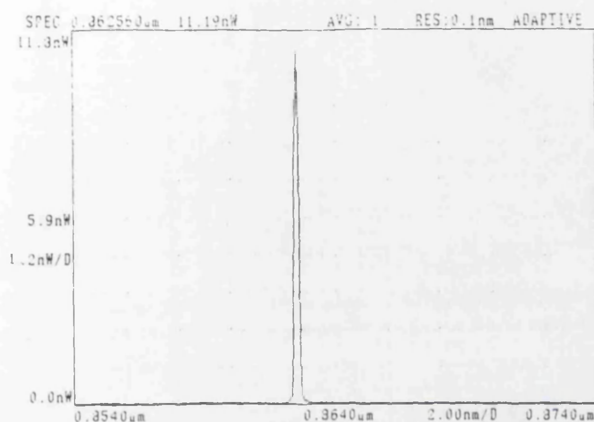

I = 60 mA (ND 0.3)

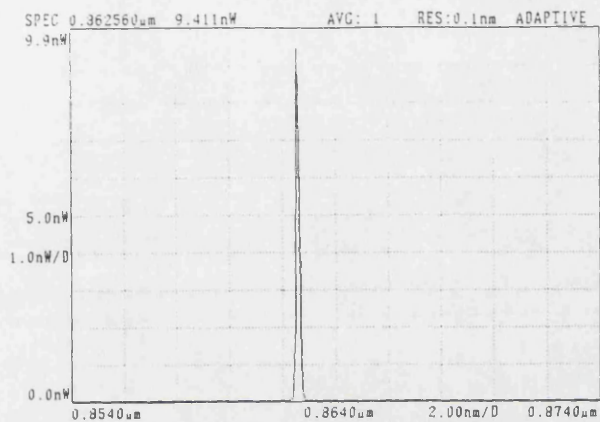

I = 100 mA (ND 0.044)

(A) 180 μm (30 %) non-uniform region lasers.

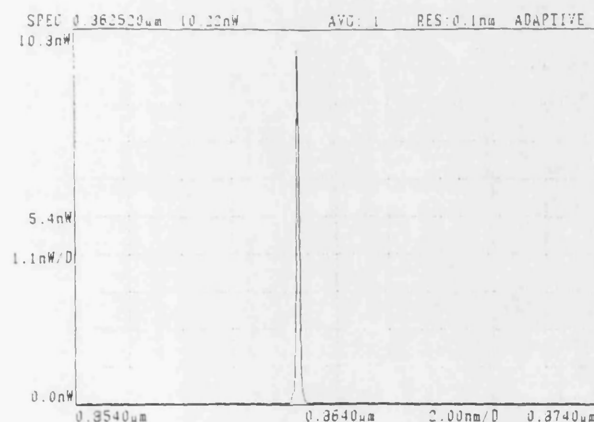

I = 60 mA (ND 0.3)

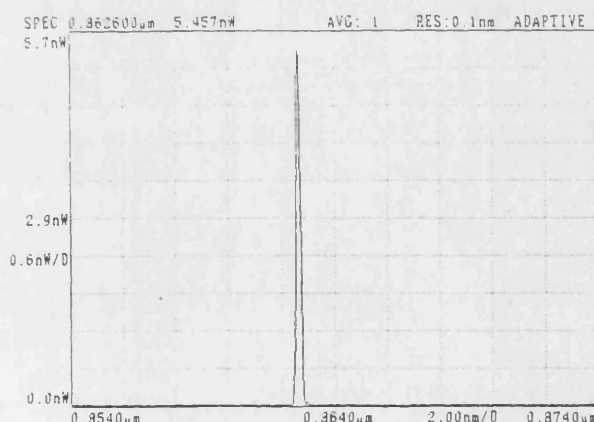

I = 100 mA (ND 0.044)

(B) 300 μm (50 %) non-uniform region lasers.

Fig.5.22. Measured spectra for the 180 μm (30 %) non uniform region (A) and the 300 μm (50 %) non uniform region (B) lasers in pulsed operation, at 20 °C.

Fig.5.23 shows the temperature dependence of the spectrum of the 180 μm (30 %) non-uniform region DFB lasers and Fig.5.24 shows the spectra of the lasers for I=60mA at 2, 5, 10 and 60 °C in pulsed operation. The estimated temperature dependence of the DFB lasing mode was 0.062 nm/°C. It was found that the temperature range for single transversal DFB mode operation was from 10 to 60 °C and that the DFB mode did not lase at 2 °C. There was evidence of another mode below 5 °C, which was likely to be that the Fabry-Perot mode from its temperature dependence. The reason for the onset of FP mode lasing below 5 °C is likely to be the threshold gain for the FP mode becomes lower than the threshold gain for the DFB mode, because of the shift of the gain curve to shorter wavelengths, as shown in Fig.5.7.

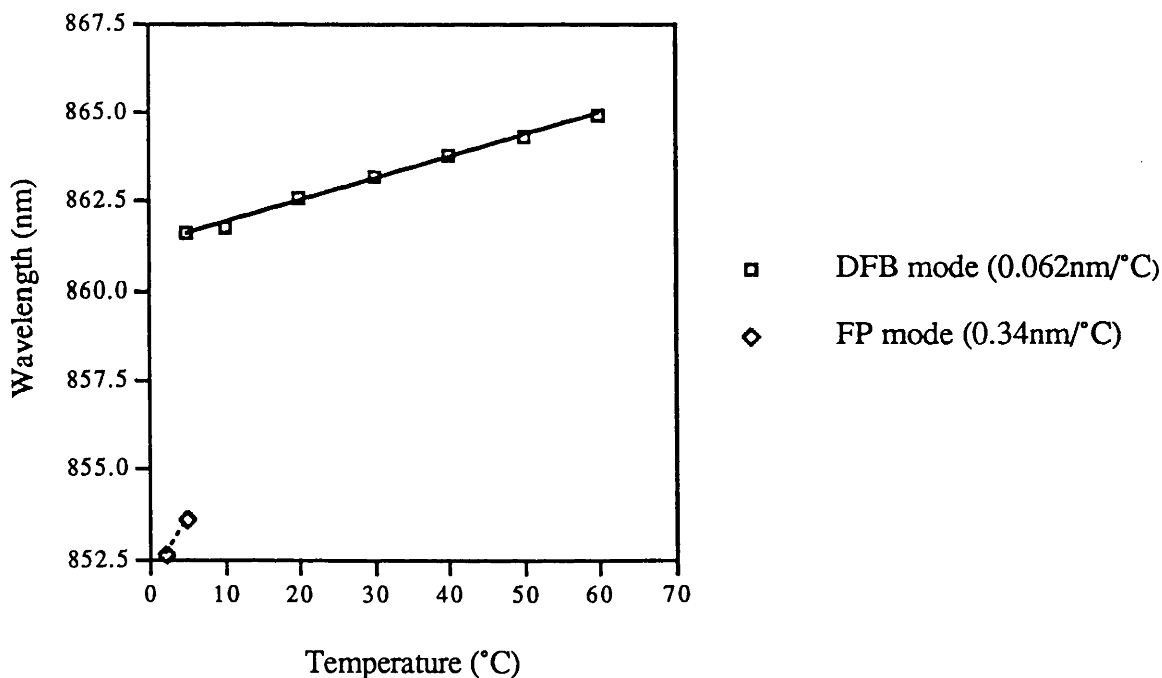

Fig.5.23. Temperature dependence of the spectrum of the 180 μm (30 %) non-uniform region DFB lasers.

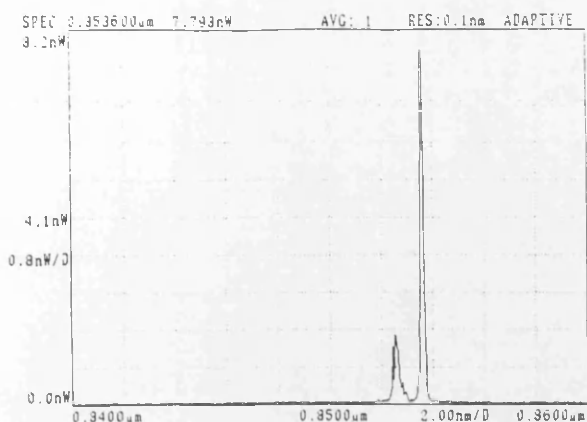

At 2 °C

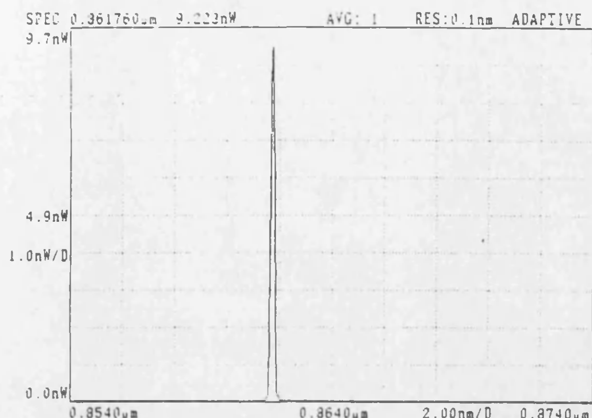

At 10 °C

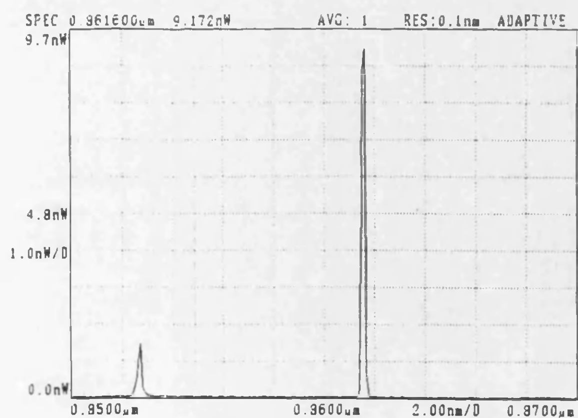

At 5 °C

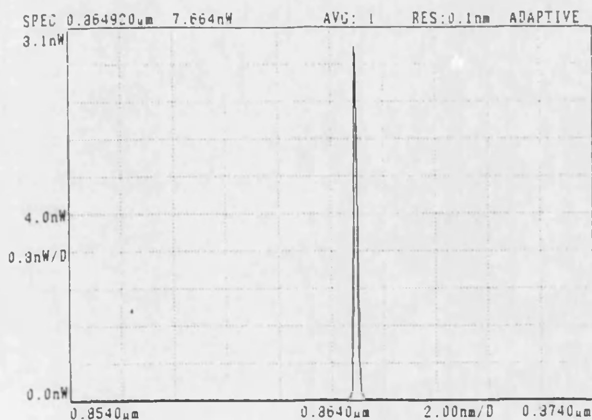

At 60 °C

Fig.5.24. Change of spectrum of the 180 μm (30 %) non uniform region DFB lasers for I = 60 mA, at 2, 5, 10 and 60 °C in pulsed operation.

5.2.2 Results for lasers in CW operation

In CW operation, laser chips were mounted on gold-plated steel heat-sinks. The devices evaluated are as follows:

(1) surface grating DFB uniform stripe lasers with AR coatings,

(2) surface grating DFB non-uniform stripe lasers with AR coatings.

(1) Surface grating DFB uniform stripe lasers with AR coatings

I-V curves and L-I curves were measured for the lasers, as follows:

(a) stripe width 2.5 μm and GaAs contact layer etched away,

(b) stripe width 4.5 μm and GaAs contact layer etched away.

The measured I-V curves in CW operation are shown in Fig.5.25. These lasers had the lowest threshold currents among four lasers within each category. Similar I-V characteristics result, despite the differences in the lasers. The turn on voltage was about 1.5 V and the differential resistance in the region from I = 30 mA to I = 60 mA was about 5 Ω.

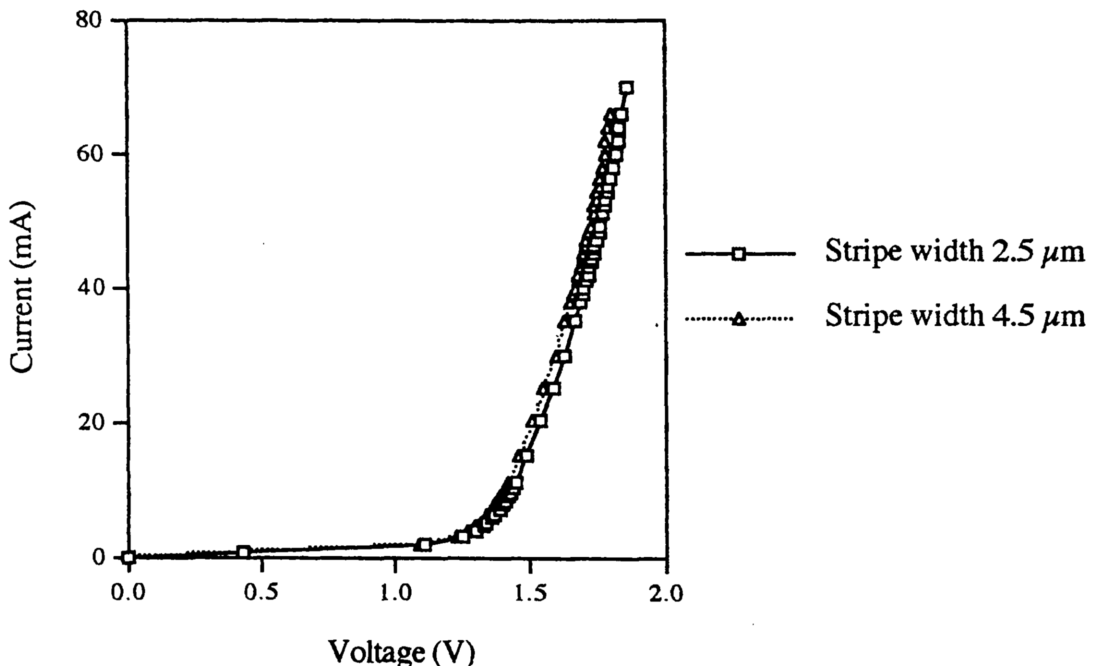

Fig.5.25. Measured current - voltage characteristics of surface grating DFB uniform stripe lasers with AR coatings, at 20 °C.

Fig.5.26 shows measured L-I curves for CW operation. Table 5.6 shows the external differential quantum efficiency, the threshold current and threshold current density from the L-I curves. The data were not so different from the measured data for pulsed operation. The optical power obtained was up to 7 mW per facet.

Table 5.6. Measured data for surface grating DFB uniform stripe lasers with AR coatings in CW operation, at 20 °C.

Lasers	External differential quantum efficiency per facet (%)	Threshold current (mA)	Nominal threshold current density (A/cm^2)
Stripe width 2.5μm GaAs contact layer etched.	15	37	2470
Stripe width 4.5μm GaAs contact layer etched.	19	40	1480

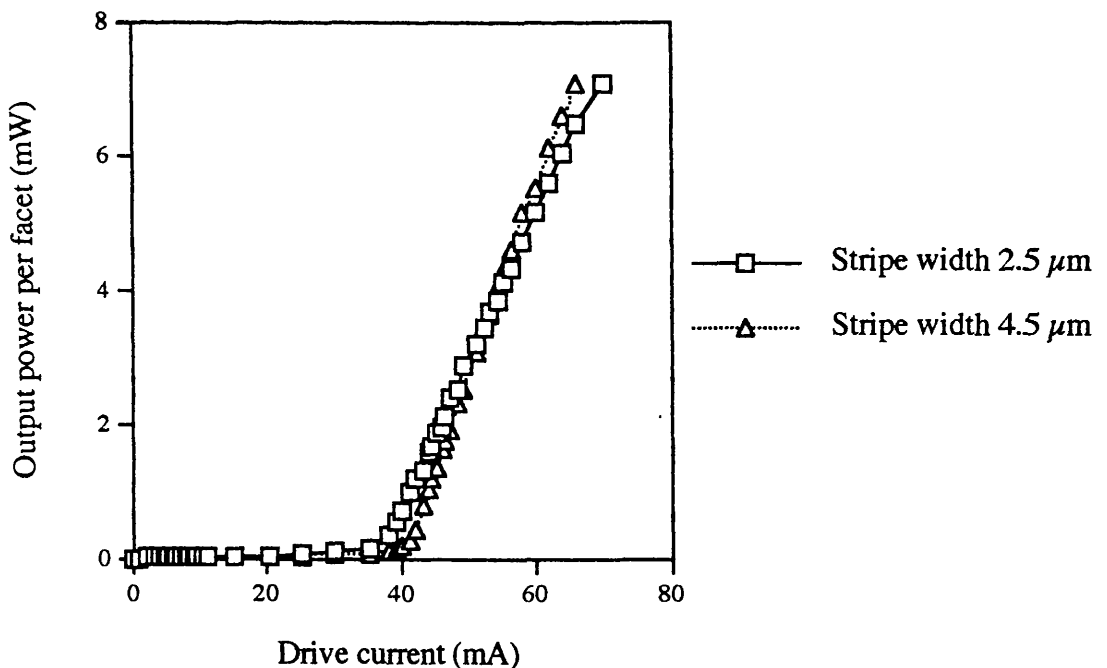

Fig.5.26. Measured output power per facet - drive current characteristics in surface grating DFB uniform stripe lasers with AR coatings for CW operation, at 20 °C.

Fig.5.27 shows measured spectra for the 2.5 μm width and 4.5 μm width stripe DFB lasers at 20 °C. There is no evidence of Fabry-Perot modes or higher order transverse modes. The emission wavelengths were 862.8 nm and 863.0 nm in the 2.5 μm width and the 4.5 μm width stripe lasers respectively. The emission wavelengths shifted to longer wavelengths with increasing drive current. This is likely to be due to change of the refractive index by heating caused by the increasing of the drive current.

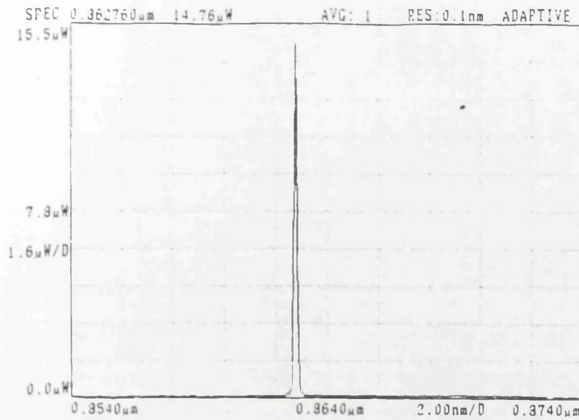

I = 45 mA (1.2 × I_{th})

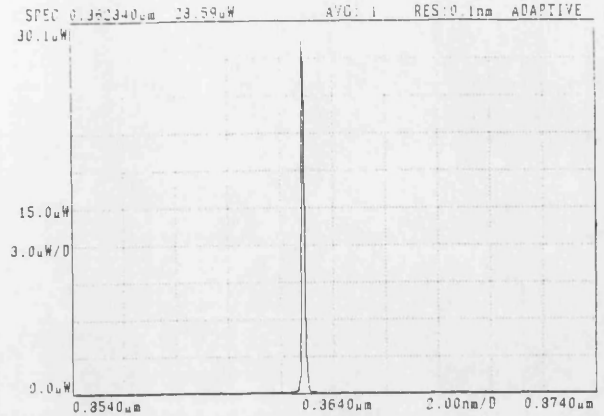

I = 60 mA (1.6 × I_{th})

(A) 2.5 μm stripe width (ND = 0.3)

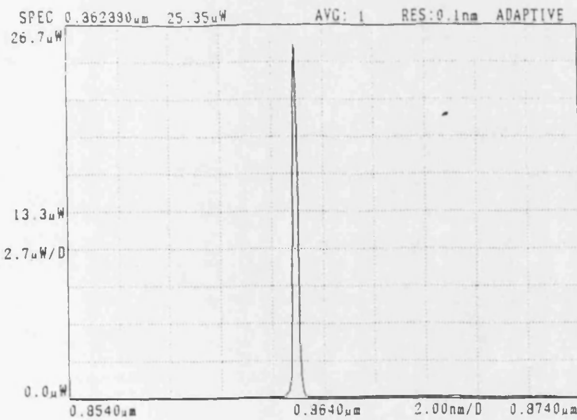

I = 50 mA (1.3 × I_{th})

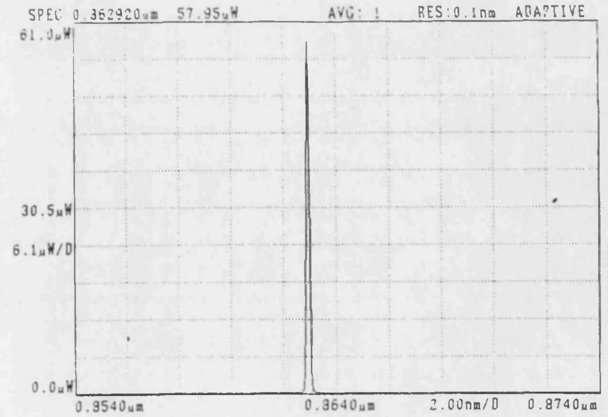

I = 65 mA (1.6 × I_{th})

(B) 4.5 μm stripe width (ND = 0.3)

Fig.5.27. Measured spectra for the 2.5 μm width stripe DFB lasers (A) and the 4.5 μm width stripe DFB lasers. (ND: Neutral density filter)

Fig.5.28 shows the spectra of the 2.5 μm width stripe DFB lasers for I=70 mA at 2, 5, 10 and 75 °C. It was found that the temperature range for single transversal DFB mode operation was from 10 to 75 °C and the DFB mode did not lase at 2 °C. There was evidence of another mode below 5 °C, which was likely to be the Fabry-Perot mode from its temperature dependence.[5-5]

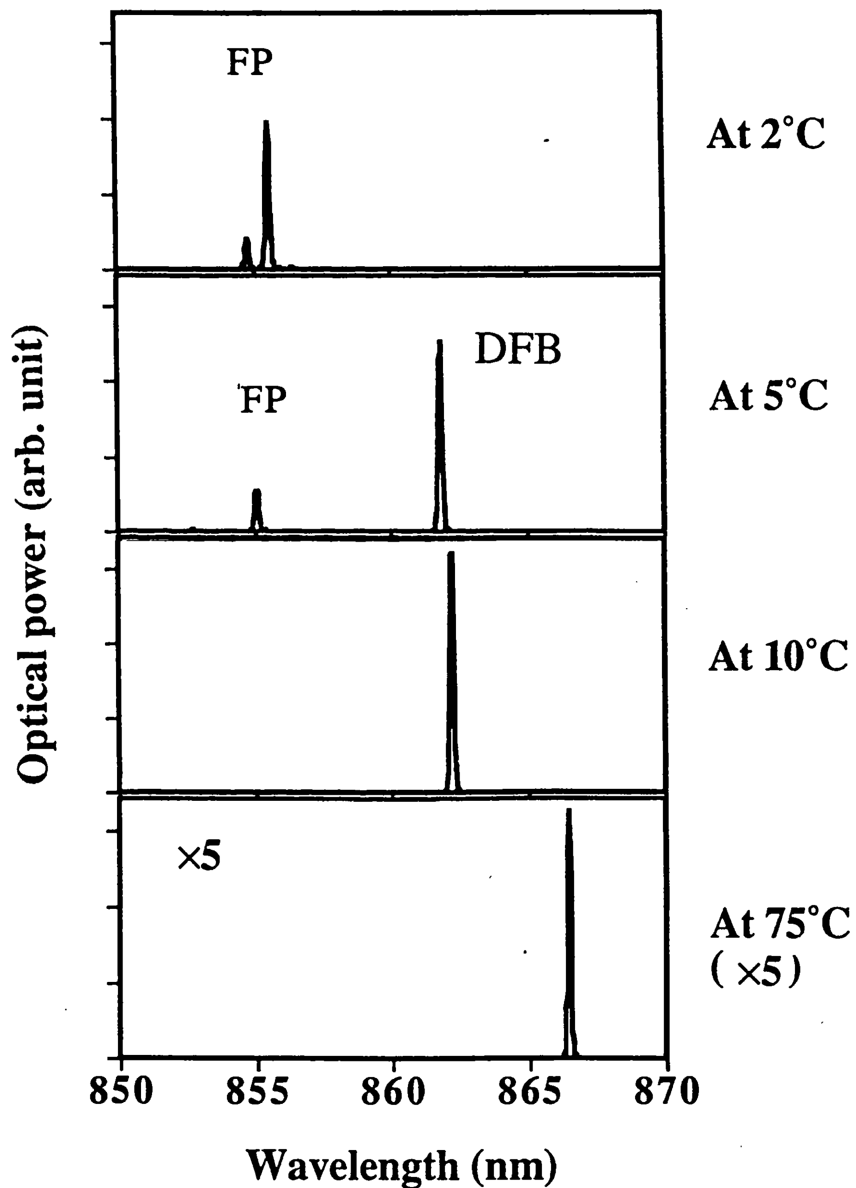

Fig.5.28. Measured spectra of the 2.5 μm width stripe DFB lasers for I = 70 mA at 2, 5, 10 and 75 °C.

The increase of junction temperature in CW operation can be estimated using the data of the temperature dependence of the spectrum in pulsed operation and CW operation.[5-12] The increase of the junction temperature ΔT is given by

$$\Delta T = \frac{\Delta\lambda}{d\lambda / dT} \qquad [5.20]$$

where $\Delta\lambda$ is change of emission wavelength between pulsed operation and CW operation and $\frac{d\lambda}{dT}$ is temperature coefficient of the emission wavelength. Fig.5.29 shows the temperature dependence of the spectrum of 2.5 μm width stripe DFB lasers for I=60 mA in pulsed (as shown in Fig.5.17) and CW operation. The measured change of wavelength between pulsed and CW operation $\Delta\lambda$ was 0.25 nm and the measured temperature coefficient of DFB lasing mode $\frac{d\lambda}{dT}$ was 0.063 nm/°C. From these values, the increase of the junction temperature was estimated to be about 4 °C, at a current of 60 mA.

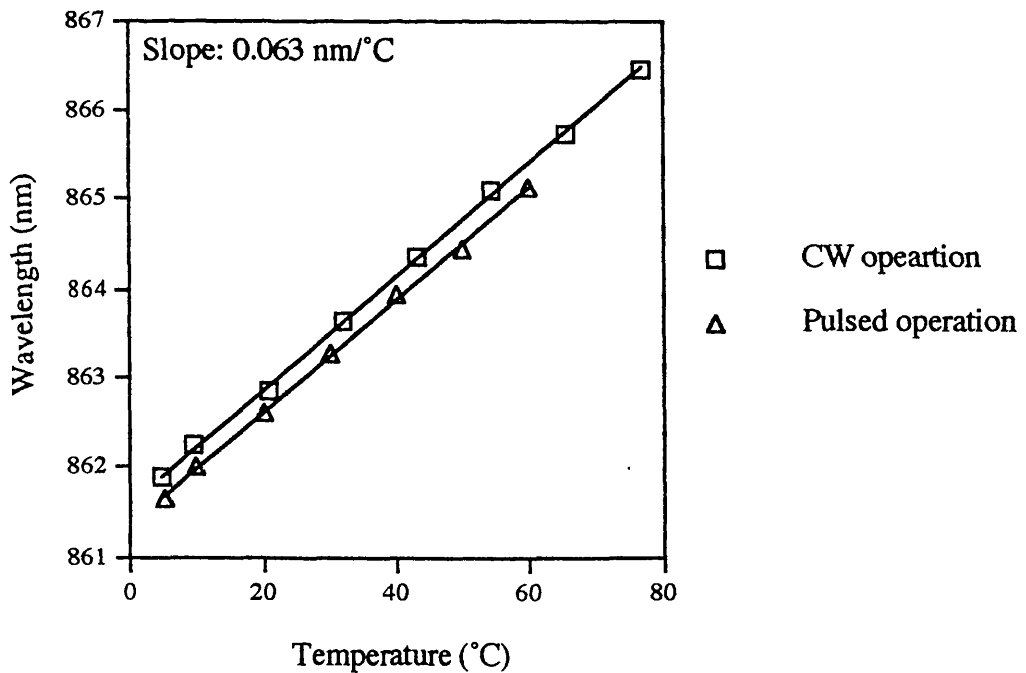

Fig.5.29. Measured temperature dependence of the spectrum of 2.5 μm width stripe DFB lasers for I=60 mA in pulsed and CW operation.

From the increase of the junction temperature, I-V curves and L-I curves, the thermal resistance can be estimated.[5-13] The thermal resistance R_{th} is given by

$$R_{th} = \frac{\Delta T}{P_{elec.} - P_{opt.}} \quad [5.21]$$

where ΔT is the increase of the junction temperature, $P_{elec.}$ is the injected electrical power to the laser and $P_{opt.}$ is the emitted optical power. The value of $P_{elec.}$ was 110 mW (I = 60 mA, V = 1.8 V) from Fig.5.25 and the value of $P_{opt.}$ was 10 mW at I= 60 mA from Fig.5.26. Accordingly, the thermal resistance R_{th} can be estimated to be about 40 °C/W.

Fig.5.30 shows the temperature dependence of the threshold current of the 2.5 μm width stripe DFB lasers. It was found that the threshold current increased with temperature. Similar characteristics have been reported by M.Nakamura et al.[5-14] The reason for the increase of the threshold current with increasing temperature is likely to be the decrease of the optical gain with increasing temperature and mis-match between the laser gain curve and the modal resonances established by the grating period at those temperatures.

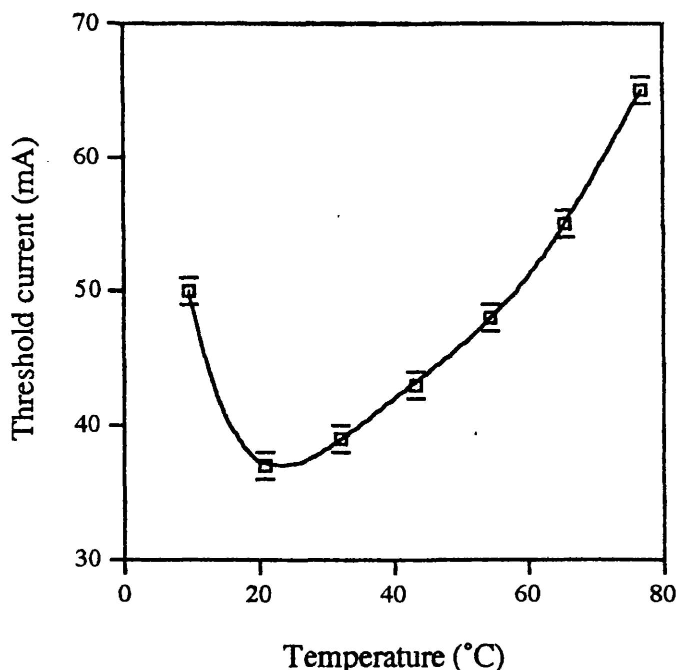

Fig.5.30. Temperature dependence of the threshold current of the 2.5 μm width stripe DFB lasers.

In conventional DFB lasers, a stopband should be observed. Normally, it is easier to observe the stopband near the threshold, where mode selection has not occurred[5-15, 5-16] Fig.5.31 shows the spectra of the 2.5μm width stripe DFB lasers for I = 30 mA (0.81 × I_{th}) and I = 35 mA (0.95× I_{th}) at 20 °C. The stopband was observed but it was difficult to measure the stopband width using the spectrum analyser. So the scanning Fabry-Perot interferometer method as shown in Fig.5.3 was used for the measurement of the stopband width.

To confirm the operation of the scanning Fabry-Perot interferometer method, the separation between the allowed longitudinal modes of the 2.5 μm width oxide stripe Fabry-Perot lasers with the cavity length of 600 μm was measured. The measured spectra are shown in Fig.5.32. The spacing of the Fabry-Perot interferometer cavity was 0.44 ± 0.02 mm. The Fabry-Perot lasers lased in multi-mode and the separation of the longitudinal modes was measured to be 0.12 ± 0.01 nm.

Here the separation of the longitudinal modes $\Delta\lambda_L$ is given by[5-5]

$$\Delta\lambda_L = \frac{\lambda^2}{2n(1 - \frac{\lambda}{n}\cdot\frac{dn}{d\lambda})L} \qquad [5.22]$$

where λ is the lasing wavelength, L is the cavity length and n is the refractive index in the semiconductor corresponding to the wavelength. In practice the group index $n(1-\frac{\lambda}{n}\cdot\frac{dn}{d\lambda})$ is found to have a value in GaAs of about 4.5 at λ =870 nm.[5-17] The separation between the longitudinal modes of the 2.5 μm width oxide stripe lasers with the cavity length of 600 μm (λ =860 nm) was calculated to be 0.137 nm.
It was confirmed that the measured value (0.12 ± 0.01 nm) using the scanning Fabry-Perot interferometer method closely agreed with the calculated value (0.137 nm).

Fig.5.33 shows measured spectra of the 4.5 μm width stripe DFB lasers for I = 42 mA using the scanning Fabry-Perot interferometer method. The stopband was observed and the stopband width was estimated to be 0.22 ± 0.01 nm. For the 2.5 μm width stripe DFB lasers, the stopband width was estimated to be 0.26 ± 0.01 nm (I= 39mA).

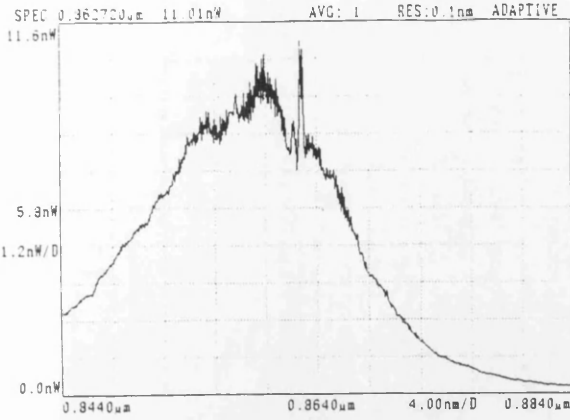

$I = 30$ mA ($0.81\times I_{th}$)

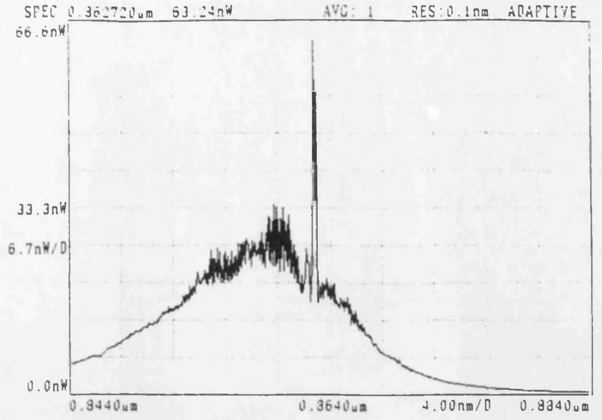

$I = 35$ mA ($0.95\times I_{th}$)

Wavelength range 40 nm

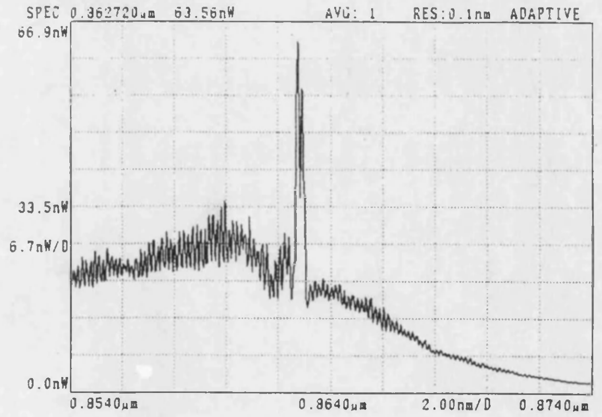

$I = 35$ mA ($0.95\times I_{th}$)

Wavelength range 20 nm

Fig.5.31 Measured spectra of the 2.5μm width stripe DFB lasers for I = 30 mA ($0.81\times I_{th}$) and I = 35 mA ($0.95\times I_{th}$), at 20 °C.

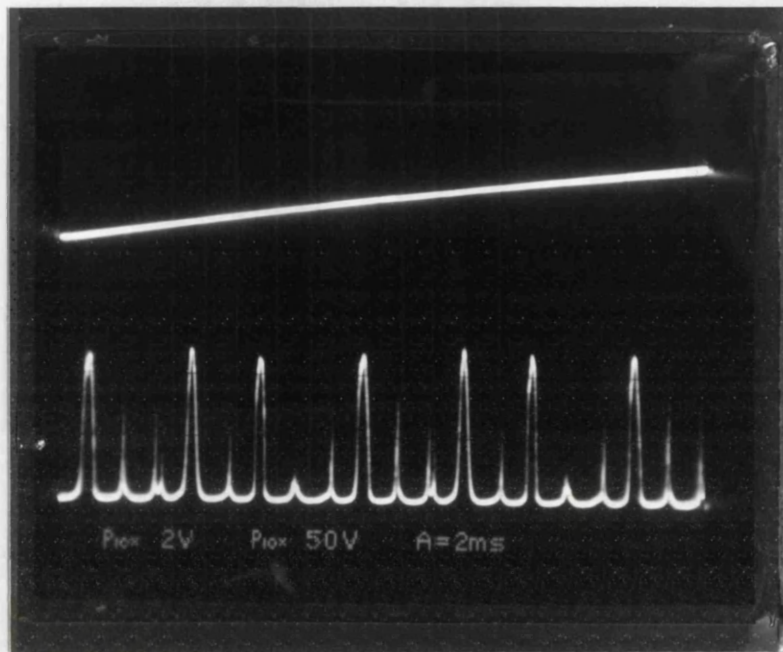

Fig.5.32 Measured spectra of the 2.5μm width oxide stripe Fabry-Perot lasers with the cavity length of 600 μm using the scanning Fabry-Perot interferometer method.

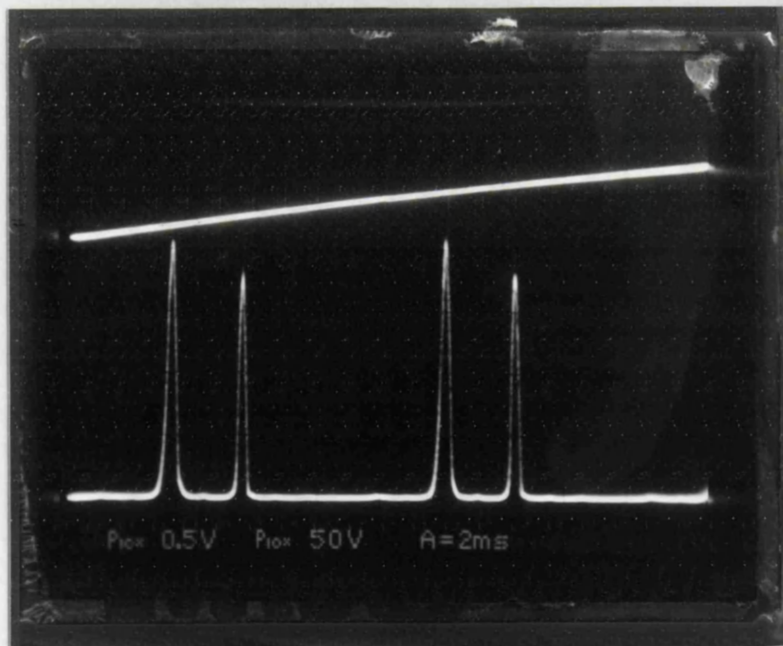

Fig.5.33. Measured spectra of the 4.5 μm width stripe DFB lasers for I = 42 mA (1.1 × I_{th}), using the scanning Fabry-Perot interferometer method.

From the stopband width, the coupling coefficient κ can be estimated using the threshold condition for DFB lasers as shown in Eqns. [5.18] and [5.19].[5-11, 5-18] The calculated relationship between the stopband width and the coupling coefficient is shown in Fig.5.34. From Fig.5.34, the coupling coefficients κ for the 2.5 μm width and 4.5 μm width stripe DFB lasers were calculated to be $\kappa_{2.5}$= 14 ± 2.2 cm^{-1} and $\kappa_{4.5}$= 5.5 ± 2.3 cm^{-1} respectively. These values are reasonably close to the calculated results, as shown in section 2.4 and close to the results given by L.M.Miller et al (κ=5.4 cm^{-1}).[5-6]

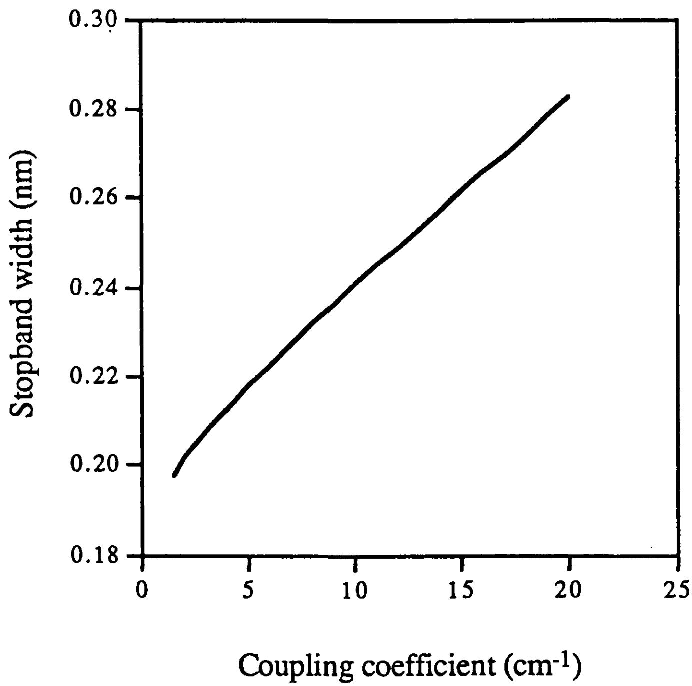

Fig.5.34. Calculated relationship between the stopband width and the coupling coefficient.

(2) Surface grating DFB non-uniform stripe lasers with AR coatings

Surface grating DFB non-uniform stripe lasers had a wider region which was located at the centre of the lasers. The width of the wider region was 4.5 μm and the width of the narrower region was 2.5 μm. The lengths of the wider regions were 60 μm (10%), 180 μm (30 %), 300 μm (50 %) and 420 μm (70 %). From measured I-V curves for the surface grating DFB non uniform stripe lasers in CW operation, the turn on voltage was about 1.5 V and the differential resistance in the region from I = 30 mA to I = 80 mA was about 5 Ω. Fig.5.35 shows measured L-I curves for CW operation at 20 °C. These lasers had the lowest threshold currents among three lasers within each category. Table 5.7 shows the external differential quantum efficiency, the threshold current and the threshold current density obtained from L-I curves. The data were not so different from the measured data for pulsed operation. The optical power obtained was up to 7 mW per facet.

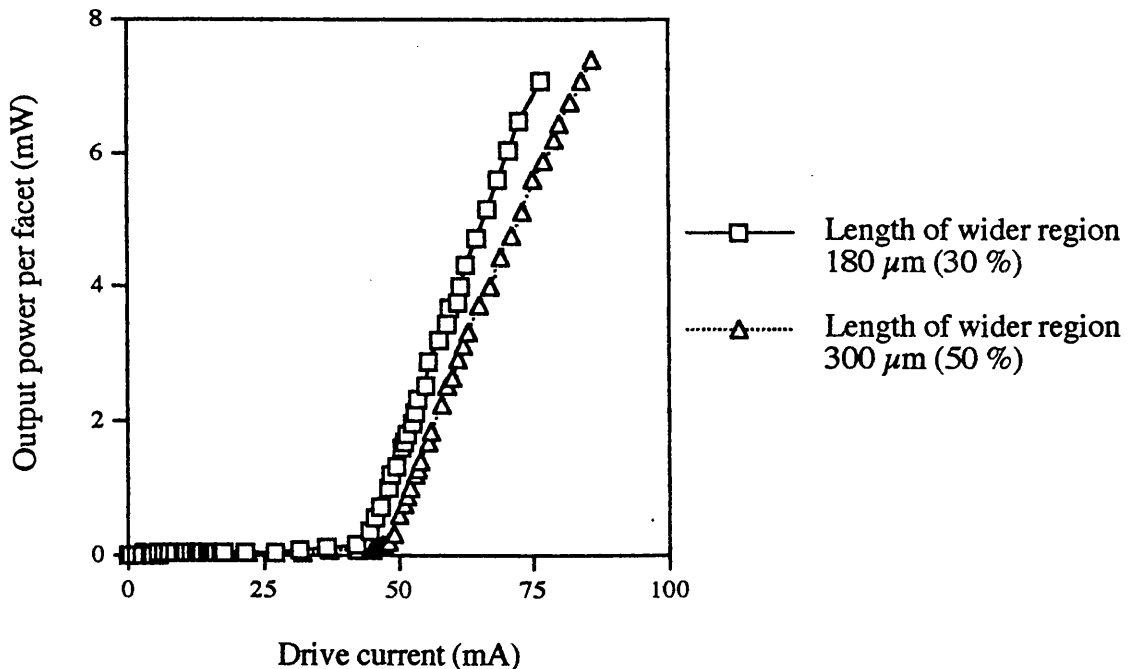

Fig.5.35. Measured output power per facet - drive current characteristics in surface grating DFB non-uniform stripe lasers with AR coatings in CW operation, at 20 °C.

Table 5.7. Measured data for surface grating DFB non-uniform stripe lasers with AR coatings in CW operation, at 20 °C.

Lasers	External differential quantum efficiency per facet (%)	Threshold current (mA)	Nominal threshold current density (A/cm^2)
Length of wider region 60 μm	15	42	2590
Length of wider region 180 μm	15	43	2310
Length of wider region 300 μm	13	47	2240
Length of wider region 420 μm	12	50	2140

Fig.5.36 shows measured spectra for the 300 μm (50 %) non-uniform region DFB lasers. There is no evidence of Fabry-Perot modes or higher order transverse modes. The emission wavelength was 863.0 nm. The emission wavelengths shifted to longer wavelengths with increasing drive current. This is likely to be due to the change of the refractive index by heating caused by increasing of the drive current.

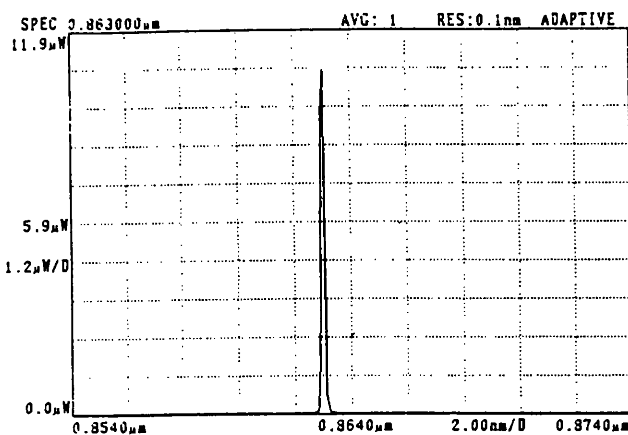

I = 50 mA (1.1 × I_{th})

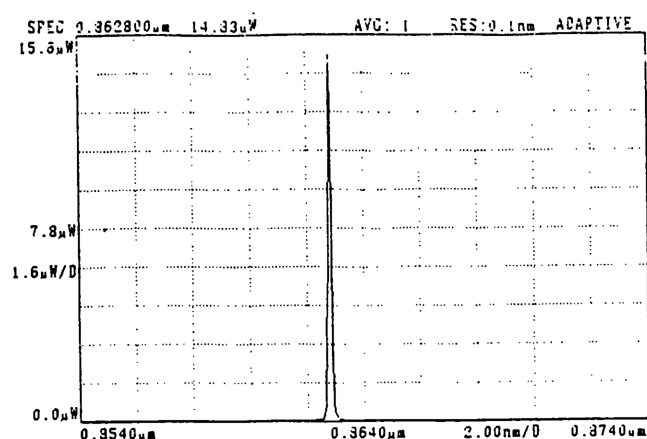

I = 65 mA (1.4 × I_{th})

Fig.5.36. Measured spectra for 300 μm (50 %) non-uniform region DFB lasers in CW operation, at 20 °C.

Fig.5.37 shows the temperature dependence of the spectrum of the 300 μm (50 %) non-uniform region DFB lasers. The measured temperature dependence of the DFB mode was 0.063 nm/°C. It was found that the temperature range for single transversal DFB mode operation was from 10 to 75 °C and that the DFB mode did not lase at 2°C. There was evidence of another mode below 5 °C, which was likely to be the Fabry-Perot mode from its temperature dependence. The reason for the onset of FP mode lasing below 5 °C is likely to be that the threshold gain for the FP mode becomes lower than the threshold gain for the DFB mode, because of the shift of the gain curve to shorter wavelengths, as shown in Fig.5.7.

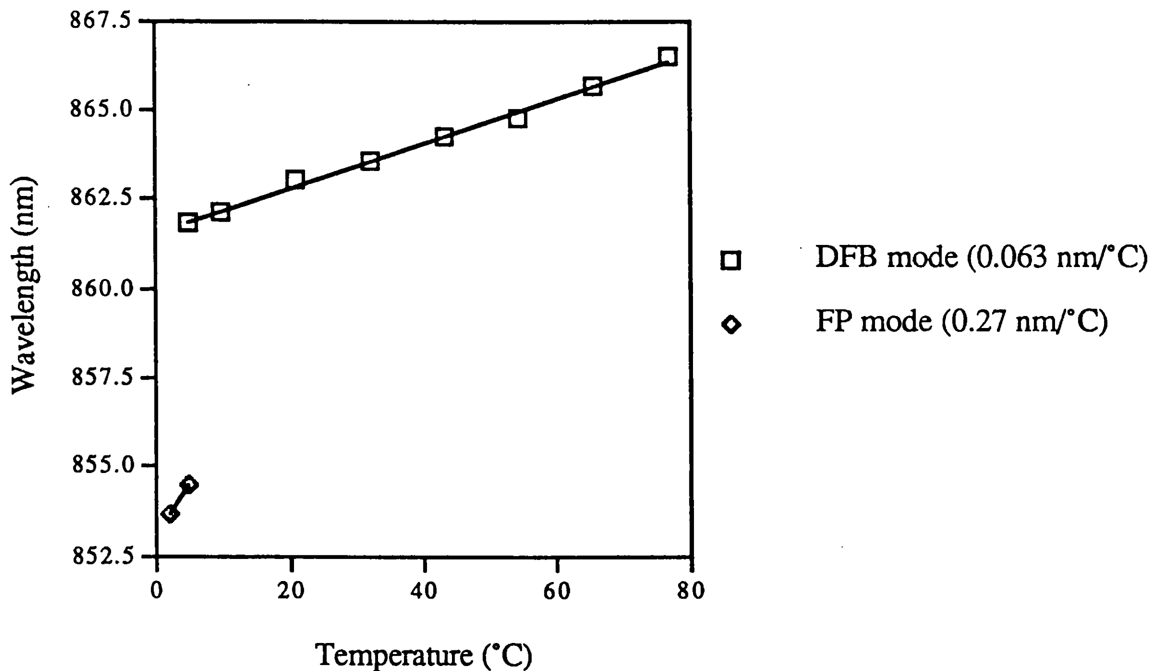

Fig.5.37. Measured temperature dependence of the spectrum of the 300 μm (50 %) non-uniform region DFB lasers in CW operation.

The scanning Fabry-Perot interferometer method as shown in Fig.5.3 was used for the measurement of the stopband width. For the 60 μm (10 %) non-uniform region and the 420 μm (70 %) non-uniform region DFB lasers, the stopband was observed and the width was measured to be 0.26 ± 0.01 nm ($I = 45$ mA, $1.1 \times I_{th}$) and 0.23 ± 0.01nm ($I = 53$ mA, $1.1 \times I_{th}$). On the other hand, for the 180 μm (30 %) non-uniform region and the 300 μm (50 %) non-uniform region DFB lasers, the stopband was not observed. Fig. 5.38 shows measured spectrum of the 300 μm (50 %) non-uniform region DFB lasers for I= 50 mA ($1.1 \times I_{th}$) using the scanning Fabry-Perot interferometer method.

The difference in the propagation constant between the narrower region and the wider region is calculated to be 7.5×10^{-3} μm^{-1} using the effective index method. Accordingly, the amount of the phase shift $\Delta\beta L$ is calculated to be 0.43 π and 0.72 π for the 180 μm (30 %) non-uniform region and the 300 μm (50 %) non-uniform region, respectively.

It has reported that a non-uniform region of gratings is effective for prevention of existence of the stopband, similar to the quarter wavelength shift effect, in buried grating structure DFB lasers.[5-19, 5-20] Soda et al.[5-20] have reported that the phase shift of 0.48 π is effective for prevention of existence of the stopband. These results mostly agreed with their results. However in this measurement, only two lasers for each type were measured. Accordingly, it is important to confirm reproduct ability of the observation of the stopband.

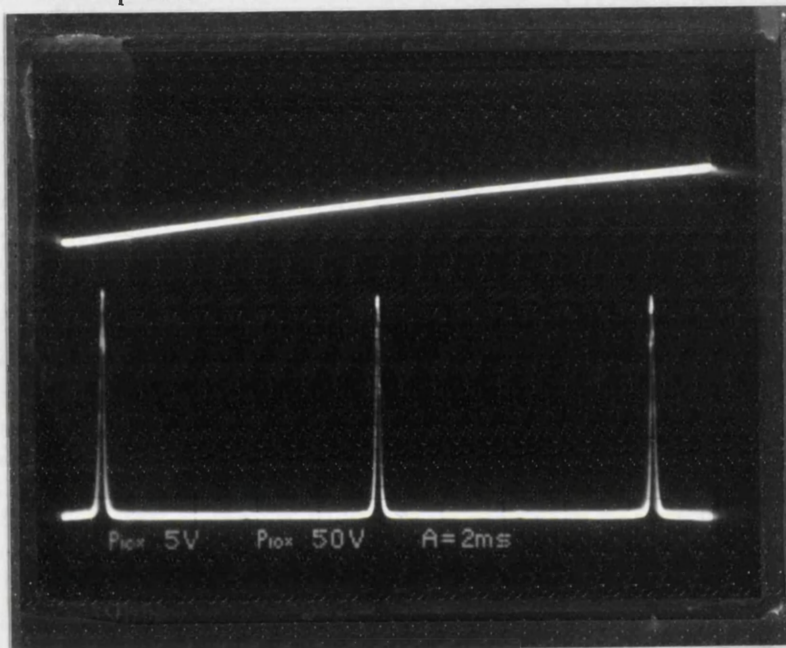

Fig.5.38. Measured spectrum of the 300 μm (50 %) non-uniform region DFB lasers for I = 50 mA using the scanning Fabry-Perot interferometer method.

References

5-1. M.J.Adams, A.G.Steventon, W.J.Devlin and I.D.Henning, "Semiconductor lasers for long-wavelength optical-fibre communications systems", Peter Peregrinus Ltd., 1987.

5-2. E.Hecht and A.Zajac, "Optics second edition", Addison-Wesley publishing company., 1987.

5-3. H.C.Casey,Jr, M.B.Panish, "Heterostructure Lasers Part B: Materials and Operating Characteristics", Academic Press., 1978.

5-4. H.Yonezu, I.Sakura, K.Kobayashi, T.Kamejima, M.Ueno and Y.Nannichi, "A GaAs-$Al_xGa_{1-x}As$ Double Heterostructure Planar Stripe Laser", Japanese Journal of Applied Physics, Vol. 12, p. 1585-1592, 1973.

5-5. S.M.Sze, "Semiconductor devices physics and technology", John Wiley and Sons., p. 274-278, 1985.

5-6. L.M.Miller, K.J.Beernink, J.T.Verdeyen, J.J.Coleman, J.S.Hughes, G.M.Smith, J.Honing and T.M.Cockerill, "Characterization of an InGaAs-GaAs-AlGaAs strained-layer distributed-feedback ridge-waveguide quantum-well heterostructure laser", IEEE Photonics Technology Letters, Vol. 4, p. 296-299, 1992.

5-7. G.H.B.Thompson, "Physics of semiconductor laser devices", John Wiley and Sons., Chap. 8, 1980.

5-8. S.Akiba, K.Utaka, K.Sakai and Y.Matsushima, "Asymmetry in output power of InGaAsP/InP DFB lasers", Japanese Journal of Applied Physics, Vol. 23, p. 1054-1059, 1984.

5-9. C.Lin, "Optoelectronic technology and lightwave communications systems", Van Nostrand Reinhold, Chap. 11, 1989.

5-10. A.Yariv, "Quantum electronics", John Wiley and Sons., p. 600-623, 1987.

5-11. A.Yariv and M.Nakamura, "Periodic Structures for Integrated Optics", IEEE Journal of Quantum Electronics, Vol. QE-13, p. 233-253, 1977.

5-12. G.H.B.Thompson, "Physics of semiconductor laser devices", John Wiley and Sons., p. 523-527, 1980.

5-13. T.L.Paoli, "A new technique for measuring the thermal impedance of junction lasers", IEEE Journal of Quantum Electronics, Vol. QE-11, p. 498, 1975.

5-14. M.Nakamura, K.Aiki, J.Umeda and A.Yariv, "CW operation of distributed feedback GaAs-GaAlAs diode lasers at temperatures up to 300K", Applied Physics Letters, Vol. 27, p. 403, 1975.

5-15. M.Aoki, K.Uomi, T.Tsuchiya, S.Sasaki, M.Okai and N.Chinone, "Quantum size effect on longitudinal spatial hole burning in MQW $\lambda/4$-shifted DFB lasers", IEEE Journal of Quantum Electronics, Vol. 27, p. 1782-1789, 1991.

5-16. K.Utaka, S.Akiba, K.Sakai and Y.Matsushima, " λ/4-shifted InGaAsP/InP DFB lasers ", IEEE Journal of Quantum Electronics, Vol. QE-22, p. 1042-1051, 1986.

5-17. G.H.B.Thompson, "Physics of semiconductor laser devices", John Wiley and Sons., p. 114-118, 1980.

5-18. K.Iga, "On the use of effective refractive index in DFB laser mode separation", Japanese Journal of Applied Physics, Vol. 22, p. 1630, 1983.

5-19. K.Tada, Y.Nakane and A.Ushirokawa, "Proposal of a distributed feedback laser with nonuniform stripe width for complete single-mode oscillation.", Electronics Letters, Vol. 20, p. 82-84, 1984.

5-20. H.Soda, K.Wakao, H.Sudo, T.Tanahashi and H.Imai, "GaInAsP/InP phase-adjusted distributed feedback lasers with a step-like nonuniform stripe width structure.", Electronics Letters, Vol. 20, p. 1016-1018, 1984.

Chapter 6 : Conclusions and future work

6.1 Conclusions

The original objective of this work was to fabricate and evaluate deep surface grating DFB stripe lasers using quantum well material. The distributed feedback structure was created by deep, dry etched, gratings alongside the ridge in the top confining layer of the laser. The material system used consisted of two 0.01 μm GaAs quantum wells and 0.01 μm $Al_{0.2}Ga_{0.8}As$ barriers. Typical emission wavelength of the lasers was about 860 nm.

In chapter 3, concerned with epitaxial wafer structure and its characterisation, the quantum well epitaxial wafer used for this work was shown , using broad area oxide stripe lasers, to have satisfactory characteristics, such as the transparency current J_t = 120 A/cm^2, the quantum well gain parameter for one well g_0 = 1700 cm^{-1} and the internal optical loss α = 14.5 cm^{-1}.

In chapter 4: 'Device structure and fabrication', optimum conditions were described to produce a third order 1:1 mark-space ratio grating using the holographic exposure, shadow evaporation and reactive ion etching processes.

In chapter 5: 'Measurements', the light output - drive current characteristics, temperature range for single transversal DFB mode operation and the increase of junction temperature in CW operation were described.

It is concluded that the scanning Fabry-Perot method allows an accurate estimation of the stopband width. From the estimated stopband width, the coupling coefficient was calculated and the value agreed with an approximate value obtained from passive waveguide calculations using the effective index method in section 2.4.

As regards surface grating DFB non-uniform stripe lasers, the light output - drive current characteristics and temperature range for single transversal DFB mode operation were obtained in CW operation. It was confirmed that a suitable non-uniform stripe structure was effective in achieving single longitudinal mode operation.

6.2 Future work

Possible extensions of the work carried out in this thesis are as follows:

(1) measurements of the emission linewidth of surface grating DFB non-uniform stripe lasers, under a range of operating conditions

(2) theoretical calculations of threshold gain and the oscillation frequency for surface grating DFB non-uniform stripe lasers using numerical calculation methods.

Emission linewidths may be measured using the scanning Fabry-Perot method or self-homodyne/ heterodyne method.[6-1, 6-2] Minimum resolution of measured linewidth is about 10 MHz and about 50 kHz[6-1] respectively. In general, the self-homodyne/ heterodyne method requires more complicated set-up.

Measurements of the relationship between emission linewidth and the length of the non-uniform region and also the drive current dependence of the linewidth are also important.

The threshold gain and the oscillation frequency for the DFB non-uniform stripe lasers may be calculated using the F-matrix method[6-3, 6-4] briefly described in section 2.5. Comparison between the theoretically calculated results and measured results described in this thesis is clearly important.

References

6-1. T.Okoshi, K.Kikuchi and A.Nakayama, "Novel method for high resolution measurement of laser output spectrum", Electronics Letters, Vol. 16, 1980.

6-2. K.Iiyama, K.Hayashi, Y.Ida and S.Tabata, "Delayed self-homodyne method using solitary monomode fibre for laser linewidth measurements", Electronics Letters, Vol. 25 1989.

6-3. M.Yamada and K.Sakuda, "Analysis of almost-periodic distributed feedback slab waveguides via a fundamental matrix approach", Applied Optics, Vol. 26, p. 3474-3478, 1987.

6-4. M.Okai, S.Tsuji and N.Chinone, "Stability of the longitudinal mode in $\lambda/4$-shifted InGaAsP/InP DFB lasers", IEEE Journal of Quantum Electronics, Vol. 25, p. 1314-1319, 1989.

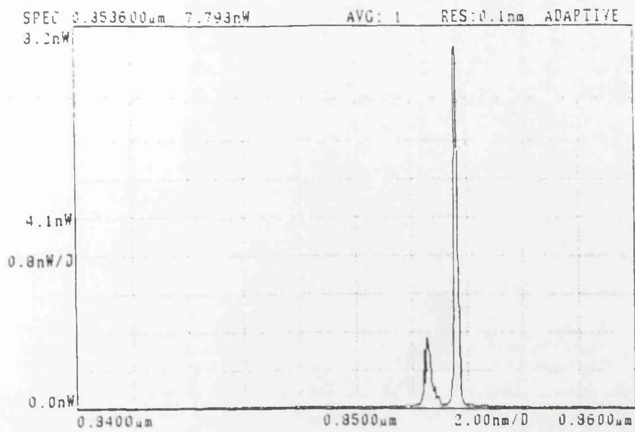

At 2 °C

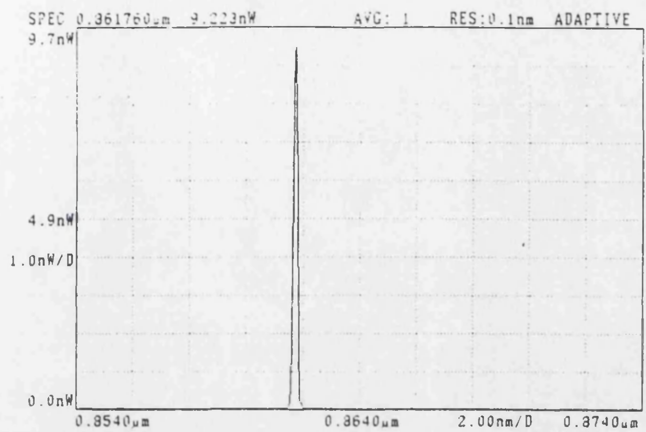

At 10 °C

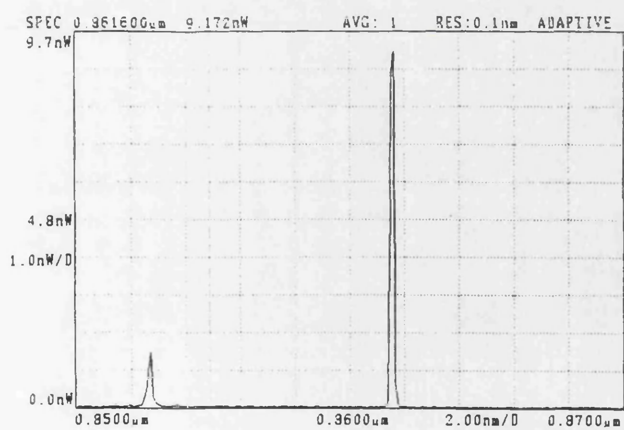

At 5 °C

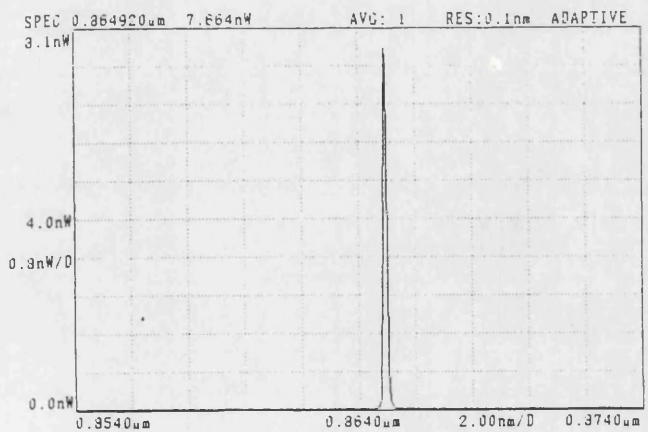

At 60 °C

Fig.5.24. Change of spectrum of the 180 μm (30 %) non uniform region DFB lasers for I = 60 mA, at 2, 5, 10 and 60 °C in pulsed operation.